In situ Characterization of Deformation Mechanisms in Harmonic Structure Nickel

Sjögren-Levin, Elis

2024

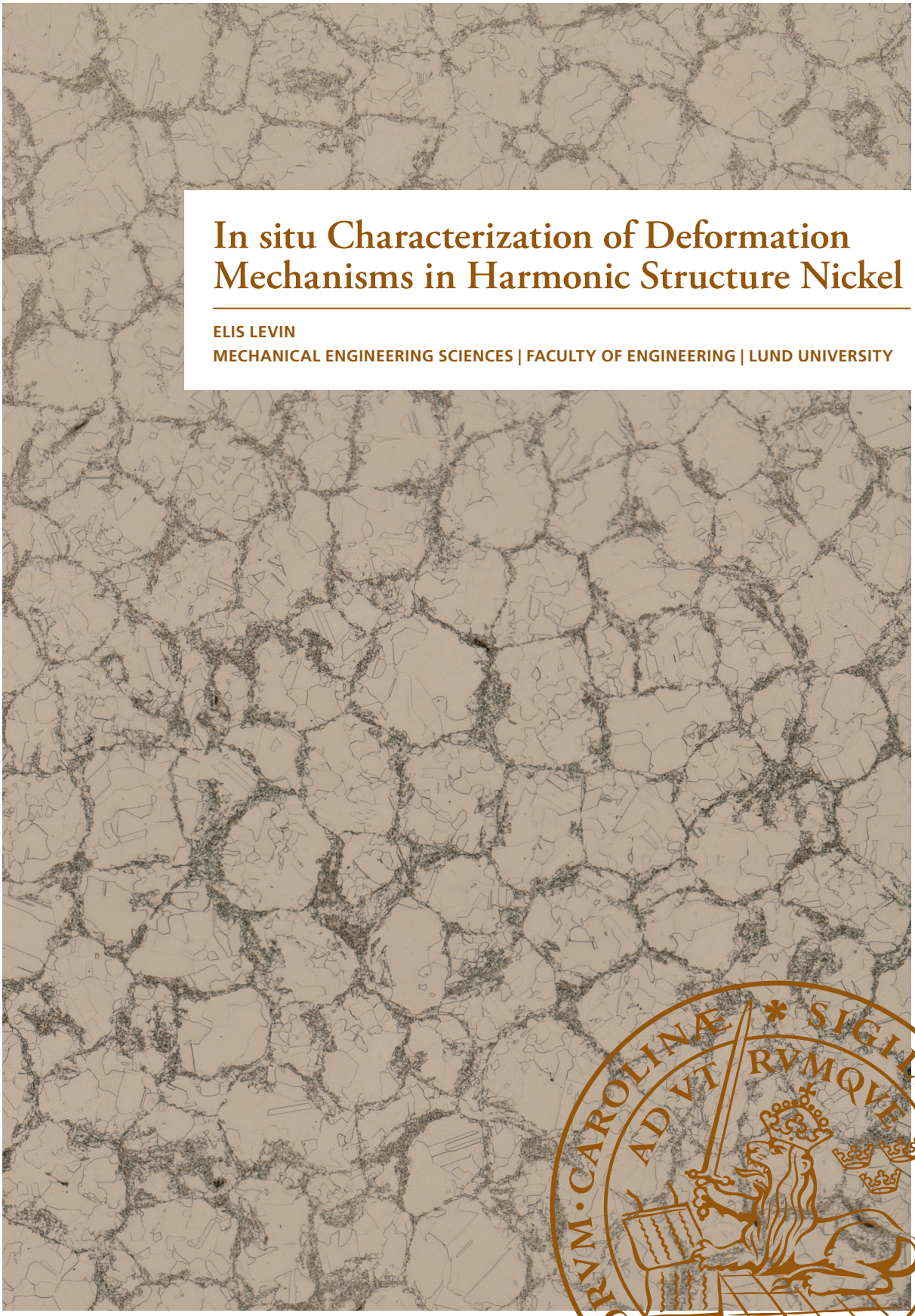

In situ Characterization of Deformation Mechanisms in Harmonic Structure Nickel

ELIS LEVIN
MECHANICAL ENGINEERING SCIENCES | FACULTY OF ENGINEERING | LUND UNIVERSITY

In situ Characterization of Deformation Mechanisms in Harmonic Structure Nickel

In Situ Characterization of Deformation Mechanisms in Harmonic Structure Nickel

Elis Levin

LUND
UNIVERSITY

DOCTORAL DISSERTATION

Doctoral dissertation for the degree of Doctor of Philosophy (PhD) at the Faculty of Engineering at Lund University to be publicly defended on the 22nd of November at 9.00 in lecture hall M:E, Department of Mechanical Engineering Sciences, Ole Römers väg 1, Lund

Faculty opponent
Professor Dorte Juul Jensen
Technical University of Denmark (DTU), Department of Civil and Mechanical Engineering, Lyngby, Denmark

Organization: Division of Mechanics, Materials and Component Design, Department of Mechanical Engineering Sciences, Faculty of Engineering, LUND UNIVERSITY

Document name: DOCTORAL DISSERTATION **Date of issue:** 2024-10-22

Author: Elis Levin **Sponsoring organization:**

Title and subtitle: In situ Characterization of Deformation Mechanisms in Harmonic Structure Nickel

Abstract: There is an ever-increasing demand for structural metals with higher strength. Metals can be strengthened by reducing grain size in their microstructure, but ductility is also concomitantly reduced. High strength and ductility are a desirable combination of properties for most structural engineering materials. By arranging fine grains in a continuous network that surrounds islands of coarse grains, in a so-called harmonic structure, it is possible to increase the strength without reducing ductility. Such a synergetic effect has been attributed to an accelerated work-hardening rate in harmonic structures.

This thesis aims at deepening the understanding of the synergetic effects, which can help the optimization of harmonic structures in the future. The distributions of stress and strain were measured during tensile testing as they are deemed important for understanding the interplay between coarse and fine grain fractions. Stress distribution among the grain fractions were measured at unprecedented detail in harmonic structures materials through synchrotron X-ray powder diffraction and individual grains through high resolution reciprocal space mapping. To achieve individual investigation of grain fractions, a new algorithm was elaborated in this work for the separation and analysis of diffraction data in a single-phase material with two fractions of grain sizes. The distribution of strain was measured with digital image correlation in optical microscopy.

The main achievements in this work reveal that the constriction of coarse grains by fine grains in harmonic structures increases the yield strength of coarse grains compared to homogenous counterparts. At elastic-plastic transition, stress partitions between the grain fractions and back stresses develop in coarse grains along with forward stresses in fine grains. With further macroscopic strain, the local strains also clearly partition between the grain fractions. The stress-strain behaviour of the grain fractions is similar to the homogenous counterparts when the local and macroscopic strains are similar. The high work-hardening rate of the harmonic structure is the superposition of fine grains with inherited high work-hardening rate and coarse grains with low work-hardening rate. Beyond elastic-plastic transition, the acceleration of work-hardening rate in the coarse-grained fraction is found, which coincides with the strain partitioning. The evolution of strain distributions shortly before macroscopic fracture indicates that the microstructure might suppress strain localization. However, full understanding of fracture mechanisms requires further investigation.

Key words: Heterogenous structure, Harmonic structure, Synchrotron radiation, X-ray diffraction, Stress partitioning, Digital image correlation, Strain partitioning

Classification system and/or index terms (if any)	Supplementary bibliographical information
ISBN: 978-91-8104-255-9 (print)	**ISSN and key title**:
ISBN: 978-91-8104-256-6 (electronic)	**Language:** English
Recipient's notes	**Number of pages**: 91
Price	Security classification

In Situ Characterization of Deformation Mechanisms in Harmonic Structure Nickel

Elis Levin

LUND
UNIVERSITY

Coverphoto by Elis Levin

Faculty of Engineering
Department of Mechanical Engineering Sciences
Division of Mechanics Materials and Component Design

ISBN 978-91-8104-255-9 (print)
ISBN 978-91-8104-256-6 (electronic)

Printed in Sweden by Media-Tryck, Lund University
Lund 2024

Acknowledgements

I would like to express my deepest gratitude to all those who have supported and guided me throughout my Ph.D. journey.

First, I extend my sincere thanks to Professor Srinivasan Iyengar, whose inspiring lectures sparked my initial interest in metallurgy. His passion for the subject ultimately led me to pursue a master's thesis project at the Division of Materials Engineering with Professor Dmytro Orlov and Höganäs AB. This brings me to my next expression of gratitude—to Professor Dmytro Orlov, who saw a future Ph.D. student in me and encouraged me to apply for a project for which he had secured funding.

My research was conducted at the Division of Materials Engineering, now the Division of Mechanics, Materials, and Component Design, under the supervision of, in turn, Professor Dmytro Orlov, Professor Solveig Melin, and Professor Aylin Ahadi. I am deeply thankful to each of them for their support, insightful guidance, and constant encouragement throughout my doctoral work. A special thanks to my co-supervisor, Dr. Filip Lenrick, who has been an invaluable support, both professionally and personally, during challenging times. I would also like to thank Dr. Rikard Hjelm and Dr. Pär A. T. Olsson for their moral support.

I extend my sincere appreciation to my co-authors, Professor Kei Ameyama and Professor Nobuhiro Tsuji, who welcomed me into their laboratories during my stay in Japan. I am grateful for the access they provided to their facilities, as well as the support from their students and staff, who helped me fabricate my research materials and learn best-practice metallurgical lab work. I am also greatly thankful for the meaningful discussions with my co-author, Professor Wolfgang Pantleon, which significantly accelerated my understanding of the subject. I thank the PETRA III P21 beamline staff and Josephine Chatilier, who greatly improved the studies with digital image correlation during her research project that I co-supervised.

I appreciate all the help I received from my colleagues and the staff at the department, especially Rose-Marie Hermansson for her administrative assistance. A special mention to my former and current office mates, Dr. Hossein, Dr. Alex, and Johan, for good company as well as moral support, valuable advice, and encouraging discussions. I also thank the other Ph.D. students for the fun times during lunch and outside the office.

On a personal note, I would like to extend my heartfelt gratitude to my family and friends. Their unwavering support, patience, and encouragement were crucial in helping me push through challenging moments.

Finally, Frida—what would I be without you? I thank you and our wonderful child Verner for bringing so much joy into my life and reminding me of what is truly important.

Table of Contents

Abstract

There is an ever-increasing demand for structural metals with higher strength. Metals can be strengthened by reducing grain size in their microstructure, but ductility is also concomitantly reduced. High strength and ductility are a desirable combination of properties for most structural engineering materials. By arranging fine grains in a continuous network that surrounds islands of coarse grains, in a so-called harmonic structure, it is possible to increase the strength without reducing ductility. Such a synergetic effect has been attributed to an accelerated work-hardening rate in harmonic structures.

This thesis aims at deepening the understanding of the synergetic effects, which can help the optimization of harmonic structures in the future. The distributions of stress and strain were measured during tensile testing as they are deemed important for understanding the interplay between coarse and fine grain fractions. Stress distribution among the grain fractions were measured at unprecedented detail in harmonic structures materials through synchrotron X-ray powder diffraction and individual grains through high resolution reciprocal space mapping. To achieve individual investigation of grain fractions, a new algorithm was elaborated in this work for the separation and analysis of diffraction data in a single-phase material with two fractions of grain sizes. The distribution of strain was measured with digital image correlation in optical microscopy.

The main achievements in this work reveal that the constriction of coarse grains by fine grains in harmonic structures increases the yield strength of coarse grains compared to homogenous counterparts. At elastic-plastic transition, stress partitions between the grain fractions and back stresses develop in coarse grains along with forward stresses in fine grains. With further macroscopic strain, the local strains also clearly partition between the grain fractions. The stress-strain behaviour of the grain fractions is similar to the homogenous counterparts when the local and macroscopic strains are similar. The high work-hardening rate of the harmonic structure is the superposition of fine grains with inherited high work-hardening rate and coarse grains with low work-hardening rate. Beyond elastic-plastic transition, the acceleration of work-hardening rate in the coarse-grained fraction is found, which coincides with the strain partitioning. The evolution of strain distributions shortly before macroscopic fracture indicates that the microstructure might suppress strain localization. However, full understanding of fracture mechanisms requires further investigation.

Populärvetenskaplig sammanfattning

Målet med denna avhandling är att förstå mekanismerna som sker i nickel designat på mikrostrukturnivå med en harmonisk struktur allt eftersom det deformeras under dragning. Vad det innebär förklaras här nedan.

För att förstå vad en harmonisk struktur är behöver man veta vad ett korn innebär för en materialvetare. Tänk dig att du ska bygga en sten av oregelbundet kantiga gruskorn. Inom varje korn ligger atomerna i ett repeterande mönster. Gruskornen måste sättas in i olika riktningar relativt varandra för att kunna bygga upp en sten som saknar hålrum emellan gruskornen. På samma sätt är en metall uppbyggd. Skillnaden är att kornen vanligtvis är för små för att se med blotta ögat utan är i storleksordningen mikrometer, därav namnet mikrostruktur. Med en harmonisk struktur menas att vi har designat mikrostrukturen på så sätt att kluster av stora korn ligger insprängda i ett kontinuerligt nätverk av små korn.

Varför bemöda sig att skapa en sådan struktur? För att det ökar styrkan på materialet. Metallbaserade material finns överallt runt om oss, som till exempel armeringsjärn i byggnader, komponenter i bilar och köksredskap. Genom att utveckla starkare material kan en mindre mängd material användas för att bära samma laster utan att ge vika. Det är bra ur klimat- och energisynpunkt på två sätt. Dels minskar materialåtgången, vilket är bra i sig, och dessutom minskas vikten i motordrivna föremål, vilket minskar energiåtgången för deras drivning. Det finns många sätt att stärka metalliska material; det går att blanda grundmetaller till en legering, utföra värmebehandling av materialet eller bearbeta materialet mekaniskt. Detta gör att atomerna som materialet består av arrangerar om sig, vilket drastiskt kan ändra de mekaniska egenskaperna. Problemet är att när styrkan på materialet ökan, så minskar dess plastiska seghet. Plastisk seghet är ett mått på hur mycket ett material, efter att först ha gett vika, kan deformeras tills att det börjar spricka och gå itu. I strukturella material vill man ha ett visst mått av seghet. Om materialet är tillräckligt segt, kan man i förtid se om en komponent har överstigit sin last och åtgärda det. Ett material som saknar plasticitet kan spricka utan förvarning, vilket kan ge ödesdigra konsekvenser. Problemet kallas styrka-seghet-dilemmat. Det går inte att få det ena utan att göra avkall på det andra. Idealt sett vill man öka styrkan utan att minska segheten. Med vissa legeringar har man delvis kunnat uppnå detta genom att låta atomer från grundmetallerna fördela sig i kluster med olika sammansättning. Om man i stället är begränsad till en viss kombination av atomer som ska vara samma genom hela komponenter, är möjligheterna få.

Det är möjligt att bearbeta metallen mekaniskt så att kornstorleken minskas. Med en minskad kornstorlek ökar styrkan (definierad som flytspänning, som ska förklaras ytterligare) dramatiskt men segheten minskar likaså. En lovande metod för att överkomma dilemmat är att blanda grupper av stora och små korn. Det finns många olika sätt att arrangera grupperna av korn, varav harmonisk struktur är en.

Med en sådan struktur har det visat sig möjligt att få styrkan från de små kornen och segheten från de stora. Materialets egenskaper är alltså inte en blandning av egenskaperna från de två korngrupperna, utan genom positiva samverkanseffekter får man de bästa från vardera.

Hur materialet produceras på labbnivå beskrivs i avhandlingen, men notera att frågor som berör storskalig produktion och tillämpningsområden inte behandlas. Det är frågor för framtida forskning och utveckling. Avhandlingen handlar om att förstå mekanismerna som ger de positiva effekterna. Med god förståelse för mekanismerna kan designen optimeras ytterligare och materialet användas i praktiska tillämpningar med god säkerhet.

För att studera materialet har vi utfört dragprov. Det innebär att man töjer (drar ut) materialet och mäter vilken kraft som krävs för att göra detta. Man vet då hur mycket provbiten är töjd i genomsnitt, och om man tar provbitens dimensioner i beaktande, storleken på den genomsnittliga spänningen. Från det kan man få ut en rad övergripande värden såsom flytspänningen, den spänning som krävs för att provbiten ska gå från elastisk, reversibel deformation till plastisk, permanent deformation, samt den totala spänning och töjning som krävs för att materialet ska spricka. Värdena går att jämföra med andra material, men hjälper lite för att förstå mekanismerna. För att vidga förståelsen har vi studerat den lokala fördelningen av spänning och töjning av materialet.

Vi har använt röntgenstrålningsmetoder för att mäta snittförändringar i atomavståndet och hur dess lokala arrangemang ändras. Utifrån detta går det att uppskatta spänning och plastisk deformation lokalt i materialet. Genom att anpassa experimentuppställningarna och dataanalysmetoder efter material med harmoniska strukturer har beteendet i vissa individuella korn samt det genomsnittliga beteendet i grupperna av stora och små korn kunnat studeras. Lokala töjningar har undersökts genom att använda en teknik där små markörer sätts på provbitens yta. Ytan filmas under dragprovstestet, och utifrån markörerna förflyttning relativt varandra beräknas den lokala töjningen.

Genom att kombinera informationen från den lokala spänningen och töjningen kan följande slutsatser dras: Grupperna av stora och små korn töjs lika mycket till en början. Eftersom de stora kornen är omslutna av små korn, tvingas de stora kornen att deformeras elastiskt tillsammans med de små kornen ända tills att de små börjar deformera plastiskt. Det gör att flytspänningen i material med harmonisk struktur är högre än väntat. Därefter beter sig materialet som en kombination av material med bara stora korn och små korn var för sig, ända tills att töjningen börjar koncentrera sig i stora korn. I samband med det sker återigen positiva samverkanseffekter som gör att materialet tål mer plastisk deformation än förväntat. Varför har vi bara fått en översiktlig bild av och det ska studera vidare. Det är mest av akademiskt intresse och inte avgörande ur en praktisk synpunkt, eftersom komponenter ska vara designade så att de inte utsätts för krafter långt över flytspänningen.

List of Papers

Paper I

Separation of XRD peak profiles in single-phase metals with bimodal grain structure to analyze stress partitioning.
E. Sjögren-Levin, W. Pantleon, A. Ahadi, Z. Hegedüs, U. Lienert, N. Tsuji, K. Ameyama and D. Orlov.
IOP Conference Series: Materials Science and Engineering 2022 Vol. 1249 Issue 1 Pages 012040.
https://doi.org/10.1088/1757-899x/1249/1/012040

Paper II

Stress partitioning in harmonic structure materials at the early stages of tensile loading studied in situ by synchrotron X-ray diffraction.
E. Sjögren-Levin, W. Pantleon, A. Ahadi, Z. Hegedüs, U. Lienert, N. Tsuji, K. Ameyama and D. Orlov.
Scripta Materialia 2023 Vol. 226 Pages 115186.
https://doi.org/10.1016/j.scriptamat.2022.115186

Paper III

Grain-level mechanism of plastic deformation in harmonic structure materials revealed by high-resolution X-ray diffraction.
E. Sjögren-Levin, W. Pantleon, A. Ahadi, Z. Hegedüs, U. Lienert, N. Tsuji, K. Ameyama and D. Orlov.
Acta Materialia 2024 Vol. 265 Pages 119623
https://doi.org/10.1016/j.actamat.2023.119623

Paper IV

Mechanics of accelerated strain hardening in harmonic-structure materials.
J. Chatellier, E. Sjögren-Levin, K. Ameyama and D. Orlov.
IOP Conference Series: Materials Science and Engineering 2022 Vol. 1249 Issue 1 Pages 012012
https://doi.org/10.1088/1757-899x/1249/1/012012

Paper V

Strain partitioning and localization characteristics depending on phase fraction distribution in bimodal grain size materials.
E. Sjögren-Levin, J. Chatellier, A. Shokry, P. Ståhle, K. Ameyama and D. Orlov.
in manuscript

Author's contribution to the papers

Paper I

The author fabricated the material, conceptualized and performed the experiment, developed the code, conducted data analysis and wrote the draft.

Paper II

The author fabricated the material, conceptualized and performed the experiment, conducted data analysis and wrote the draft.

Paper III

The author fabricated the material, performed the experiment, conducted data analysis and wrote the draft.

Paper IV

The author jointly conducted data analysis and draft writing.

Paper V

The author jointly conducted data analysis and wrote the draft.

Papers not included in the thesis:

Realization of Ultrahigh Quality InGaN Platelets to be Used as Relaxed Templates for Red Micro-LEDs

Z. Bi, T. Lu, J. Colvin, E. Sjögren, N. Vainorius, A. Gustafsson, J. Johansson, R. Timm, F. Lenrick, R. Wallenberg, B. Monemar and L. Samuelson

ACS Appl. Mater. Interfaces 2020, 12, 15, 17845–17851

https://doi.org/10.1021/acsami.0c00951

Peridynamic Modelling of Harmonic Structured Materials Under High Strain Rate Deformation.

T. S. De Sousa, A. Ahadi, E. Sjögren and D. Orlov.

14th World Congress on Computational Mechanics (WCCM) ECCOMAS Congress 2020 published 2021

https://doi.org/10.23967/wccm-eccomas.2020.279

Abbreviations

DIC	Digital image correlation
EBSD	Electron backscatter diffraction
FCC	Face centre cubic
FE	Finite Element
GND	Geometrically necessary dislocations
KME	Kocks-Mecking-Estrin
PREP	Plasma rotating electrode processing
ROM	Rule of mixtures
SEM	Scanning electron microscope
SPS	Spark plasma sintering
SSD	Statistically stored dislocations
UFG	Ultrafine grain
IP	Initial powder

1 Introduction

High strength and toughness are the desirable set of properties for most structural engineering materials [1]. Unfortunately, enhancing these properties tend to be mutually exclusive. There is a constant strive for stronger and harder materials, but these materials have little to no use as bulk structural materials in safety-critical applications. Strength is necessary for the material to resist permanent (plastic) deformation and toughness is necessary for the material to have the ability to undergo some plastic deformation (have some ductility) and absorb energy before failure. Strong materials tend to have little ability to undergo plastic deformation before failure, the so-called strength-ductility trade-off [1, 2].

Strategies to overcome this trade-off exist in metallic materials are typically based on designing composite-like structures with hard and soft phases. For instance, dual-phase steels consist of a soft matrix of ferrite reinforced with a hard martensitic phase. Strength is provided by the hard phase and once yielding occurs strain is concentrated to the plastically deforming soft phase with good work-hardenability. Microcracks that are prone to nucleate due to stress concentrations and strain incompatibilities between the hard and soft phases can often be blunted by local deformation and work-hardening of the soft phase. This provides further toughness to the material [3].

If a strong and ductile single-phase (or chemically homogenous) metal is to be used, there are fewer options at hand. Already in the 1950s, it was shown by Hall [4] and Petch [5] that the yield strength increases with decreasing grain size. This led to the research field of severe plastic deformation techniques that aims to reduce the grain size to ultrafine grains (UFGs) ≤ 1 μm or nano crystals ≤ 100 nm [6]. At such small grain sizes, the yield strength increases dramatically but the ability of the grains to store dislocations and thus to work-harden becomes reduced. This makes the specimen sensitive to flaws at the surface and the interior, which can, particularly in tensile tests, initialize localized deformation leading to short uniform elongation and fracture at low plastic strains [7]. In order to increase the work-hardening capability and to suppress strain localization, several methods have been developed based on designing microstructures with both coarse and fine grains. Similar to dual-phase steels, these microstructures with bimodal or heterogenous grain size distributions consist of a strong and a soft phase. With the difference being that the variance in strength emerges from differences in grain size instead of

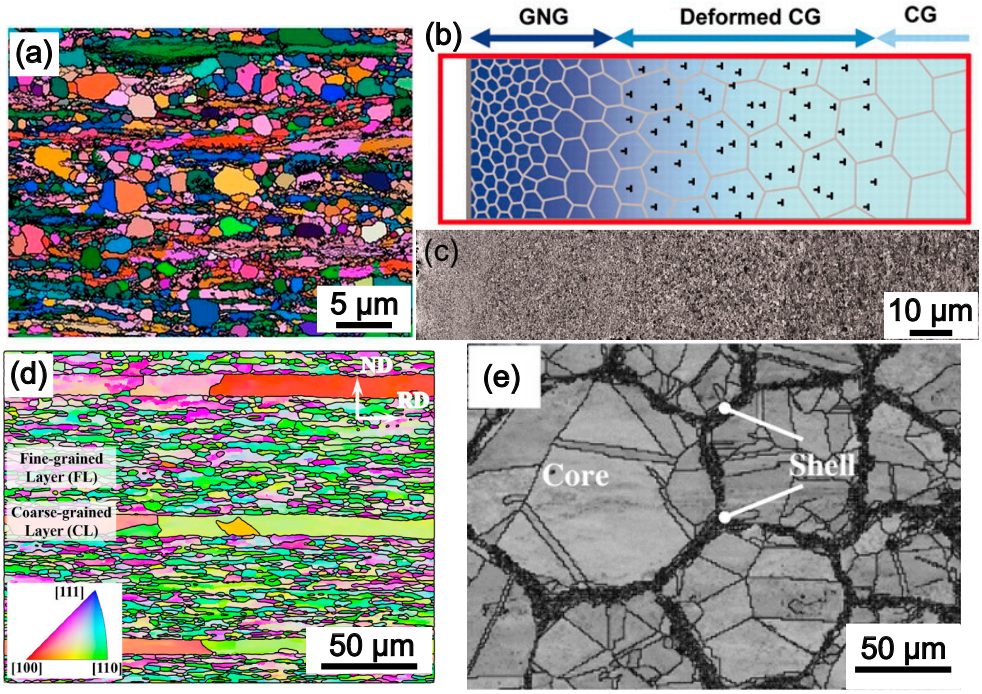

Figure 1.1 Examples of heterogeneous structures. Electron backscatter diffraction micrographs of heterogenous lamella (a) laminate structure (d) and harmonic structure modified from [8, 9] [10] respectively. Schematic of gradient structure cross-section (b) showing gradient nanograined (GNG) layer in dark blue and deformed coarse-grained layer in light blue, and typical scanning electron microscope image in (c) adapted from [11]. Figures (d) reprinted from [9] with permission from Elsevier and (e) from [10] with permission from SNCSC. Figures (b,d) from [11]. Reprinted with permission from AAAS.

crystallography and chemical composition, meaning that the phases have equal Youngs modulus.

Several heterogenous structures with different architectures have emerged during the last decade with heterogenous lamella, gradient materials, laminate and harmonic structures being the most common examples in review papers [12-15]. The architectures are shown in Figure 1.1. Heterogenous lamella (Figure 1.1a) consist of soft lamellae of a few microns grains completely embedded in hard lamellae of UFGs [8]. Gradient structure (Figure 1.1b, c) typically has a nanocrystalline surface with a gradual increase in grain size to the central part of a sheet where grains are relatively coarse [16]. Laminate structures (Figure 1.1d) consist of two-dimensional layers of either dissimilar materials [14] or the same material but varying grain size [9] that are staked. Harmonic structures (Figure 1.1e) constitute of a three-dimensional network of fine grains that encapsulate islands of coarse grains [17].

All of the above architectures have shown to be successful in providing high strength with good ductility. The connecting feature of the architectures is that the work-hardening rate seems to increase more than expected from the individual grain fractions such that the strength and ductility are higher than predicted from rule of mixtures [15]. Nevertheless, the deformation mechanisms of each individual architecture are far from understood and it remains an open question which one is the best at providing strength and ductility. This thesis focuses on understanding the deformation behaviour of harmonic structures under tensile testing.

As a last detour before delving into the meat of this thesis topic one may wonder where these heterogenous structures may find application? At this stage, it is difficult to forecast where such cutting-edge materials can be used as the industrial adaptation may take decades. If the production of any of the architectures meet the industrial demand of economic viability and reproducibility, they may find their use in applications where the manufacturer, for some reason, is restricted to a particular chemical composition. This could for instance be in the food industry, where the alloys allowed to be in contact with food are regulated by authorities [18], or in the biomedical industry where there is a limited number of alloys acceptable to be implanted in the body [19]. In such cases, the structural properties of the material can only be tailored with processing techniques. If the requirement of single-phase and chemical homogeneity is omitted, the architectures may be incorporated in already existing multi-phase materials as an additional improvement in mechanical properties.

1.1 Scope of the work

This thesis focuses on investigating the deformation mechanisms of pure nickel with harmonic structure under tensile testing. Nickel was chosen as a model material because it is a well-studied single-phase material of face centre cubic crystal system that does not undergo phase transformations upon straining. This allows us to study the effect of grain size variation on the mechanical behaviour in isolation. Key factors for understanding the deformation mechanisms of harmonic structures are the distributions of stresses and strains. Therefore, we have employed *in situ* high-energy X-ray diffraction experiments for studying the stress partitioning in the bulk and digital image correlation experiments to study the strain partitioning on the surface. The early stages of deformation are the primary focus as it is the most critical for efficient use of harmonic structure materials. With detailed understanding of the mechanical behaviour close to the yield strength, the potential use of the harmonic structure material can be optimised. It enables lower safety-margins which reduce material usage and improves sustainability. One of the most efficient methods, high resolution reciprocal space mapping, to study the elastic-plastic transition have been used. Furthermore, better understanding of the

deformation mechanisms of harmonic structures gives guidance on how to tailor the microstructure for optimal mechanical properties. Additionally, the deformation mechanisms may be common for many heterogenous structures, and the findings may be useful for the optimization of other architectures.

2 Background

This aim of this section is to provide the overview of deformation mechanism in heterogenous metals during tensile deformation. It highlights gaps in the literature and clarifies the selection of studies (and methods) in this work. This section begins with briefly outlining some general concepts in physical metallurgy, follows with introducing the deformation mechanisms of metals with typical homogeneous grain size distributions, and ends with a literature review on the deformation mechanism of heterogenous materials.

2.1 Fundamentals

The behaviour of a material is to a large extent dependent on the arrangement of atoms. Atoms in metals are arranged in a periodic structure called a crystal lattice with the smallest repeating unit called "unit cell". Nickel has the same unit cell with face-centred cubic (FCC) symmetry, independent of temperatures and pressures. The FCC crystal structure is illustrated in Figure 2.1a and is characterized by three orthogonal crystal axe ($\mathbf{a_1}$, $\mathbf{a_2}$, $\mathbf{a_3}$) of the same unit cell length called the lattice constant a (a=3.524 Å for nickel [20]) such that the unit cell forms a cube. The atoms are positioned at the corner of the cube and in the centre of each face. Miller indices are used to describe directions and planes in the crystal lattice. The directions are denoted by [uvw] where [1 0 0] is parallel with $\mathbf{a_1}$ and [1 1 0] lies in between $\mathbf{a_1}$ and $\mathbf{a_2}$ as illustrated in Figure 2.1a. Symmetrically equivalent directions are denoted by <uvw>. Lattice planes are denoted by Miller indices (hkl) and are defined by the position where the plane intersects the crystal axis. Symmetrically equivalent planes are denoted by{hkl}. For cubic lattices the lattice plane normal are parallel to the crystal direction. The (111) plane is illustrated in Figure 2.1b. The distance between lattice planes is given by

$$d_{hkl} = \frac{a}{\sqrt{h^2 + k^2 + l^2}}. \tag{2.1}$$

Real crystals contain defects of several different types. One type, dislocations, is particularly important for the plastic deformation of metals. A dislocation is a

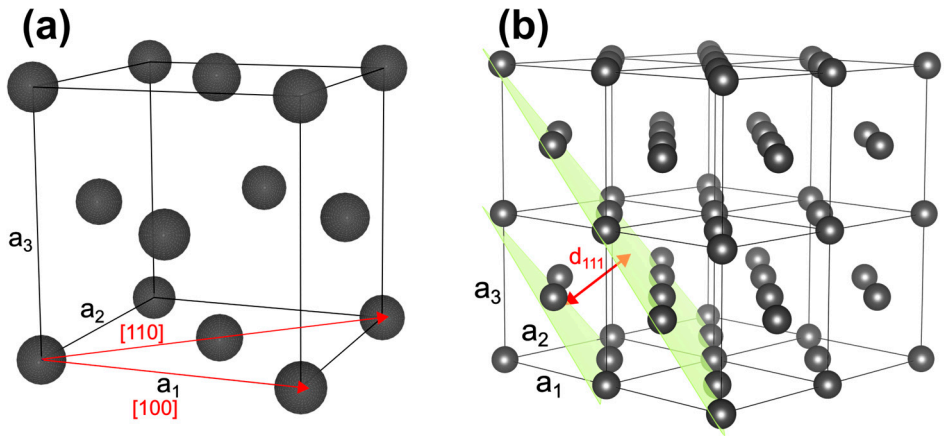

Figure 2.1 Illustraintion of the atomic arrangement in an FCC unit cell (a, b) indicating [100] and [110] directions (a), and (111) lattice plane (b).

one-dimensional defect along a (dislocation) line where the atoms are displaced from their ideal position [21]. The magnitude and the direction of atom displacement is characterized by the Burgers vector. The dislocation gives rise to the displacement of surrounding atoms. The description of displacement is often divided into one part describing the core of a dislocation and another part describing the displacement further away. The positions of atoms close to the core are difficult to predict, while elastic theory can be applied on the atoms far away. This allows the prediction of displacement, stress, and strain fields around several types of dislocation. An important general feature is that the stress/strain fields of a dislocation is long-range, as the fields decay with 1/r where r is the distance from the dislocation core. Thus, the dislocation is associated with an accumulated strain energy that increases with the size of the crystal. A real crystal contains many dislocations, that experience long-range interactions with each another. The dislocations can be arranged in several configurations such that the strain fields cancel one another, which reduces the strain energy compared to a single dislocation [22].

A crystalline solid can consist of a single crystal, which means the same periodic arrangement extends throughout the solid. However, most metallic solids are polycrystals, meaning that they are composed of at least several crystals. The individual crystals are called grains, and have different crystallographic orientations relative to a reference frame of the solid. The periodic pattern of atoms in different grains breaks down along a two-dimensional surface called ‘grain boundary’. Grains are further categorized into grains and subgrains, commonly depending on misorientation across the boundary with a threshold of 15 ° [21]. The mechanical properties of a metal alter significantly depending on the average grain size, which will be discussed in detail later.

2.2 Mechanical behaviour

This section aims to provide an overview of the current understanding of the deformation mechanism of heterogenous metals during tensile deformation. However, to highlight the unique deformation mechanism of heterogenous structures, an overview of the most common deformation mechanism of materials with homogenous coarse and fine grains are first provided.

2.2.1 Stress and strain

Metallic solids deform when subjected to an external load. This section describes the concepts of stress and strain.

Forces acting on the surface of a body are defined by force per unit spatial area called external traction vector [23]. In order to link the external traction acting on the surface of a body with its interior, the concept of internal traction is introduced. The point of any one body is held together by a continuous distribution of tractions, $\boldsymbol{t_n}$ belonging to real space, acting across the imaginary internal surface of the body. The traction acting on a plane passing through a point $\boldsymbol{x} = [x \quad y \quad z]^T$ with unit normal $\hat{\boldsymbol{n}}$ is described by the stress tensor

$$\boldsymbol{\sigma} = \begin{bmatrix} \sigma_{11} & \sigma_{12} & \sigma_{13} \\ \sigma_{21} & \sigma_{22} & \sigma_{23} \\ \sigma_{31} & \sigma_{32} & \sigma_{33} \end{bmatrix}, \tag{2.2}$$

such that the traction of the plane is given by

$$\boldsymbol{t_n} = \boldsymbol{\sigma}\hat{\boldsymbol{n}}. \tag{2.3}$$

The traction vector can be decomposed into two components. The normal stress $\boldsymbol{t_n}$ parallel to $\hat{\boldsymbol{n}}$ and the shear stress perpendicular to $\hat{\boldsymbol{n}}$. The diagonal stresses in the stress tensor are axial stresses and the off diagonal are shear stresses. It is important to note that any plane can be chosen, the magnitudes of the components of the stress tensor depends on the coordinate system and thus is a function of $\hat{\boldsymbol{n}}$. It is possible to find a plane $\hat{\boldsymbol{n}}$ of principal axis such that the shear components vanish and only the normal stresses $(\sigma_{11}, \sigma_{22}, \sigma_{33})$, now called principal stresses $(\sigma_1, \sigma_2, \sigma_3)$, are left [23]. The stress tensor can be decomposed in a hydrostatic (trace of the stress tensor) and a deviatoric part. The hydrostatic part describes change of volume and the deviatoric change of shape.

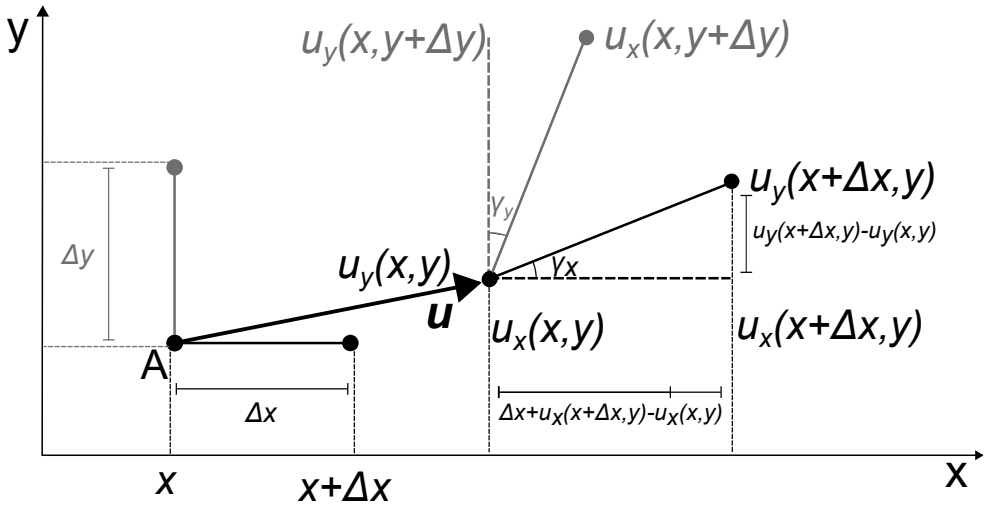

Figure 2.2 Two initially orthogonal line elements of infinitesimal length Δx and Δy becoming deformed by displacement field $\boldsymbol{u}$.

Material points in a body undergo displacement when subjected to an external load. The material points may translate in space or undergo deformation. The deformation, that is, change of volume and/or shape is described by the concept of strain. The body is imagined as a collection of small line elements originating at the material points. The strain at a point is completely characterized by the movement of three mutually perpendicular line segments. The line segments can change length by undergoing normal strains, and/or change the angle between two initially perpendicular line segments by undergoing shear strains [24].

The concept is described by considering a two-dimensional case shown in Figure 2.2. Two perpendicular line element of lengths Δx and Δy starting at point A (x, y) undergoes a displacement by the displacement field $\boldsymbol{u} = u_x(x, y) + u_y(x, y)$.

First, the movement along the x-direction is considered. The starting point undergoes displacement $u_x(x, y)$ and the end of the line segment $u_x(x + \Delta x, y)$. The normal strain is

$$\epsilon_{xx} = \frac{u_x(x + \Delta x, y) - u_x(x, y)}{\Delta x}, \tag{2.4}$$

which as $\Delta x \to 0$ becomes

$$\epsilon_{xx} = \frac{\partial u_x}{\partial x}. \tag{2.5}$$

Second, the movement in the y-direction along $x + \Delta x$ is considered. The starting point undergoes displacement $u_y(x, y)$ and the end of the line segment $u_y(x + \Delta x, y)$, resulting in the line segment rotating an angle

$$\tan(\gamma_x) = \frac{u_y(x + \Delta x, y) - u_y(x, y)}{\Delta x + u_x(x + \Delta x, y) - u_x(x, y)} \tag{2.6}$$

$$= \frac{\frac{u_y(x + \Delta x, y) - u_y(x, y)}{\Delta x}}{1 + \frac{u_x(x + \Delta x, y) - u_x(x, y)}{\Delta x}},$$

which as $\Delta x \to 0$, and with the approximation $\epsilon_{xx} \ll 1$ becomes

$$\gamma_x = \frac{\frac{\partial u_y}{\partial x}}{1 + \frac{\partial u_x}{\partial x}} = \frac{\frac{\partial u_y}{\partial x}}{1 + \epsilon_{xx}} \approx \frac{\partial u_y}{\partial x}. \tag{2.7}$$

Similar derivations of movement in the y direction and in the x-direction along $y + \Delta y$ lead to

$$\epsilon_{yy} = \frac{\partial u_y}{\partial y}, \tag{2.8}$$

$$\gamma_y \approx \frac{\partial u_x}{\partial y}. \tag{2.9}$$

The shear strain is

$$\epsilon_{xy} = \frac{1}{2}(\gamma_x + \gamma_y). \tag{2.10}$$

These partial derivatives are displacement gradients measuring how rapid the displacement change through the material which is equivalent to strain [24]. The concept is easily extended to three dimensions, such that the full strain tensor is

$$\epsilon = \begin{bmatrix} \epsilon_{xx} & \epsilon_{xy} & \epsilon_{xz} \\ \epsilon_{yx} & \epsilon_{yy} & \epsilon_{yz} \\ \epsilon_{zx} & \epsilon_{zy} & \epsilon_{zz} \end{bmatrix}. \tag{2.11}$$

2.2.2 Stress-strain relationship

The stress tensor and the strain tensor are related. When the stress is relatively small the deformation or strain is purely elastic. As soon as the external stress is removed, a solid recovers its original shape. For many materials, the stress and strain are approximately linearly related in the region of elastic strain, such that the stress components are linearly related to strain by the generalized Hooke's law

$$\boldsymbol{\sigma_{ij} = C_{ijkl}\epsilon_{kl}}, \tag{2.12}$$

where $\boldsymbol{C_{ijkl}}$ is a fourth-order tensor field, which considers that the material may have different properties in different directions [25].

For many materials it is reasonable to approximate the material as isotropic having the same properties in all directions. For such materials it is sufficient to describe the stress-strain relation through a uniaxial tensile test [26]. A uniaxial load F applied to a solid specimen with an initial cross section A_0 gives rise to an applied stress, or an engineering stress

$$\sigma = F/A_0. \tag{2.13}$$

The applied stress makes the specimen to elongate from an initial length L_0 to a length L along the tensile axis. The relative elongation is assumed to be homogenously distributed over the solid and is expressed as engineering strain

$$\epsilon = (L - L_0)/L_0, \tag{2.14}$$

or true strain, where the change in length is divided by the current length $dL = dL/L$ such that total elongation is

$$\epsilon_t = \int_{L_o}^{L} \frac{dL}{L} = ln(\frac{L}{L_0}). \tag{2.15}$$

With increasing strain, the cross-sectional area, A, decreases such that the engineering stress is different from the true stress. For as long as the deformation is uniform, it is possible to calculate the true stress by

$$\sigma_t = \sigma(1 + \epsilon) \tag{2.16}$$

under the assumption of constant volume $LA = L_0A_0$.

The stress and strain are plotted in a diagram as shown in Figure 2.3a. When the stress is sufficiently small, the strain is purely elastic, so the stress and strain are approximately linearly related as described by the Hooke's law

$$\sigma = E\epsilon, \tag{2.17}$$

where E is the Young's modulus.

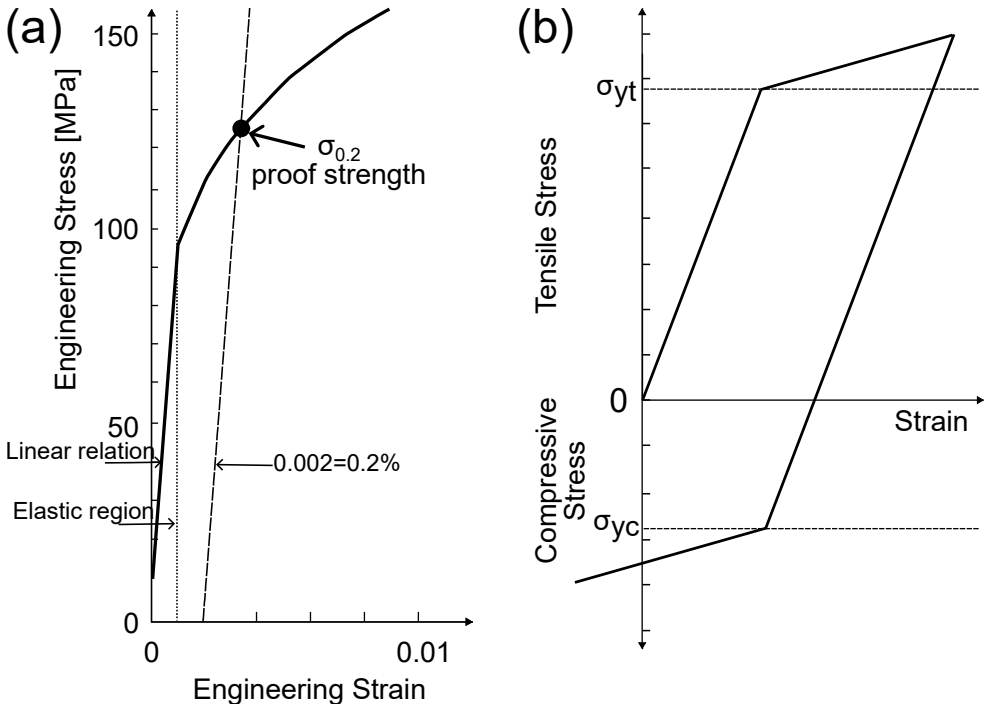

Figure 2.3 Initial part of a stress-strain curve (a). Illustration of the Bauschinger effect (b).

With further increase of stress, the stress passes the materials 'yield stress' σ_y, and the deformation becomes plastic, which means the solid specimen does not recover its original shape fully after unloading, and the relation between stress and strain becomes non-linear. With increasing amount of plastic deformation, an increasing (flow) stress is required to continue plastic deformation. This is due to work hardening, which is typical for most metals.

The transition from elastic to plastic deformation is gradual for many metals and the yield stress σ_y is not uniquely defined. Often the 0.2% proof stress $\sigma_{0.2}$ is taken as σ_y. Figure 2.3a illustrates the definition of $\sigma_{0.2}$, it is the stress where a line parallel to the linear part of the stress-strain curve offset at 0.2% strain intersects the stress-strain curve.

Figure 2.3b illustrates that a metal deformed in tension beyond its tensile yield stress σ_{yt}, may exhibit a lower compressive yield stress σ_{yc} upon subsequent loading in the opposite direction. This reduction in resistance to deformation upon load reversal is known as the Bauschinger effect [27]. The effect is frequently observed in polycrystalline alloys [28], pure metals [29], and even single crystals [30]. There are several theories to explain the effect [31], one of which will be discussed in section 2.2.6.3.

2.2.3 Dislocation glide

In order for metals to change shape permanently, atoms need to be moved relative to one another. FCC metals such as nickel predominately undergo plastic deformation via a process called dislocation glide. Dislocations move on slip planes defined as planes that contain the dislocation line and the Burgers vector [32]. The direction of the Burgers vector is the slip direction. The dislocation line and the Burgers vector can be either parallel, perpendicular, or a mix of both to one another. The combination of a particular slip plane and slip direction is termed a slip system. Dislocations tend to move on close-packed planes along close-packed directions. Close-packed planes have the highest density of atoms and largest spacing. For FCC crystals the most common slip plane is of type {111} and the slip direction is of type <110>, such a direction and plane are shown in Figure 2.1a and b, respectively.

During the process of dislocation glide, the part of a crystal on either side of the slip plane becomes displaced relative to one another for a Burgers vector distance once the dislocation reaches the surface [32]. The dislocation line marks the boundary between slipped and non-slipped areas in the crystal. Dislocation slip (or glide) involves breaking and formation of atomic bonds, which forms a lattice friction. The dislocation slip is driven by a resolved shear stress on the slip plane, which is present even though the external loading is not in a shear mode.

Figure 2.4 shows a slip plane in a cylindrical crystal of cross-sectional area A_0, which is subjected to a uniaxial tension F. The resolved shear force in the slip direction is $Fcos(\lambda)$, where λ is the angle between the tensile axis and the slip direction, and the resolved slip plane area is $A = A_0/cos(\phi)$, where ϕ is the angle between the tensile axis and the slip plane normal. Thus, the resolved shear stress (τ_{rss}) is related to the tensile stress by

$$\tau_{rss} = \frac{F}{A}cos(\lambda) = \sigma cos(\phi)cos(\lambda). \tag{2.18}$$

The resolved shear stress on the slip plane in the slip direction needs to be larger than a 'critical resolved shear stress' (stemming from the lattice friction) necessary to initiate a dislocation to slip [32]. The magnitude of resolved shear stress clearly depends on the orientation of the slip system (and consequently also the grains orientation) relative to the tensile axis.

The net result of dislocation glide is that the slip planes appear to have sheared over each other in the slip direction. If the individual grains would have no geometrical constraints, the grain would change shape "sideways" relative to the direction of applied load. However, in practice, the specimen ends are constrained by grips in a uniaxial tensile test, which forces the deforming part of the specimen to rotate relative to the direction of applied load [33] In a polycrystal, the grains are forced to rotate due to geometrical constrains by neighbouring grains, since they must deform compatibly.

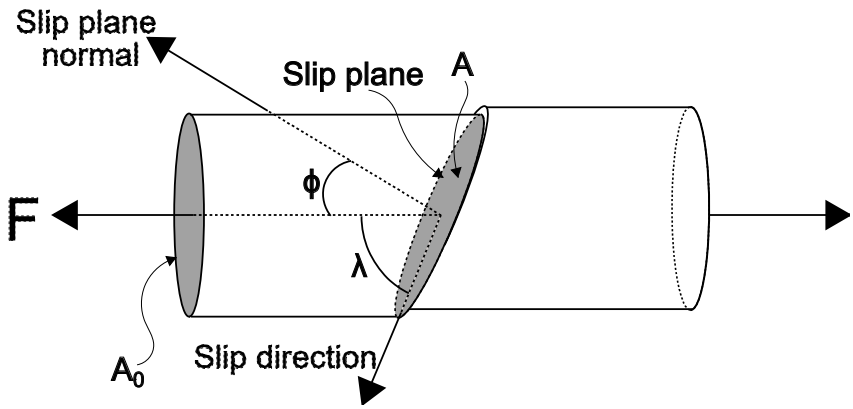

Figure 2.4 Relation between slip plane, slip direction and tensile axis for calculation of resolved shear stress.

2.2.4 Evolution of microstructure

During deformation, dislocations multiply and become stored in ductile metals [34]. As previously mentioned, dislocations interact with one-another and organize into arrangements to reduce their total strain energy, so called dislocation structures [35]. The morphology of dislocation structures depends on material and the orientation of grains relative to the load axis, deformation mode and the amount of strain [36].

Dislocations in FCC metals such as nickel, copper and aluminium are mobile in three dimensions and tend to self-organize into cell structures [36]. The three-dimensional mobility originates from that the parts of a dislocation line that are parallel to the Burgers vector can swich from one {111} type plane to another in a process known as cross-slip [37]. Cell structures consist of dislocation rich walls and nearly dislocation free interiors. The cell walls are formed by the statistical mutual trapping of glide dislocations and induce a small rotation angle between neighbouring cells [38]. The cell structures are often hierarchical on the scale of a grain, with the cells grouped into blocks of small misorientation angles between each cell and the blocks separated by dislocation walls with larger misorientation angles [39].

The large misorientation between cell blocks originates from that different combination of slip systems are activated in different parts of the grain. Homogenous deformation of a grain occurs if at least 5 slip systems are activated [40, 41], which is known as the Taylor criterion. However, not all 5 slip systems need to be activated over the whole volume of the crystal at once to fulfil the criterion. Different volumes of an individual grain can have less than five slip systems operating as long as all volumes fulfil the criterion collectively [39]. With different slip systems operating, large misorientation develops between the cell blocks. With strain increase, the

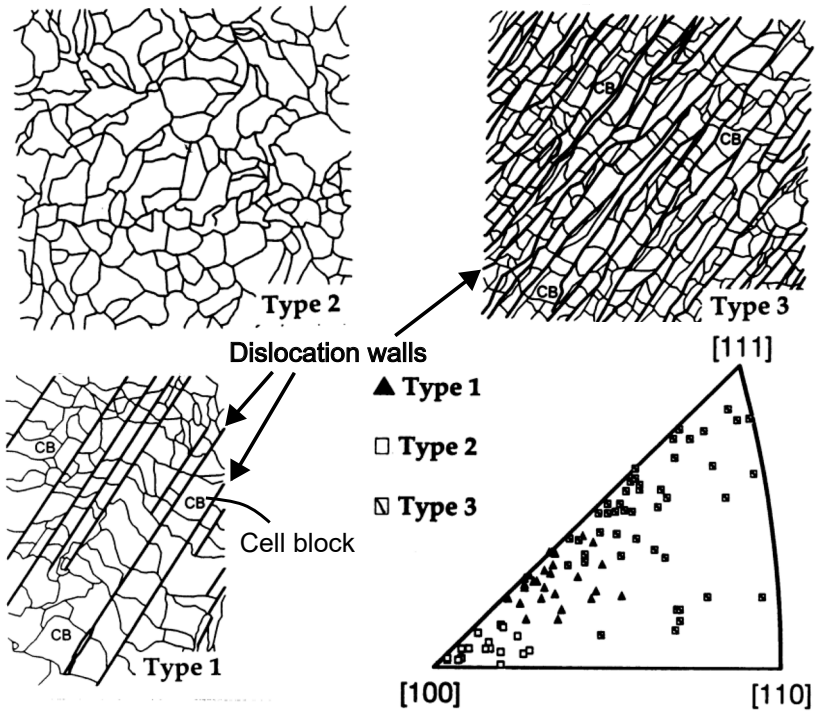

Figure 2.5 Three morphological types of dislocation structures in tensile strains polycrystalline pure aluminum. The relation between type of dislocation structure and the direction of tensile axis with respect to the crystal is shown in the stereographic triangle. Reprinted from [42] with permission from Elsevier.

misorientation between cell blocks increase, and the block size decrease. This is also true for the individual cells. However, the rates of misorientation and cell size changes are different for cells and cell blocks [42].

The morphology of the dislocation structure depends on the orientation of the grain with respect to the load axis as the combination of slip systems change [42]. Three different types of microstructures have been identified based on the tensile axis orientation in the stereographic triangle, as shown in Figure 2.5. The type 1 structure forms when the tensile axis is parallel with the central part of the stereographic triangle, type 2 forms within 15° of the [100] corner and type 3 within 20° of the [111] corner. The type 1 structure consists of cell blocks containing cells that are separated by curved cell walls. The cell blocks are separated by extended planar walls almost parallel to a (111) plane. Similarly, the type 3 structure consists of cell blocks separated by extended walls, but the walls are less planar and are not parallel to a slip plane. The type 2 structure is a cell structure without extended planar walls. Grains with the tensile axis parallel to a [100] crystal axis will be analysed in detail later in the thesis (***Paper III***).

2.2.5 Hall-Petch relationship

In the 1950s, Hall [4] and Petch [5] showed that the yield strength of mild steels is related to their average grain size, D, by the now called Hall-Petch relationship

$$\sigma_y = \sigma_0 + K_{HP}\left(\frac{1}{D}\right)^{1/2}. \tag{2.19}$$

where σ_0 and K_{HP} are experimental constants. Later it was shown that the relationship holds for other pure metals and alloys [43]. Despite several decades of research, consensus has not been reached on the exact mechanism behind the relationship. Several review papers [44-46] that summarize various models and discusses their correctness have been published in recent years. Delving into this topic in detail is outside the scope of this thesis work. Nevertheless, in brief, high-angle grain boundaries act as obstacles for dislocation slip as a slip system necessarily need to change when passing from one grain to another. The local stress at the grain boundary needs to increase for plastic flow to transmit to the next [47]. The constant K_{HP} and exponent are related to the grain boundary strengthening whereas all other strengthening mechanisms are incorporated in σ_0 [44].

2.2.6 Work-hardening, dislocation density and grain sizes

As already noted, the dislocation density increases with plastic strain, and is defined as the length of dislocation lines per unit volume. The stress and strain fields from a dislocation causes the dislocation to act as an obstacle for other gliding dislocations. Hence, a higher applied stress is needed to move a mobile dislocation past the stuck one. The shear flow stress τ is proportional to the mean distance between dislocations ($\approx \sqrt{\rho}$) according to the Taylor relation

$$\tau = \tau_0 + aGb\sqrt{\rho}. \tag{2.20}$$

where b is the magnitude of the Burgers vector, G is the shear modulus, a is related to the geometrical arrangement of dislocations and τ_0 is the internal friction stress [48]. The relation is extended to polycrystals by introducing the Taylor factor M. This factor relates the axial strains to the total shear strain on all active slip systems in the grains, and thus the macroscopic flow stress to the shear stress in slip systems [41].

$$\sigma = \sigma_0 + MaGb\sqrt{\rho}. \tag{2.21}$$

Thus, it is easily understood that the flow stress increase with plastic deformation as the dislocation density increase.

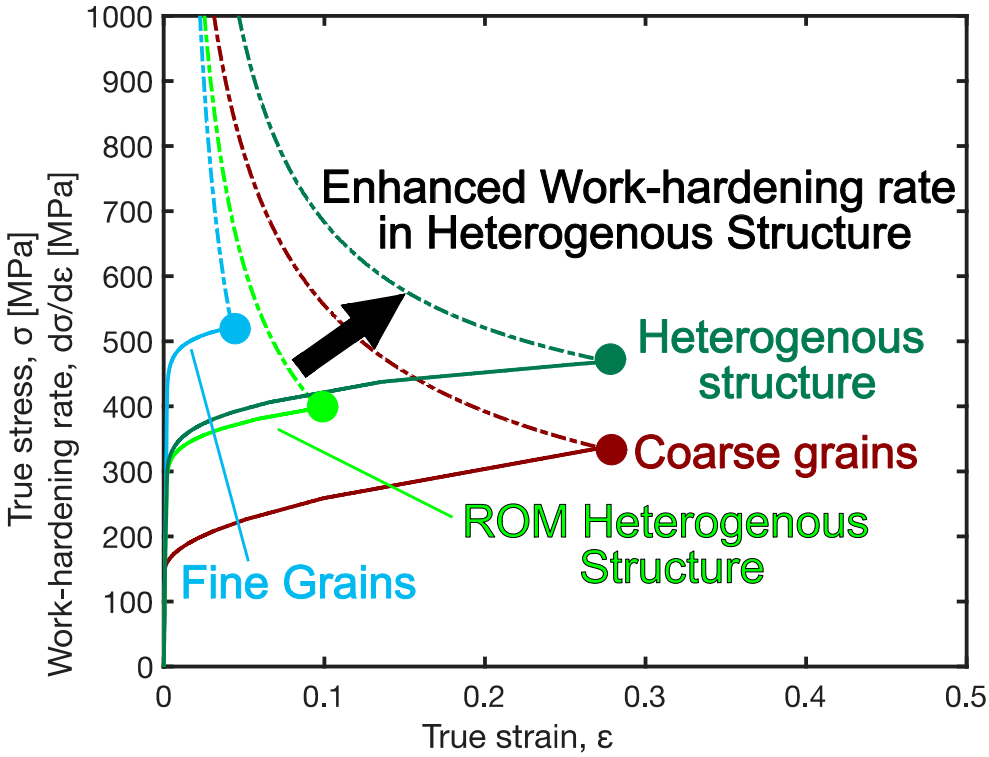

Figure 2.6 Illustration of true stress-strain in solid curves and corresponding work-hardening rate in dashed curves of microstructures with homogenous fine and coarse grains, theoretical heterogenous structures based on rule of mixtures (ROM Heterogenous structure) and practical tests (Heterogenous structure).

The evolution of dislocation density is grain size dependent as we shall see later. This causes the stress-strain curves to also be grain size dependent. Schematics of typical stress-strain curves of homogenous coarse-grained metals and fine-grained metals are shown in Figure 2.6. It can be seen that yield strength is higher for the fine-grained metal than for the coarse-grained counterpart, as expected from the Hall-Petch relationship. The flow stress (seen from the higher work-hardening rate) also increases faster with strain, and the fine-grained metal fractures at lower strains. The two last observations are discussed below. The curves denoted ROM heterogenous structure and heterogenous structure will be discussed later.

2.2.6.1 Kocks-Mecking-Estrin model

Work-hardening is related to the dislocation density and dislocation structure [42, 49-52]. One popular model to describe the work-hardening (increasing flow stress) in tensile test is the Kocks-Mecking-Estrin (KME) model [53]. The model assumes the evolution of dislocation density as the governing parameter for the increasing flow stress and ignores all other sources of resistance to dislocations glide. The

model is suitable for describing tensile test since the specimen often fractures before reaching the stage of deformation where the dislocation structure is necessary to incorporate [54]. In the KME model, the average spacing between dislocations is assumed to be proportional to $1/\sqrt{\rho}$ irrespective to the dislocation arrangement in a random structure or a cell structure. The evolution of dislocation density with strain is controlled by the competing processes of storage and recovery, where the storage is associated with the immobilization of moving dislocations after traveling a mean free path. The mean free path is proportional to the average spacing between dislocations and other obstacles. The only obstacle apart from other dislocations are grain boundaries in single-phase metals. The evolution of dislocation density is described by

$$\frac{d\rho}{d\epsilon} = \mathrm{k} + k_1\sqrt{\rho} - k_2\rho. \tag{2.22}$$

The three coefficients denote probabilities of dislocations storage at grain boundaries, by other dislocations, and annihilation due to dynamic recovery, respectively. The probability of dislocation storage due to grain boundaries is proportional to the grain size *D* through a relationship $k = \frac{1}{b\mathrm{D}}$.

From the above relation it is clear that a metal with smaller grain size, with all other factors unchanged, should increase its dislocation density faster than a metal with large grains, and thus have a higher work-hardening rate, as supported in literature [54]. However, the high rate of dislocation storage does not continue to large strains. It has been reported that metals of nanocrystals and UFGs show virtually no work-hardening beyond the initial stage of rapid work-hardening in the strain regime of (1-3%) [55]. The dislocation density saturates because dislocations are generated and annihilated at the same rate. It has been suggested that the grain boundaries act as sources and sinks of dislocations as these are sites where dislocations are readily generated and annihilated [55, 56]. Thus, dislocations can travel through the grain without interacting, which does not lead to an increase in dislocation density.

A recent study where the KME coefficients were used for fitting tensile stress-strain curves of nickel with average grain sizes varying from 0.78 μm to 105 μm showed that the coefficients vary with grain size [54]. Interestingly, the coefficient k_2 increases sharply in the range of 0.78-1.32 μm while insensitive to grain size in the range of 4-105 μm. The difference was attributed to thermally activation of dislocation annihilation at the grain boundaries. This mechanism dominates ultrafine-grained metals, while dislocation interaction in the grain interior plays a major role in large grains [57].

2.2.6.2 Statistically stored and geometrically necessary dislocation

Additional to the KME model, other theories exist for explaining the higher work-hardening rate of polycrystals when grain size is small. The previously mentioned Taylor model assumes homogenous deformation (of all grains in a polycrystal) [58].

Ashby pointed out that a metal containing components with different resistance to plastic deformation cannot deform homogenously [59]. Such a component can be non-deformable particles, phase or even grains. The grains in a polycrystal deform by different amounts, depending on their orientations and the constraints imposed by their neighbours. Whenever components with different resistance to plastic deformation exist in the microstructure, gradients in strains are introduced, although the imposed global deformation is uniform, as in a tensile test. The local strain gradients create a lattice curvature in the deformable matrix, which is associated with a lattice rotation. The number of dislocations needed to produce the lattice curvature are called geometrically necessary dislocations (GND). The lattice curvature, lattice rotation and gradient in plastic shear strain are linked such that the density of GND can be calculated directly from the strain gradient.

Theoretically, all individual dislocations are geometrically necessary because they assure the local deformation with respect to its surrounding [58]. However, at group level, collections of dislocations may have different properties. A group of dislocations that produce a lattice curvature and have a large net Burgers vector are geometrically necessary. Dislocations may still be present in large numbers without having a net Burgers vector and producing lattice curvature or lattice rotations. This group is called statistically stored dislocations (SSD) since they accumulate due to random mutual trapping of dislocations [59]. The aforementioned cell walls fall into the category of SSD [59, 60].

In Ashby's model, the deformation of plastically non-homogenous metal can be divided into two parts. A part where a uniform deformation is achieved by shear on one or several slip systems such that the density SSD accumulates, and a part of local non-uniform deformation during which the density of GND accumulates [59]. The individual grains in a polycrystal are first let to deform uniformly without considering compatibility and equilibrium conditions [59, 61]. Compatibility is then ensured by introducing a density of GND by filling in or hollowing out voids and overlap that otherwise would be created near grain boundaries [61]. Thus, it is expected that the density of GND gives rise to an increased dislocation density and lattice rotation at grain boundaries and triple junctions [62]. The amounts of voids and overlaps are related to the grain size D and the axial strain ε such that the density of GND evolves as

$$\rho_G \simeq \frac{\varepsilon}{4bD}. \tag{2.23}$$

In Ashby's model, the density of GND is the grain size dependent part of the work-hardening in polycrystals. Assuming the Taylor relationship between flow stress and dislocation density holds, the GND add to work-hardening by increasing the total dislocation density. GND are also assumed to produce long-range internal stresses (since their net Burgers vector is not zero). However, Ashby did not take the long-range stresses into account as their contribution to the flow stress was not clear [59].

The storage of GND and SSD is proportional to the inverse of their respective slip distances, the distance travelled before becoming trapped. The slip distance of GND is independent of strain, as it is proportional to the grain size, while the slip distance of SSD shortens with strain due to the increasing dislocation density [59]. At small strains, GND dominate the total dislocation density but are overturned by the SSD at large strains [59]. Thus, the Ashby model gives rise to a similar grain size dependency of dislocation storage as the KME-model in terms of a higher work-hardening rate at small strains in polycrystals with small grains compared to large grain counterparts.

2.2.6.3 Composite model

The dislocation network may be importance for explaining observations such as the Bauschinger effect. After some plastic strain, grains with their [100] crystal axes parallel to the tensile axis develop cell structures. The two main components of such structure are shown in Figure 2.7, a dislocation depleted cell interior or subgrain, and a dislocation rich cell wall or dislocation wall. Because of the higher dislocation density, the cell wall has higher resistance to plastic flow than the interior, such that, with increasing applied stress, the cell interior yield while the cell wall deforms elastically. As long as the wall do not deform elastically, gliding dislocations in the cell interior becomes trapped at the interface between the walls and interior [63]. The dislocations at the interface induce elastic stresses such that the stress in the walls increase compared to the applied (experiencing forward stress), and decrease in the interior (experiencing back stress). This ensures compatible deformation of the two components. When the loading direction is reversed, the back stress adds to the applied such that the applied stress required for initiating yielding in the cell interior reduces [64].

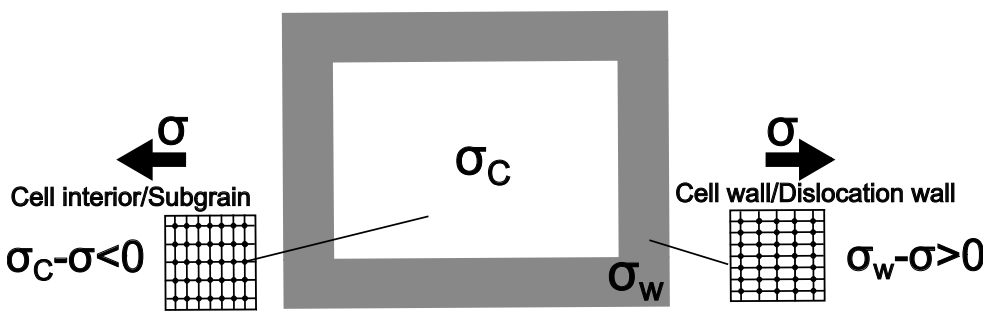

Figure 2.7 Illustration of the composite model of a dislocation structure with cell walls (gray) and cell interiors (white). σ is the applied stress, σ_c and σ_w are the local stress in the interior and wall, respectively. The insets display the difference in elastic strains in the two regions.

2.2.7 Strain localization and fracture

In tensile tests of ductile metals, plastic deformation initiates in the weakest region. The cross-sectional area reduces, but as the region work-hardens it can carry the extra stress. The plastic deformation will then proceed in another weak region, and the cycle is repeated. This type of deformation is stable and uniform on the macroscopic level but is obviously not on the very local level. The plastic deformation continues homogenously macroscopically until plastic instabilities such as necking and shear banding occurs. In necking, strain localizes in a small region known as a "neck" where the cross-sectional area becomes reduced, and essentially all subsequent deformation is concentrated to [65]. Within this region, stress concentration is expected, and thereafter a rapid fracture through void nucleation, growth, and coalescence [66].

Plastic instability is a trade-off during deformation between work-hardening and the level of applied stress [65]. Mathematically, the point of plastic instability can be described by the Considère criterion ($d\sigma/d\epsilon = \sigma$), which states that instability occurs when the work-hardening rate equals to the true stress for strain-rate insensitive materials [67, 68]. Figure 2.6 illustrates that the work-hardening rate of metals tend to decrease with increasing strain while the stress increases. Thus, the two trends cross at some point, and the material becomes plastically unstable, and even a minor defect becomes sufficient to promote localized deformation [65]. As described in previous sections, the yield strength increases with decreasing grain size, and after the initial rapid work-hardening the work-hardening rate decays faster in fine-grained than in coarse-grained metals. This results in that the point of instability is met at lower strains in fine-grained metals than in coarse grained ones.

The strain localization behaviour can be translated from the coarse grain regime to grains in the ultra-fine grain regime. However, when the grain sizes is $\leq$ 300-400 nm, the mode of deformation change [55]. In those grain sizes, strain frequently localizes in the form of shear bands [69-74]. Shear banding is facilitated by the repression of homogenous dislocation slip [75]. Shear bands are narrow zones of concentrated plastic deformations in non-crystallographic bands across the sample and inclined to the loading direction [76]. It must be noted that shear banding also occurs in homogenous coarse-grained metals under high loading rates [65]. As the result of a concentrated plastic deformation, voids grow in the shear band and coalesce along the shear direction due to the shear force and forming crack path [71]. However, the formation of a single shear band does not inevitably lead to a catastrophic failure. It has been shown that the activation of numerous microshear bands in nanocrystalline aluminium alloys supress the transformation to large-scale macro shear banding leading to failure [73, 74].

2.3 Deformation mechanisms in heterogeneous structures

Figure 2.6 illustrates stress-strain curves of heterogenous materials based on practical tests (such as Figure 2.8a) and heterogenous materials based on rule of mixtures (ROM) of the homogenous coarse- and fine- grained metals. Heterogenous materials are expected to have strength, ductility and stress-strain behaviour in between that of coarse and fine grains according to the ROM. Nevertheless, in practice, heterogenous materials can have higher strength and ductility than expected, as shown in the curve denoted heterogenous structure in Figure 2.6. It is attributed to the interplay between the coarse and fine grains during deformation, which enhances the work-hardening rate compared to the mixture of the components. The higher work-hardening rate results in meeting the Considère criterion at higher strains.

Broad trends towards understanding deformation mechanism in heterogenous materials leading to the synergetic interplay between hard and soft zones have been formulated in [12-15, 77-79]. The synergetic interplay is attributed to the inhomogeneous deformations due to the different strength of the constituents. Because of the difference in resistance to applied stress, the soft zone is subjected to higher plastic strains than the hard zone. This leads to strain partitioning and the development of steep strain gradients at a boundary near the zone interfaces. In order to accomplish the strain gradient and to maintain material integrity, a high density of GND form in the boundary vicinity. Such density of GND produce long-range internal stresses that act against the applied stress (back stress) and along the applied stress (forward stress). The back stress strengthens the soft zone lowering the experienced stress and the forward stress weakens the hard zone.

Three stages of deformation have been identified (Figure 2.8b). In stage I, upon global yielding at 0.2% strain, the soft zone deforms plastically, while the hard zone still deforms elastically. When the soft zone is surrounded by hard elastic deforming zones dislocations motion is obstructed by the interface [80]. This causes GND to pile-up at the interface if the metal does not cross-slip, or to accumulate near the interface if the metal is prone to cross-slip [15]. The local configuration of GND exerts back stress in the soft zone, which hinders further emission of dislocations from dislocation sources [80]. This causes the soft zone to appear stronger and to increases the global yield strength.

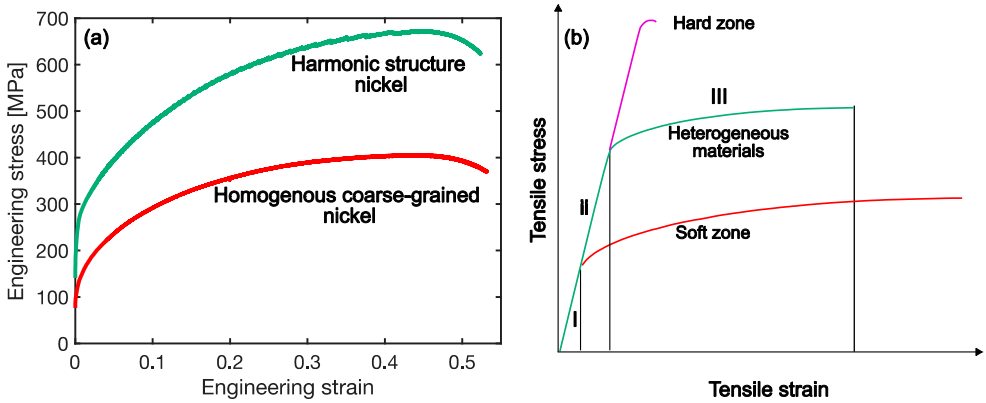

Figure 2.8 Engineering stress-strain curves from tensile tests of harmonic structure and homogenous coarse-grained nickel (a) replotted with data from [81]. Division of the deformation stages in heterogenous materials based on theoretical curve (b) adapted from [78].

In stage II, most of the hard zones deform elastically and gradually become plastic with increasing global strain. This elastic to plastic transition over the strain range results in a high apparent strain hardening [14]. Once both the soft and the hard zones deform plastically in stage III, the extra synergetic work-hardening from the heterogenous structure becomes reduced. The back stress still strengthens the soft zone, but the forward stress weakens the hard zone. This causes the extra work-hardening to increase slowly or even to saturate [14].

In addition to the high work-hardening rate, it has been suggested that heterogenous materials promote strain delocalization, which reduces the propensity of local plastic instabilities leading to rapid failure and thus supports uniform deformation [82]. It has been observed that the formation of local strain bands is promoted in several heterogenous structures (gradient structure nickel [83] and interstitial free steel [84], heterogenous bimodal copper [85] and layered nickel [86]. The strain bands are often about 45° to the loading direction and therefore interpreted as shear bands [15]. Unlike the aforementioned shear bands in nanocrystalline homogenous materials, the strain bands in heterogenous structures are not catastrophic. Instead of a few narrow strain bands, many dispersive strain bands form which causes the strain to delocalize [15].

The formation of shear bands was investigated in the layered nickel [86]. A highly concentrated narrow shear band was observed in the hard zone. Near the interface zone, however, a shear band in the hard zone expanded into a fan-shaped shear band-affected zone as strain transferred from the hard to the soft zone. This led to the blunting of the shear band in the hard zone. Interestingly, there was no evidence of strain concertation in the centre of the soft zone. It must be noted also, the hard zones in heterogenous bimodal copper [85] and layered nickel [86] consists of grains

with a larger size than the typical grain size in homogenous structures prone to the formation of shear bands.

Wang *et al* [85] proposed a mechanism for the formation of disperse strain bands in heterostructures. The accumulated GND near the zone boundaries induce forward stresses, and thus stress concentration at the zone boundary and in the fine-grained zones. The fine-grained zones have exhausted work-hardening capacity and are susceptible for shear instabilities. The shear bands propagate through the fine-grained zone until they are arrested by neighboring coarse-grained zones. This induces additional plastic deformation and work-hardening of the coarse-grained zone, which lowers the stress concentration at the shear bands front. The stress concentration is only reviled locally, meaning that new shear bands can nucleate in other regions until they are dispersed over the whole gauge section.

2.4 Thick and classical yield surfaces

Mechanical testing is typically carried out under simple conditions such as uniaxial tension. In engineering applications, the components are subjected to the combination of stresses. The deformation is described by fundamental deformation theory within continuum mechanics.

In order to determine the onset of plastic deformation under any given combination of stresses, the concept of yield criteria is introduced. One of several yield criteria is the von Mises yield criterion. The criterion assumes that yielding occurs when the shear energy per unit volume of material reaches a critical value given by the constant k [33]. In principal stress axis the criterion is

$$(\sigma_1 - \sigma_2)^2 + (\sigma_2 - \sigma_3)^2 + (\sigma_3 - \sigma_1)^2 = k, \qquad (2.24)$$

where $\mathrm{k} = 2{\sigma_y}^2$. The criterion can be described as a surface in principal stress space. This yield surface takes, as Figure 2.9a shows, the form of a cylinder along the hydrostatic axis $\sigma_1 = \sigma_2 = \sigma_3$. That is because hydrostatic stresses do not induce plastic deformation. In the octahedral plane perpendicular to the hydrostatic axis, the yield surface is circular (Figure 2.9b).

When the stress (state) resides inside the yield surface, the material undergoes elastic deformation. Once the stress state reaches the yield surface, plastic deformation occurs. The stress state cannot move outside the yield surface. The yield surface stays constant for a material that does not work-harden. For a hardening material, on the other hand, the subsequent yield surface depends on the state of stress, the plastic strain and the plastic strain history. Three types of hardening rules are commonly used for metals. First, isotropic hardening meaning that the yield surface expands (or contracts) uniformly at a fixed centre point in

stress space. Second, kinematic hardening which assumes that the yield surface translates in stress space without rotation and with fixed size and shape. The kinematic hardening takes into account directional effect such as the Bauschinger effect during plastic deformation. The third type is mixed hardening which is a combination of isotropic and kinematic hardening [87].

The yield surface is circular in the octahedral plane because the von Mises yield criterion assumes isotropic materials. However, not all materials are isotropic and can be captured with other yield criteria. The individual grains in a polycrystalline metal are anisotropic. For a single crystal, the criterion of critical resolved shear stress is useful for determining yielding of a specific slip system. The tensor $\mathbf{m^s}$ encodes the slip plane normal and slip plane direction of all possible slip systems. The yield surface of each slip system is mapped by a pair of parallel planes determined by the equation

$$\mathbf{m^s}: \boldsymbol{\sigma} \leq \tau_{crss}, \tag{2.25}$$

such that the yield surface is formed by the inner envelope of the planes. The yield surface is a general polyhedron in five-dimensional stress space bounded by hyperplanes, hyperedges and hypercorners. Importantly, the straining direction is perpendicular to the yield surface [88]. If the stress state only activates one slip system, the straining direction is perpendicular to that plane. At corners, the straining can take any direction in between the limits of the coinciding planes.

With knowledge of the preferred orientation of grains in a polycrystal the polycrystal yield surface can be constructed. One method to extend the single crystal yield surface to polycrystals is to employ the Taylor uniform strain assumption [40] and the Bishop and Hill maximum work principle [89] for determining the set of active slip systems in each grain. From the above and assuming the same critical resolves shear stress on each slip system it is possible to calculate the Taylor factor [90] for each grain. By using the mean Taylor factor for several straining directions the yield surface is constructed [91]. The procedure is to locate, for a particular straining direction, the distance from the origin which is the mean Taylor factor and draw a tangent perpendicular to the radius. The inner envelope of the tangent lines for the considered straining directions is the yield surface. The yield surface for metals with strong preferred orientations typically contain sharp corners [88].

Classically the yield surface is closed by the inner envelope and stress states outside it cannot be reached. Beygelzimer *et al.* introduced the concept of thick yield surface [92, 93]. Figure 2.9c illustrates this yield surface, it represents a thick and foamed surface, which the stress states can penetrate. The concept was tested on inhomogenous polycrystals by simulations based on a cellular model with self-consistent field approach [92]. The microstructure is represented by interconnected elements that themself consist of sub-elements in multiple levels. The elements may represent single crystals that deform through slip. The slip systems of the sub-

elements of each higher-level element are mapped in stress space as if the elements were not connected. This forms the thick yield surface with a structure of many planes that are not closed by an inner envelope. However, as in the classical interpretation of yield surfaces, the stress must reside on the planes. The stress state of the highest element level splits into stress-state on the sub-element level which continue to split until the lowest-level element. This forms a cloud of internal stresses that may evolve during deformation as the planes move due to for instance, work-hardening of slip systems, grain rotation and fragmentation [93]. Interestingly, the thick yield surface of inhomogeneous materials has visual similarities with the X-ray diffraction data from harmonic structure material to be presented later.

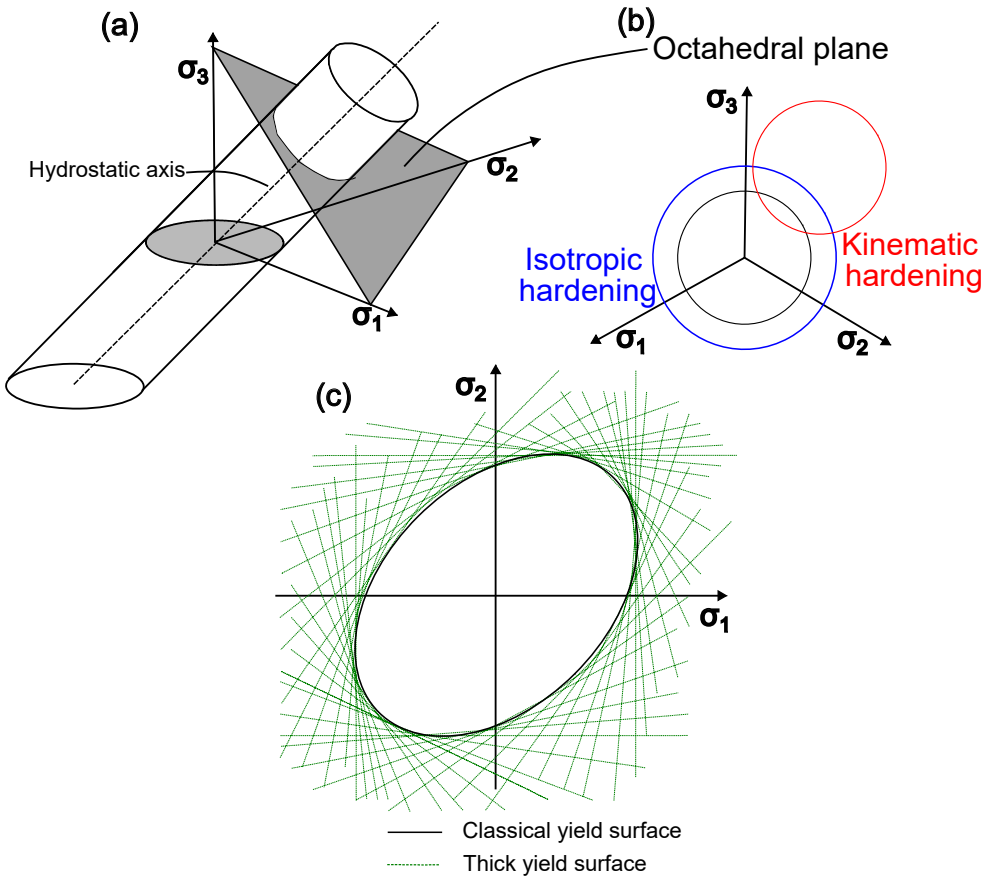

Figure 2.9 Representation of von Mises yield criterion in principal stess space (a), in octahedral plane (b) with subsequent yield surfaces, and classical and thick yield surfaces viewed in $\sigma_1,\ \sigma_2,\ \sigma_3 = 0$ plane (c).

3 Fabrication and characterization

This section aims to give a detailed description of the fabrication of harmonic structure nickel in the present study and its microstructure.

Samples of harmonic structure were fabricated using the steps summarized in Figure 3.1. The upper row displays conceptually important steps, and the lower row shows their technical realization in this thesis work. Nickel powder was provided from a supplier that had produces the powder through plasma rotating electrode processing (PREP). A schematic of the process is shown in the left section of Figure 3.1. A spinning consumable electrode of the metal is at one edge heated with a plasma torch to a molten liquid. Small droplets of the liquid are ejected and solidified into powder particles during the flight in an inert gas environment [94]. The particle size distribution from the supplier ranged from 106 to 212 μm with a mean diameter of 149 μm. The chemical composition of the powder is summarized in Table 1.The insets of scanning electron microscopy (SEM) [95] images show that the powder particles have a spherical shape with smooth surface and a homogenous microstructure in the cross-section. The microstructure is also shown schematically in another inset. The as-supplied powder is called initial powder (IP) throughout the thesis.

A fraction of the IP was mechanically milled in a planetary ball mill [96] to produce a deformed zone at the periphery of the powder particles. A schematic of the ball milling process is shown in the middle section of Figure 3.1. A mix of powder and steel balls were placed inside vessels. The vessels can rotate about their own axes and are installed in a rotating support disc. The vessels and the support disc rotate in opposite directions causing centrifugal forces to alternate between acting in the same and opposite directions. The net effect is that the steel balls and powder alternate between travelling along the wall and freely through the vessel to its opposite wall. Thus, the powder varies from being milled by friction and impact.

Table 1: Chemical composition of 99.36% pure nickel initial powder (wt%) from [97].

C	Si	Mn	S	Cu	Fe	Ni
0.03	0.05	0.15	0.01	0.01	0.39	99.36

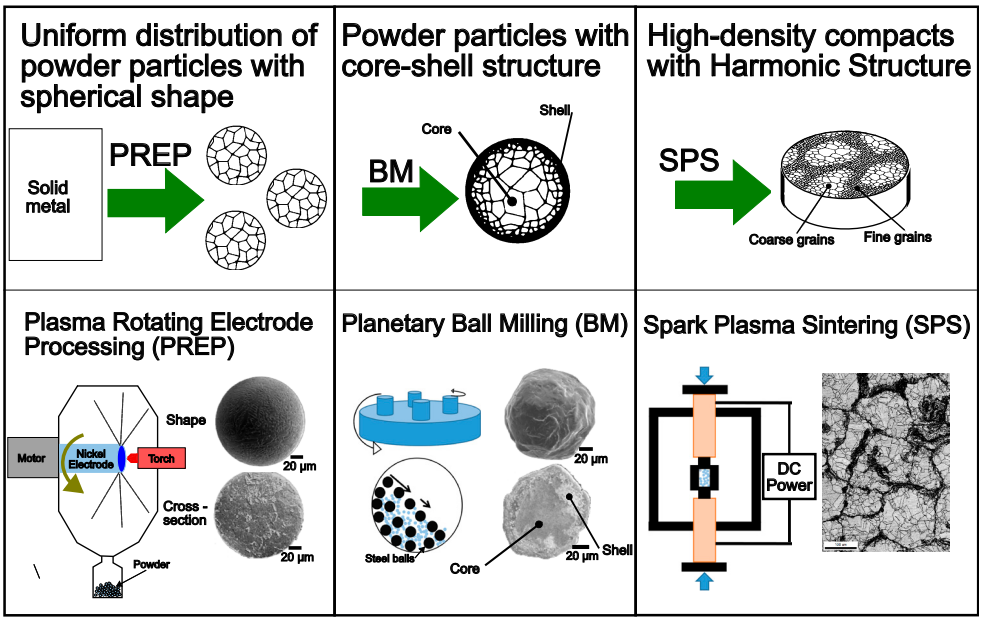

Figure 3.1 Fabrication process steps of harmonic structure materials. The left, middle and right columns show the powder fabrication, mechanical milling and consolidation steps, respectively. SEM micrographs adapted from [81] are displayed in the left and middle columns and show the external shape and cross-section of the powder particles prior to and after mechanical milling. The upper row illustrates the homogenous microstructure with coarse grains of an initial powder particle that develops a deformed shell of fine grains at the surface after mechanical milling while the grain size of the core is maintained. An EBSD micrograph and an illustration of the final compact are displayed in the right section.

Depending on processing batch, between 40 and 50 g of powder were milled with high carbon steel balls (SUJ2, 9 mm in diameter) in a 500 ml vessel made of tool steel (SKD11). The target ball to powder weight ratio was 1.8:1. Balls, powder and 1 ml heptane (used as processing control agent) were added to the vessel in an argon filled glove box to assure processing in an oxygen free environment. The processing control agent was used to avoid agglomeration and to minimize cold welding between balls and powder particles. Figure 3.2a shows powder and steel balls in the vessel after stirring to make the powder evenly wet from the processing control agent. Balls and vessel were reused from previous milling of nickel powder of similar quality and had thereby developed a nickel coating on the surface. The coating protects the nickel powder from contamination with foreign elements. The mechanical milling was carried out at room temperature for 100 h with a rotating speed of 150 rpm. After processing, the powder was sieved through two meshes with opening size 212 µm and 100 µm to separate out agglomerated and fine fractured particles. Only the fraction of particles between 100 µm and 212 µm was retained.

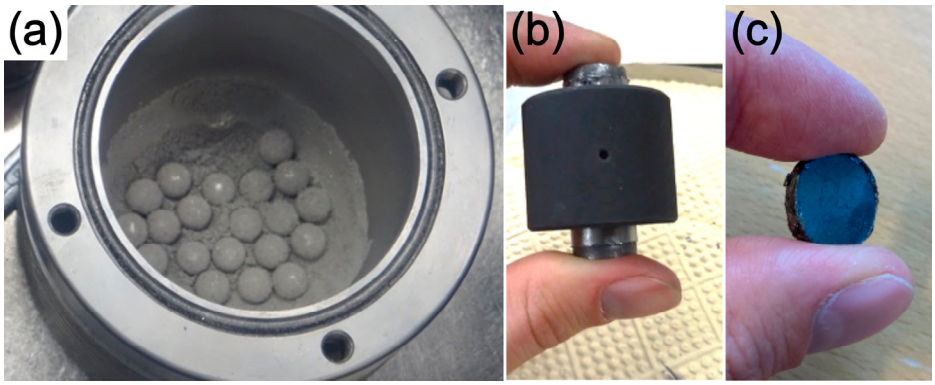

Figure 3.2 Powder and steel balls in a planetary ball mill vessel (a), die and punches used for SPS (b) and final compact coin after SPS (c).

The inset in the middles section of Figure 3.1 shows that the powder particles had developed a roughened surface due to the milling, but remained spherical. The cross-sectional image shows a deformed zone at the particle periphery which is anticipated to contain a high density of dislocations and/or fine grains. The centre appears less affected by the milling and is assumed to consist of coarse grains. The structure is referred to as a core-shell structure.

The mechanically milled powder was consolidated using spark plasma sintering (SPS). The main advantage of SPS is that it can achieve fully dense compacts and offers fast heating, which reduces the risk of significant grain growth in the deformed layer. A schematic of a typical SPS system is shown in the right section of Figure 3.1. The powder is placed in a cylindrical graphite die with punches on both sides of a channel inside it. The graphite die is then positioned in a vacuum chamber. The longitudinal cross-section is shown the schematic. The actual die and punches are shown in Figure 3.2b to get an impression of the dimensions. A compaction pressure is applied by a hydraulic system where the pistons act as electrodes supplying a pulsed high-intensity direct current that flow through the die and powder [98]. For an electrically conductive material such as nickel most of the heat is generated through Joule heating at the contact points of powder particles. Some temperature gradient might exist between the points of contact, but it has been reported that this is mostly an issue for large powder particles of material with low thermal conductivity [98].

During sintering, the temperature is controlled by a thermocouple positioned in a small hole drilled halfway through the lateral wall in the die body (visible in figure 3.2b). The target temperature and pressure as well as the measured temperature during the SPS are shown in Figure 3.3. As the temperature of the powder is not measured directly, there is a discrepancy between the measured and the actual temperature. It has been measured that the powder temperature can be about 50-250 °C higher than the measured value [99].

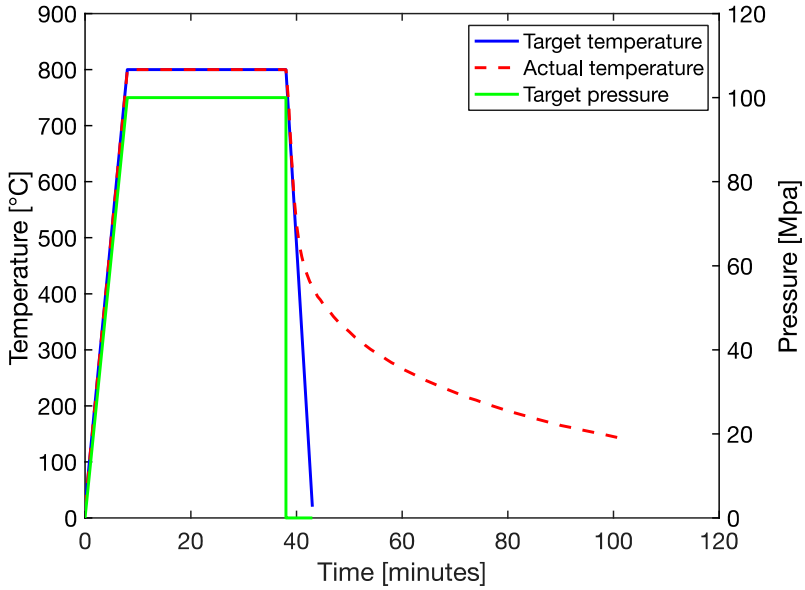

Figure 3.3 Settings of target temperature and pressure as well as measured temperature during SPS.

An example of the compacted coins with diameter of 15 mm and thickness of 2.5 mm is shown in Figure 3.2c. A schematic of the microstructure is shown in the upper-right section of Figure 3.1, and a light-optical micrograph is shown in Figure 3.4a. The inset in the lower-right section of Figure 3.1 displays an electron backscatter diffraction (EBSD) [100, 101] map showing image quality with high angle grain boundaries as black lines. A crude step size of 0.5 µm was used during EBSD scanning, which resolves the coarse grains but not the fine grains, and therefore they appear as black regions. The image clearly shows that the microstructure consists of a continuous fine-grained network (inherited from the shells of the processed powder particles) that surrounds regions of coarse grains (originating from the cores of the processed powder particles). The inset in the lower-right section of Figure 3.1 is enlarged in Figure 3.4b. The area in the red box was analysed further with a fine EBSD scanning step size of 0.1 µm to resolve the fine grains, as shown in Figure 3.4c.

The grain size distribution of Figure 3.4b is shown in Figure 3.5. The figure clearly displays a bimodal grain size distribution where a reasonable threshold between coarse and fine grains appears to be at 5 µm. When applying this threshold to the statistical analysis of grain size fractions, 24 % of the area constitutes of fine grains, and the area-weighted average grain size of grains larger than the threshold are 22.8 µm. The area-weighted average grain size of the fine grains is 1.2 µm estimated from the grain size distribution of Figure 3.4c when grains larger than the threshold are excluded. However, Figure 3.4d shows that some grains are submicron.

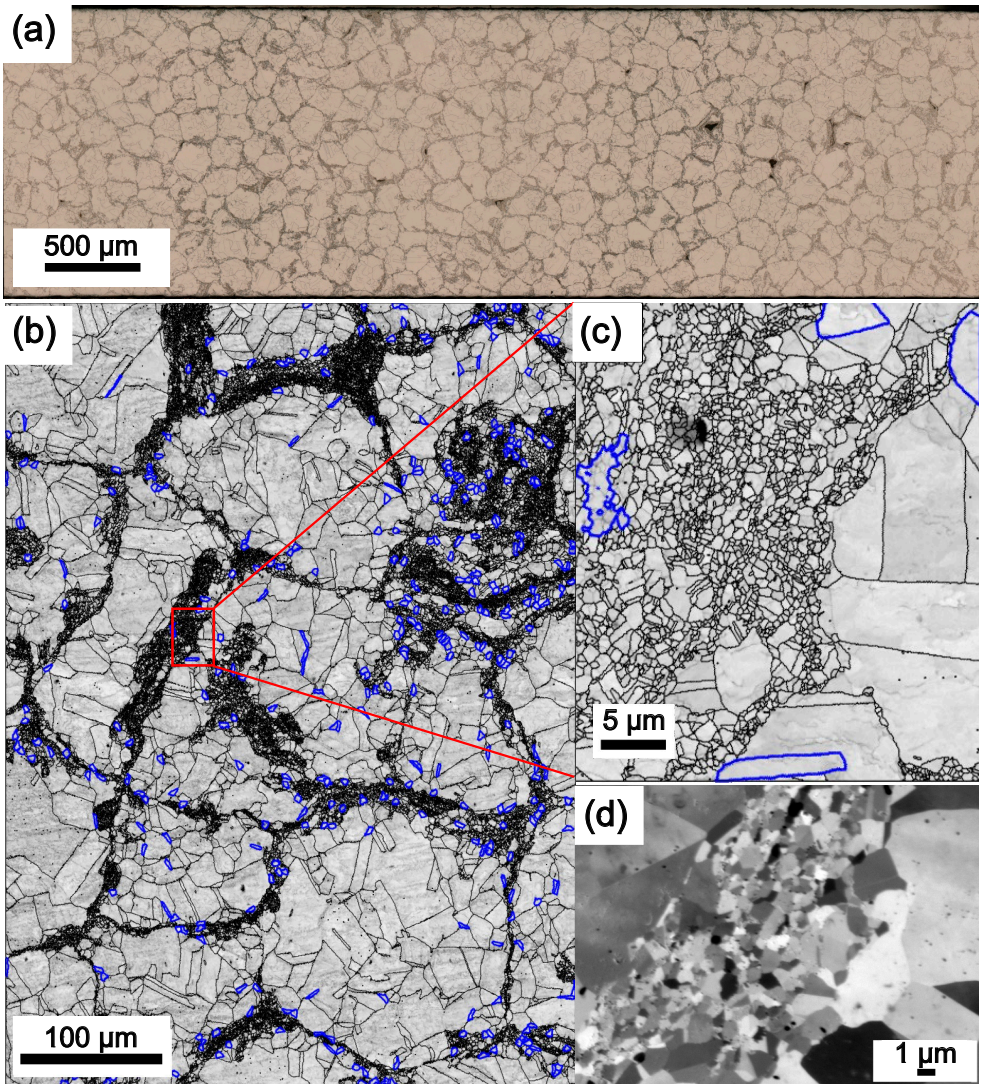

Figure 3.4 Microstructure of HS nickel. The light optical-micrograph in (a) shows a rather regular, almost periodic pattern in the spatial distribution of grain size. EBSD image quality maps overlaid with high angle boundaries (≥15◦ misorientation) in (b) and (c) display the structure of coarse grains in the core and the fine grains from the shell areas forming a continuous network. Grains with equivalent circular diamerer between 4 µm and 5 are highlighted in blue in (b) and (c). Ion channeling contrast imaging [102] micrograph in (d) illustrates that some grains in the shell are ≤1 µm in size.

Compacts samples with homogenous coarse grains were also produced from the initial powder. The SPS settings were the same as for the harmonic structure except from a slightly higher sintering temperature of 850 °C. Figure 3.6 shows an example of the microstructure of such samples. From its grain size distribution, the area-weighted average grain size is 49 µm.

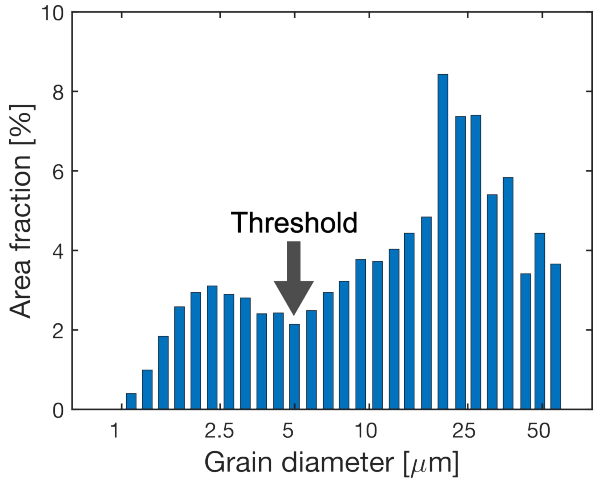

Figure 3.5 Grain size distribution of the HS nickel compact in Figure 3.4b.

Dog-bone shaped tensile specimens were cut from the compacts with harmonic structure and homogenous coarse grains with electric discharge machining. The specimens were used in the *in situ* X-ray diffraction experiments in ***Paper I***, ***II*** and ***III***. For the studies with digital image correlation (***Paper IV and V***), similar samples produced by other researchers were used. Identical nominal fabrication settings were used, and close to identical microstructure is expected. In addition, samples with bimodal random structure were used. The goal of fabricating such samples was to obtain a structure with the same fractions and average grain size the harmonic structure, but with different arrangement of the fine- and coarse-grained regions. This was achieved by mixing IP and powder that had been ball milled for 150 h prior to SPS [81].

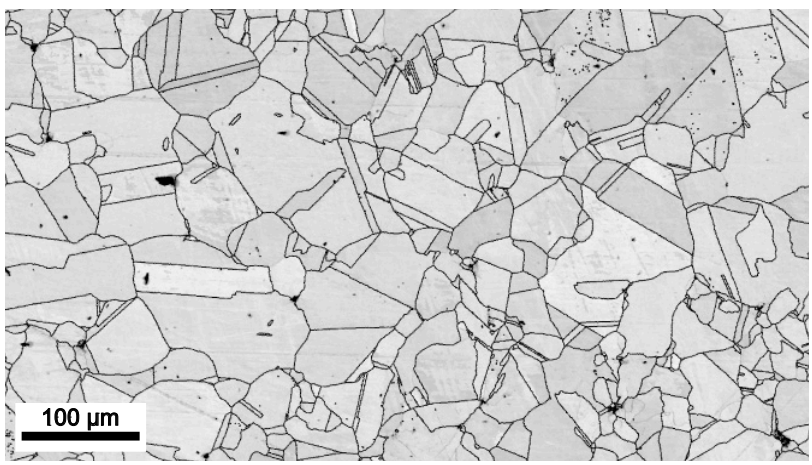

Figure 3.6 Microstructure of homogenous coarse-grained nickel. EBSD image quality map overlaid with high angle boundaries.

4 Experimental techniques

This section presents the analytical experimental procedures used in this work. These include digital image correlation and advanced X-ray diffraction techniques. Digital image correlation is briefly described while the X-ray diffraction techniques call for detailed descriptions.

4.1 Selection of experimental techniques

The overall aim of the studies is to understand the origin of the improved combination of strength and ductility in harmonic structure materials compared to expectations from the rule of mixtures. The interplay between the deformation of grain fractions might provide the synergetic strengthening. We have identified that knowledge about the distribution of stress and strain in fine and coarse grain fractions is the key factor for understanding the synergy. The evolution of dislocation densities and dislocation networks during plastic deformation are also of importance, as these parameters are closely related to work-hardening and thus the evolution of stress.

The high work-hardening rate of heterogenous materials have been attributed to the development of back stresses (see section 2.3). Loading-unloading-reloading (LUR) tests have been a popular method for evaluating the evolution of back stress in heterogenous materials. The back stress is calculated as the stress between the yield stress in the compressive and tensile direction of the LUR hysteresis loop [103]. The measured back stress is essentially the Bauschinger effect, and recent studies show that the effect becomes more pronounced with decreasing grain size [104, 105]. Comparison of the evolution of back stress between heterogenous microstructures and homogenous microstructures with coarse grains typically show a higher back stress development in the heterogenous structures [15]. Since the LUR test measures the evolution of average back stress it is not clear if the increased back stress originates from the interaction of grain fractions or from the fine-grained fraction alone.

We have selected advanced *in situ* characterisation techniques based on high energy X-ray diffraction to monitor the evolution of local stresses among grains of different

sizes within the bulk during tensile testing. This allows more direct measurement of stress partitioning and back stress between grain size fractions.

Conventional X-ray powder diffraction along with advanced data analysis was employed in ***Paper II*** to measure the evolution of microstructure and average stress in fine and coarse grains in a representative volume element. In ***Paper III***, the evolution of individual grains was monitored with an advanced x-ray diffraction technique called high resolution reciprocal space mapping. Stress and dislocation densities are interpretable from both techniques while high resolution reciprocal space mapping also provides information about the dislocation network.

For the evaluation of strain distribution (***Paper IV and V***), digital image correlation (DIC) was used in its standard procedure. Local strains were calculated based on relative displacements of microstructure features on the sample surfaces. Despite the known weakness of DIC related to data collection only from specimen surfaces, it was still the best technique for monitoring local strain evolution during plastic deformation in tension.

4.2 X-ray diffraction

X-rays of high energy are needed to monitor grains within the bulk of nickel as low-energy X-rays do not penetrate through a millimetre-thick specimen. High-energy X-rays can be produced in a synchrotron facility, where a linear accelerator accelerates electrons to relativistic speeds and injects them into a storage ring that maintains their speed. Strong magnets keep the electrons in a circular trajectory. Synchrotron radiation is emitted as the electrons change direction and accelerate in the magnetic field. The storage ring also contains straight sections with insertion devices. The insertion devices consist of an array of magnets that produces an alternating magnetic field that force the passing electrons to oscillate. This produces a coherent beam with a narrow energy range. The produced X-ray energy is tuneable depending on the energy of the electrons in the storage ring, choice of insertion device and its specific parameters [106].

The X-ray beam propagates tangentially with respect to the ring along an optical path inside a beamline. The beamline is equipped with different optical elements, sample environments and detectors depending on its specialty. The X-ray diffraction experiments in the thesis work were carried out at synchrotron facility PETRA III beamline P21 (***Paper I*** and ***Paper II***) and P07 (***Paper III***). These beamlines use monochromators for further narrowing down the energy range of the beam and other optical elements for focusing [107, 108].

4.2.1 X-ray diffraction from crystals

X-rays interact with materials in several processes out of which elastic scattering for crystals is relevant for this thesis work. When an X-ray wave propagates through a crystal, electrons in the material are set in oscillation due to the propagating wave's electromagnetic field. The oscillation causes the electrons to emit radiation in the form of spherical waves. The spherical waves can be approximated as plane waves far away from the scattering event. A monochromatic X-ray wave is described by its wave vector $\mathbf{k}$ with length $|\mathbf{k}| = 2\pi/\lambda$ and the direction of propagation. The wavelength, λ, and the beam energy, E, are related by $\lambda = hc$ where h is the Plank's constant and c the speed of light in vacuum.

The wave vectors $\mathbf{k_{in}}$ and $\mathbf{k_{out}}$ describe the incoming and outgoing waves. When the scattering is elastic, the energy of the scattered wave is preserved, so $|\mathbf{k_{in}}| = |\mathbf{k_{out}}|$. The change in direction of the incoming and outgoing waves is described by the scattering vector $\mathbf{q} = \mathbf{k_{out}} - \mathbf{k_{in}}$. The length of scattering vector and the scattering angle (the difference in angle between the wave vectors) are related by

$$\mathrm{q} = |\mathbf{q}| = \frac{4\pi}{\lambda} sin\,\theta. \tag{4.1}$$

The relationship between the wave vectors, the scattering angle, and the scattering vector is illustrated in Figure 4.1a.

Figure 4.1a depicts scattering from two atoms that are part of a row of atoms with distance R between each atom. The scattering waves from all electrons in the individual atoms add up to a single wave with an amplitude described by the atomic scattering factor, $f(\mathbf{q})$ which depends on the number of electrons, their distribution in the atom and the scattering angle [109]. At certain scattering angles, the scattering from atoms gives rise to constructive interference, the so-called diffraction.

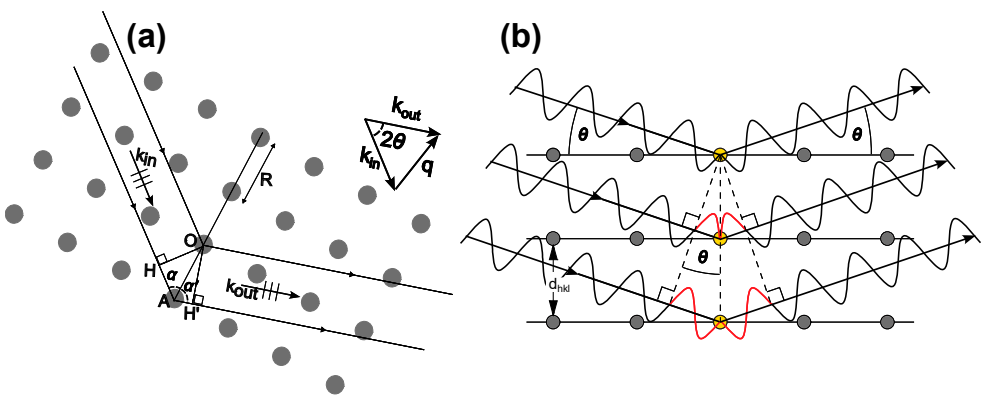

Figure 4.1 Illustration of Laue condition (a). Elastic scattering of monochromatic X-ray beam from two atoms. The inset displays the relationship between the wave vectors, scattering angle, and scattering vector. Visualization of Bragg's law (b) for lattice plane {hkl} with lattice spacing d_{hkl}.

The condition for diffraction is that the phase difference ($\Delta\phi$) between the waves scattered at different atom gives rise to a path difference (PD) that is a multiple of the wavelength. In Figure 4.1a, the path difference between the atom placed at point O and A is

$$PD = \mathrm{HA} + \mathrm{AH}' = \mathrm{R}cos(\alpha) + \mathrm{R}cos(\alpha') \tag{4.2}$$

and the phase difference is

$$\Delta\phi = -\mathbf{R}\cdot\mathbf{k_{in}} + \mathbf{R}\cdot\mathbf{k_{out}} = \mathbf{R}\cdot\mathbf{q}. \tag{4.3}$$

Thus, if the path difference equals $n\lambda$ or the phase difference equals $2\pi n$, where n is an integer number, the condition for diffraction is fulfilled.

Similarly, the condition for diffraction can be understood by viewing the atomic planes as reflecting mirrors, as illustrated in Figure 4.1b. The planes are illuminated at an angle θ. When the path difference between neighbouring atomic planes (d_{hkl}) is $PD = n\lambda = 2d_{hkl}sin(\theta)$ the condition is fulfilled. This relationship known as Bragg's law describes at which angles diffraction occurs but other details of the diffraction pattern such as varying intensity require further explanation.

To describe the scattering intensity from a whole crystal, the scattering from all atoms in the crystal needs to be considered. As shown in section 2.1, the smallest repeating unit in a crystal is the unit cell. The vector $\mathbf{R_n} = n_1\mathbf{a_1} + n_2\mathbf{a_2} + n_3\mathbf{a_3}$, where n_i are integers, gives the position of each unit cell in the crystal, the lattice points. Each lattice point is populated by the same arrangement of atoms, where the position of each atom is specified by the vector $\mathbf{r_j} = x\mathbf{a_1} + y\mathbf{a_2} + z\mathbf{a_3}$, where x, y, z are real fractional numbers. Thus, the position of any atom in the crystal is given by

$$\mathbf{R_n} = n_1\mathbf{a_1} + n_2\mathbf{a_2} + n_3\mathbf{a_3} + \mathbf{r_j} \tag{4.4}$$

for some **n**, **j**.

In the same manner, the total amplitude from a crystal can be split into a sum over all atoms in the unit cell and a sum over all the lattice points. The scattering amplitude from the unit cell is called the structure factor, $F(\mathbf{q})$, which is the sum of the atomic structure factor, with an added phase factor for each atom. The sum over all the lattice points is called the form factor, $L(\mathbf{q})$, which is the sum of amplitudes from each unit cell in the crystal

$$\mathrm{A}(\boldsymbol{q}) = \sum_{\boldsymbol{n,j}} f_j(\boldsymbol{q})e^{i\boldsymbol{q}\cdot\boldsymbol{R_{n,j}}} = \sum_{\boldsymbol{j}} f_j(\boldsymbol{q})e^{i\boldsymbol{q}\cdot\boldsymbol{r_j}} \sum_{\boldsymbol{n}} e^{i\boldsymbol{q}\cdot\boldsymbol{R_n}} = F(\boldsymbol{q})L(\boldsymbol{q}). \tag{4.5}$$

Noteworthy, X-ray detectors do not record the amplitude of the scattered beam, but only the intensity, $I(\boldsymbol{q}) \propto AA^* \propto |A(\boldsymbol{q})|^2$,which means that the phase information is lost.

The diffracted intensity can be decomposed into the product of the structure factor and the form factor

$$I(\boldsymbol{q}) = |F(\boldsymbol{q})|^2 |L(\boldsymbol{q})|^2. \tag{4.6}$$

Expansion of the form factor [110] gives

$$|L(\boldsymbol{q})|^2 = \frac{\sin^2 \pi \mathbf{q}\mathbf{a_1} \mathrm{N}_1}{\sin^2 \pi \mathbf{q}\mathbf{a_1}} \frac{\sin^2 \pi \mathbf{q}\mathbf{a_2} \mathrm{N}_2}{\sin^2 \pi \mathbf{q}\mathbf{a_2}} \frac{\sin^2 \pi \mathbf{q}\mathbf{a_3} \mathrm{N}_3}{\sin^2 \pi \mathbf{q}\mathbf{a_3}}, \tag{4.7}$$

where N_1, N_2, N_3 are the number of unit cells in each dimension of the crystal. The function reaches a sharp maximum when all $\mathbf{qa_1}$, $\mathbf{qa_2}$, $\mathbf{qa_3}$ are integers and is essentially zero everywhere else except at the vicinity of the integer values.

The above describes the direct lattice. For facilitating the analysis of X-ray diffraction, the concept of reciprocal lattice is useful as it is easier to visualize exactly what planes will be in a diffracting condition. The reciprocal lattice is constructed by the lattice vectors $\mathbf{a_1}$, $\mathbf{a_2}$, $\mathbf{a_3}$ of the direct lattice and the basis reciprocal vectors $\mathbf{a_1^*}$, $\mathbf{a_2^*}$ and $\mathbf{a_3^*}$ which are defined as

$$\mathbf{a_1^*} = \frac{2\pi\, \mathbf{a_2} \times \mathbf{a_3}}{\mathbf{a_1} \cdot (\mathbf{a_2} \times \mathbf{a_3})}, \mathbf{a_2^*} = \frac{2\pi\, \mathbf{a_1} \times \mathbf{a_3}}{\mathbf{a_1} \cdot (\mathbf{a_2} \times \mathbf{a_3})}, \mathbf{a_3^*} = \frac{2\pi\, \mathbf{a_1} \times \mathbf{a_2}}{\mathbf{a_1} \cdot (\mathbf{a_2} \times \mathbf{a_3})}. \tag{4.8}$$

The two sets of basis vectors have the property that $\mathbf{a_i} \cdot \mathbf{a_j^*} = \mathbf{2}\pi\delta_{ij}$ where δ_{ij} is the Kronecker delta symbol. The reciprocal lattice is defined by the vector

$$\mathbf{G_{hkl}} = h\mathbf{a_1^*} + k\mathbf{a_2^*} + l\mathbf{a_3^*}, \tag{4.9}$$

where (h,k,l) correspond to the already introduced Miller indices. The reciprocal lattice points represent the planes of the direct lattice. $\mathbf{G_{hkl}}$ is perpendicular to the lattice plane with Miller indices hkl and $|\mathbf{G_{hkl}}| = \frac{2\pi}{d_{hkl}}$. The scattering vector can be. decomposed into

$$\mathbf{q} = q_1\mathbf{a_1^*} + q_2\mathbf{a_2^*} + q_3\mathbf{a_3^*}, \tag{4.10}$$

where q_1, q_2, and q_3 are real dimensionless numbers.

Whenever the scattering vector equals a reciprocal lattice vector, $\mathrm{q} = \mathrm{G}$, the term $\mathbf{q} \cdot \mathbf{R_n} = 2\pi(hn_1 + kn_2 + ln_3)$, becomes an integer times 2π.

This gives rise to a sharp maximum of the from factor meaning that the condition for diffraction is fulfilled. The maxima are commonly referred to as Bragg peaks or reflections. Further evaluation of the form factor shows that the reflection is sharper and of higher integrated intensity with larger dimensions of the crystal. For a perfect crystal, the reciprocal space is populated by dimensionless reciprocal lattice points (reflections).

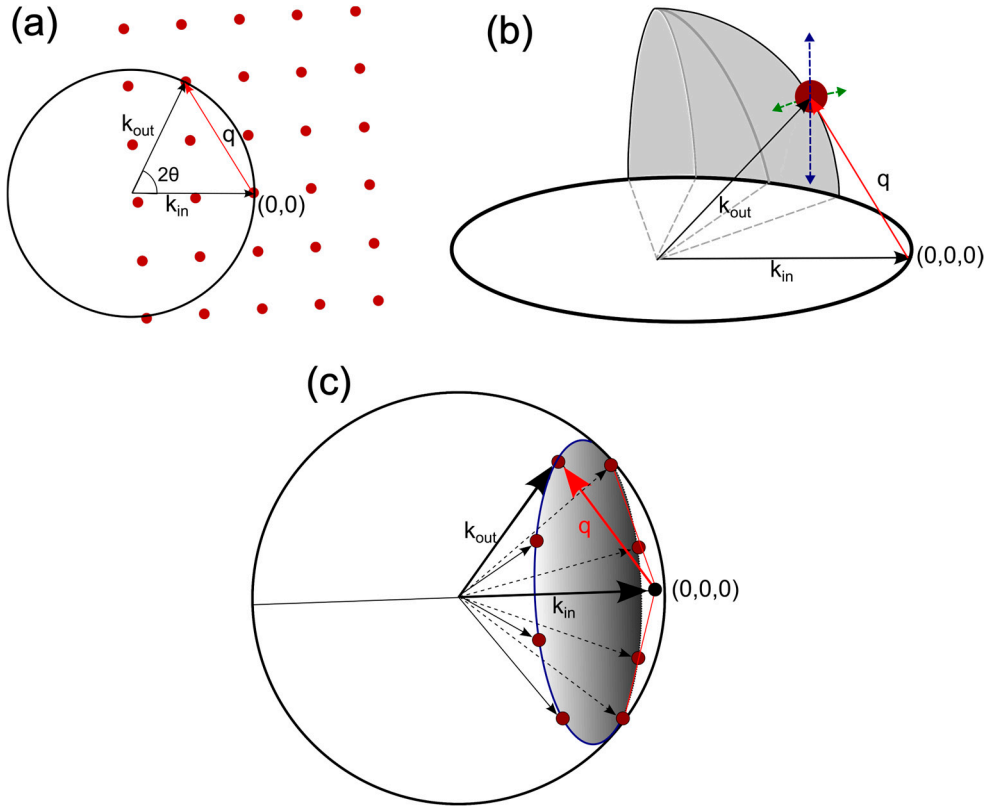

Figure 4.2 Illustration of the Ewald sphere in in two (a) and three (b) dimensions of a single crystal specimen. The visible reflections are highlighted by the red arrows. The red arrow in (b) shows the direction of the possible radial shift and broadening while the green and blue arrows show the directions for azimuthal changes. A polycrystalline specimen has many reciprocal lattice points of (hkl) that touch the Ewald sphere surface in various directions to form a diffraction ring (c).

The Ewald sphere construction is used to visualize at which angles 2θ from the direction of incident beam, reflections are visible. The principle is shown in Figure 4.2a. In reciprocal space, the Ewald sphere has a radius $1/\lambda$, and a reciprocal lattice point at the end of $\mathbf{k_{in}}$, which touches the sphere, is chosen as origin. If a reciprocal lattice point falls on the sphere, the condition for diffraction is fulfilled, and intensity is possible to detect at angle 2θ. By rotating the crystal, which is equivalent to rotate the sphere about the origin, another reciprocal lattice point can fall on the sphere.

The reciprocal lattice point is tightly linked to the atom positions in the crystal (grain). If a grain is hydrostatically strained, the reciprocal lattice point moves radially from the origin causing a radial shift of the scattering angle 2θ. A uniform rotation of the grain rotates the reciprocal lattice point and induces an azimuthal shift. The azimuthal directions are indicated in green and blue in Figure 4.2b. The previous description of reciprocal space was for a perfect grain of infinite size. A

real grain has a finite size, and especially a deformed grain contains dislocations and differently oriented regions such as cells. All of which causes broadening of the reciprocal lattice point.

As seen in equation (4.7), the form factor function is non-zero outside the maxima, if the size of the crystal is small. The condition for diffraction is relaxed such that the reflection is broadened in the radial direction. It has been reported that broadening often becomes pronounced when the single oriented regions are ≤ 1 μm [111], though it actually depend on the resolution of the specific experiment. Dislocations cause the atoms to be displaced relative to their ideal position, which also results in a broadening in the radial directions, while differently oriented regions produce an azimuthal broadening. In this work, the evolution of reciprocal lattice points from single grains with increasing deformation was investigated through high resolution reciprocal space mapping in ***Paper III*.**

So far, diffraction from one single crystal has been discussed. However, metals are typically polycrystalline containing many crystals commonly called grains. The given description of reciprocal lattice points is correct for any grain in a polycrystal. When an incoming beam illuminates a sample volume containing a large number of randomly oriented grains, reciprocal space is populated with reciprocal lattice points $\mathbf{G_{hkl}}$ for a specific {hkl}in all orientations. All of these reciprocal lattice points fall on the surface of the Ewald sphere, in a circle perpendicular to the incoming beam, as illustrated in Figure 4.2c. This produces a diffraction cone, giving rise to Debye-Scherrer rings for every {hkl} on an area detector, forming a powder diffraction pattern. In this work, powder diffraction experiments were conducted in ***Paper I*** and ***Paper II***.

4.2.2 Experimental set-up for *in situ* X-ray diffraction experiments

Figure 4.3 shows schematically the experimental set-up for collecting high resolution reciprocal space maps and powder diffraction data. The experiments can be done in an alternating sequence by shifting the near-field detector, but were in practice carried out at two different occasions in the thesis work.

Dog-bone shaped, flat tensile specimens with 5 mm gauge length, 1.5 mm width and 0.7-0.8 mm thickness were mounted in a custom-made screw-driven load frame equipped with a 1 kN load cell. The load frame was placed on top of a diffractometer stage with the tensile axis aligned horizontally. The diffractometer stage allowed for translations in x, y and z as well as ω-rotation around the vertical z-axis. The specimen was illuminated by a monochromatic high-energy X-ray beam. The centre of the illumination spot in the specimen was ensured to coincide with the ω-rotation centre of the diffractometer. In the powder diffraction experiment, a position-sensitive area detector was placed approximately 1.5 m downstream of the specimen to cover parts of the first six Debye-Scherrer rings. The position of a pixel on the

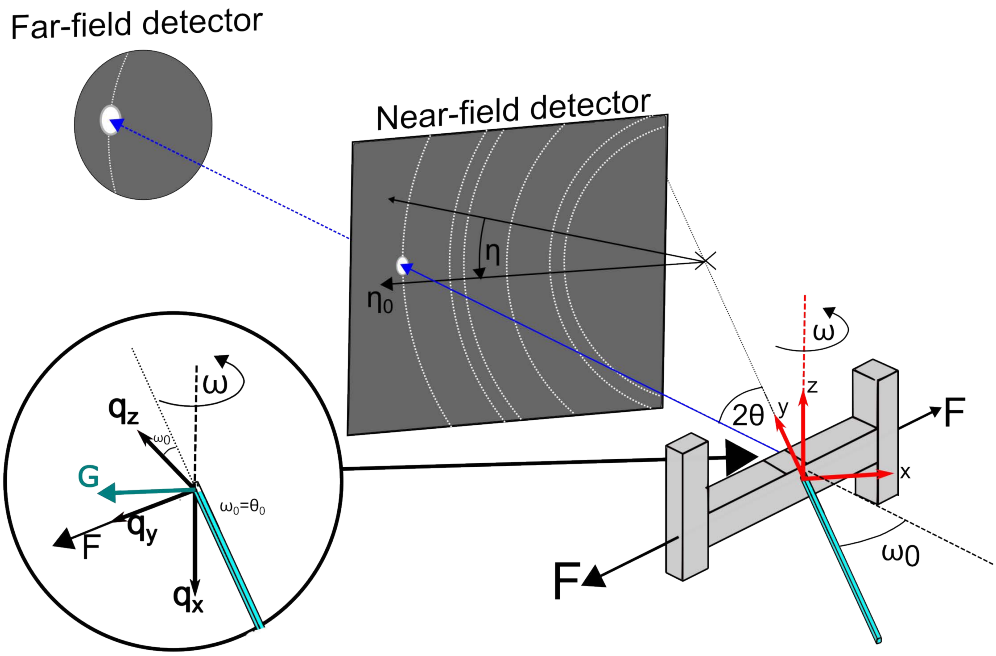

Figure 4.3 Schematic of experimental set-up. Only the near-filed and far-field detectors were used for powder diffraction and high resolution reciprocal space mapping experiments, respectively. The diffraction angle θ and the azimuthal angles η and ω are defined together with real and reciprocal space coordinates.

detector is described by the radial angle 2θ and the azimuthal angle η. An angle $\eta = 0°$ corresponds to the diffracting lattice planes being parallel with the tensile axis in the horizontal plane. The Debye-Scherrer rings constitute of sharp reflections from the coarse grains overlapping reflections from fine-grains, as elaborated later. The larger the distance from the specimen, the greater the spacing between reflections on the rings. In the high resolution reciprocal space mapping experiment, an area detector was placed 3.9 m downstream of the specimen at a horizontal position corresponding to the 400 reflections from grains having their <100>-directions close to the tensile axis.

4.2.3 High resolution reciprocal space mapping

4.2.3.1 Experimental conditions

High resolution reciprocal space mapping was carried out at beamline P07 at PETRA III with a beam of 52.7 keV that was focused to 36 µm in vertical (z) direction and narrowed by slits to 50 µm in the horizontal (x) direction. The load frame was rotated such that ω_0 equals half the scattering angle for 400 reflections,

so that reflections parallel to the tensile axis are detectable. Grains suitable for investigation were located by rotating in ω slightly off ω_0 and moving the sample in x and z. Prior to data acquisition, it was ensured that the grains were centred in and fully illuminated by the beam. During data acquisition, the specimen was rotated in small Δω intervals of 0.01° and the intensity recorded with a MarCCD 165 area detector with pixel size 79 μm. Each two-dimensional image corresponds to a slice in ω of the reflection. By stacking adjacent ω-slices, the full reflection was mapped in reciprocal space in three dimensions.

The integrated intensity of a reflection is proportional to the size of an illuminated grain. By establishing a relation between a crystal volume and intensity, it is possible to estimate the size of grains. During the centring procedure in our experiments, the beam was narrowed in the x-direction by the slits, and the grain scanned along the x-direction. The slits were then opened in the x-direction and narrowed in the z-direction, and the same scanning procedure was repeated for the z-direction. This allowed the dimensions in x and z to be measured while the dimension in y was assumed to be in between x and z. In this manner, it was possible to relate a grain volume with the integrated intensity of the reflection. For grains larger than the slit opening in x and z, the grain volumes were estimated by the scanning procedure, while grains smaller than the slit openings were estimated using the volume-intensity relation. The macroscopic strain was measured with a strain-gauge glued onto the specimen.

4.2.3.2 Data analysis

The example of iso-surface plot of a reciprocal space map from a large grain in the HS specimen at 10 MPa applied load is shown in Figure 4.4. The three-dimensional data constitutes of voxels associated with angular coordinates 2θ, η, ω that are converted to reciprocal space coordinates q, q_x, q_z using the definition in [112]. q is the length of the scattering vector according to Equation (4.1), which is essentially q_y in the current set-up, while q_x and q_z are related to the azimuthal angles η and ω. The data is analyzed with two complementary projections, the azimuthal projection and the radial projection. The azimuthal projection integrates the intensity along q onto the azimuthal $(q_x - q_z)$ plane to form an azimuthal map, as shown in Figure 4.4. High intensity peaks superimposed on a slowly varying cloud of low intensity are visible. The different high intensity peaks in the azimuthal map represent local orientation differences within the grain. Each individual peak represents the local maximum in reciprocal space of dislocation-free subgrains [113-115]. The integrated intensity of such a peak scales with subgrain size [113]. Together, all the high intensity peaks form the subgrain component. The spread-out cloud of low intensity is caused by regions of high dislocation density such as dislocation walls [114], and forms the cloud component. Using the algorithm described in [116], it is possible to isolate the subgrain and cloud components.

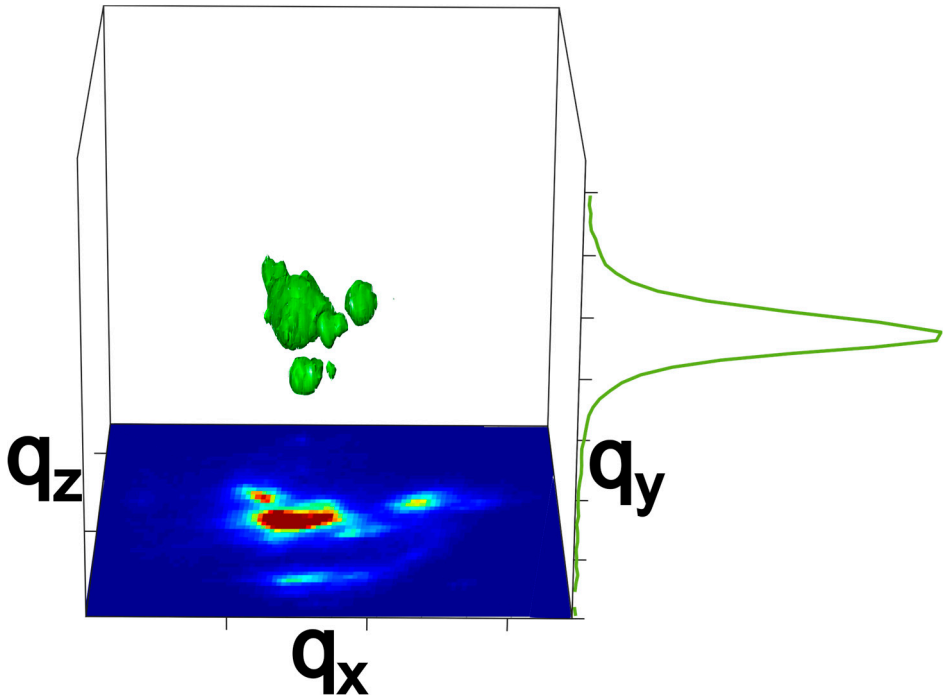

Figure 4.4 Iso-surface plot showing the intensity distribution of a reflection in three dimensions in reciprocal space from a large grain at 10 MPa applied stress. The projection of intensity onto the $\boldsymbol{q}_y$-axis is the one-dimensional radial profile. The projection of intensity along $\boldsymbol{q}_y$ forms the two-dimensional azimuthal map.

The radial projection integrates the intensity along q_z and q_x onto the scattering vector q to form a one-dimensional radial profile that can either originate from a full reflection, the cloud or subgrain component. The radial profile of a full reflection tells the distribution of distances between lattice planes within the grain. The profile is characterized by the mean position, width and asymmetry. The average peak position (q_{mean}) is in this thesis defined as the mean q-value of the profile weighted by the intensity values of a peak, where the peak is defined as the range of intensities above $1/50$ of the maximum. The q_{mean} is related to the average elastic strain (ϵ_{el}). The ϵ_{el} corresponds to a change in the average lattice plane spacing from a reference value d_{hkl0} to d_{hkl}, and can be expressed as

$$\epsilon_{el} = \frac{d_{hkl} - d_{hkl0}}{d_{hkl0}} = \frac{q_0 - q}{q}. \tag{4.11}$$

The width is characterized either by the full width at half the maximum intensity or the integral width, which is defined as the total area under the peak divided by the maximum intensity. The width is the convolution of effects from size, displacement of atoms due to defects, and instrumental conditions.

The peak position and width are determined from the original profile while the asymmetry is calculated from fitting. The profile is fitted with a split pseudo-Voigt function. A pseudo-Voigt function is a linear combination of a Lorentzian and a Gaussian function. It has been proposed that size broadening contributes with the Lorentzian function while the displacements of atoms contributes with the Gaussian function [117]. A split pseudo-Voigt function is a combination of two half-sided pseudo-Voigt profiles determined from the widths of the left- and the right-hand sides of the position with maximum intensity. This allows the two widths to be different and thus to describe an asymmetric profile. The asymmetry is in this thesis characterized by absolute asymmetry κ_{abs}^{g}, which is defined as the difference between left- and right-hand sided widths. The asymmetry arises from the difference in elastic strains of the dislocation walls and subgrains, following the composite model [118, 119].

4.2.4 Powder diffraction and separation algorithm

4.2.4.1 Experimental conditions

The powder diffraction experiment was performed at beamline P21.2 at PETRA III using a beam energy of 52 keV and a beam cross-section of 100 × 100 μm^2. The diffracting intensity was recorded with a VAREX XRD4343CT detector with pixel size 150 × 150 μm^2.

Since the aim of the experiment was to monitor the mechanical behaviour of the fractions of coarse and fine grains separately, their reflections need separation. As noted earlier, the width in radial direction increases with decreasing size. However, separation by such an approach is not feasible in the case of HS nickel because broadening is not clear for crystals larger than 1 μm. Instead, it is possible to identify if a reflection originates from a coarse or a fine grain by the reflection's integrated intensity since it correlates with grain size. The high resolution reciprocal space mapping (Figure 4.4) clearly shows that the reflections have a certain extension in angular space. In order to calculate the integrated intensities of reflections, it is necessary to capture full reflections with sufficiently high resolution to determine when one reflection ends and another one starts. Therefore, the area detector was placed 1.5 m behind the specimen to obtain sufficient resolution in η. Adequate resolution in ω was reached by rotating the specimen in intervals of $\Delta\omega = 0.02°$ as the intensity was recorded. A total angular range of 1° in ω was captured. Figure 4.5 shows a typical section of the first Debye-Scherrer ring for one specific Δω interval of an arc of about 30° in η. In the ω-interval, high intensity reflections appear as spots and overlay a continuous ring of low intensity. The high intensity reflections are assumed to originate from coarse grains, while the continuous ring is composed of reflections from fine grains, which are either overlapping or too small to be individually resolved. The intention of the experiment was to monitor the

average behaviour of the fractions of coarse and fine grains. The minimum limit of the beam cross-section is the size of the largest grain. However, a larger beam cross-section is desirable to guarantee the monitoring of a representative volume element in the material. A beam cross-section of 100 × 100 μm^2 was finally selected. Larger beam cross-section would have likely resulted in the Debye-Scherrer ring to be populated with overlapping high intensity reflections. This would have inhibited access to the reflections from fine grains, and thus the goal of the experiment would not have achieved.

Before commencing tensile loading, the specimen was translated such that the position of a reference grain had its 400 reflection parallel to the tensile axis and coincided with the rotation centre of the diffractometer stage. The tensile loading was conducted stepwise. After each load step, the reference grain was re-cantered which ensured the illumination of approximately the same specimen volume throughout the experiment.

4.2.4.2 Separation algorithm

An algorithm was developed to separate the diffraction signal originating from coarse and fine grains in the range of $\pm$ 15° from η_0. The full details of this algorithm are described in ***Paper I***. Here follows a brief summary of the algorithm, as well as some perspectives not outlined in the paper. The algorithm identifies the average intensity of the continuous ring in a small angular range of $[2\theta, \eta, \omega]$ for each Deby-Scherrer ring. The average intensity is found by detecting the range in $[2\theta, \eta]$ of each high intensity reflection, and then integrating the intensity of that angular range $[2\theta, \eta]$ over the full 1° range in ω. The reflections are then ranked by their integrated intensities, and their angular ranges are saved in a list. The reflections with lowest integrated intensities are assumed to mostly consist of continuous ring segments. The integrated intensity of their angular ranges $[2\theta, \eta]$ in intervals $\Delta\omega$ along the full range in ω is calculated and normalized by the angular range. The average normalized intensity of the $\Delta\omega$ intervals is taken as the threshold intensity of the continuous ring.

The algorithm then separates the high intensity reflections and the continuous ring by re-iterating through the list of reflections. It then assigns $\Delta\omega$ intervals with normalized intensities higher than the threshold as being part of the high intensity reflections. The separated diffraction patterns are integrated along the azimuthal directions to form the radial profiles of the averages of continuous ring and high intensity reflections. The continuous ring then becomes purely consisting of diffraction signal from fine grains, while the high intensity reflections are a mix of signal from coarse and fine grains. The fraction of continuous ring signal in the high intensity reflections is estimated and is assumed to have the same radial profile as the continuous ring. By subtracting the fraction of continuous ring radial profile from the high intensity reflections, the radial profile of pure coarse grain is obtained.

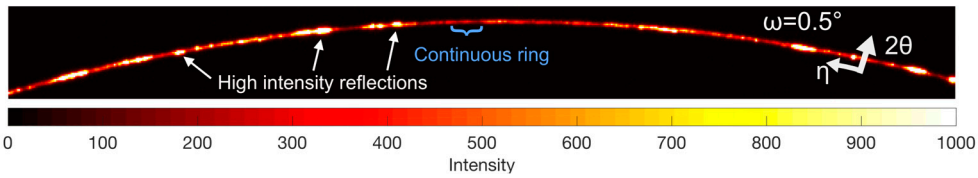

Figure 4.5 Typical section of the first Debye-Scherrer ring for one Δω interval showing an arc in η of about 30°. The high-intensity reflections originate from coarse grains, while the low-intensity continuous ring comes from fine grains.

Note, the grain size threshold is not known *a priori* in this algorithm. It can only be estimated by checking the ratio of integrated intensity from fine and coarse grains. With access to the ratio between scattering volume and integrated intensity, it would be possible to check the size of the grain with the smallest resolvable reflection. Moreover, the coarse grains could be classified into different subfractions. A suitable approach to obtain the volume to integrated intensity would be to integrate the intensity of a Debye-Scherrer ring from a fine-grained texture free cylindrical rod while it is rotated 360° in ω. Then, the grain size can be calculated from the integrated intensity with appropriate corrections [120]. Apart from an appropriate specimen this method requires the knowledge of incoming beam intensity [121]. Unfortunately, we had access to neither, but this can be done in future experiments.

4.2.4.3 Data analysis

After the separation of pure radial profiles from coarse and fine grains, it becomes possible to conduct more typical powder diffraction data analysis. The radial profiles for each separated Debye-Scherrer ring are characterized with the same methods as for the single reflections in high resolution reciprocal space mapping (see section 4.2.3.2). The average elastic strains of the investigated hkl lattice planes in respective grain size fraction are equivalently measured through the change of average spacing.

When having access to several radial profiles with different scattering angles 2θ, additional data treatment can be done, since the widths from size broadening and microstrain behave differently with diffraction angle [122]. The microstrain corresponds to the atom displacement with respect to their position in a defect free crystal. For defects such as dislocations, local elastic strains are often assumed to have a Gaussian distribution and microstrain is measured as the root mean square strain, ϵ_{rms}.

Width from crystalline size evolves with the equation [123]

$$\beta^s = \frac{\lambda \mathrm{k}}{t\cos(\theta)}, \tag{4.12}$$

where k is a constant and t is the length of crystals along the diffraction vector.

The broadening from microstrain evolves with

$$\beta^{D} = 2\,\epsilon_{rms}\tan(\theta). \tag{4.13}$$

Williamson and Hall proposed that the broadening from size effects and dislocations can be deconvoluted with a simple method [124]. The breadths are additive if both broadening functions are considered Lorentzian

$$\beta^{tot} = \beta^{s} + \beta^{D}. \tag{4.14}$$

This can be rewritten as

$$\frac{\beta^{tot}\cos(\theta)}{\lambda} = \frac{k}{t} + 2\,\epsilon_{rms}\frac{\sin(\theta)}{\lambda}. \tag{4.15}$$

If the breadth is plotted with scaling factors for the position of each radial profile at $\sin(\theta)/\lambda$, a straight line is obtained, with the intercept equal to the inverse of the crystallite size and the slope corresponding to the microstrain. This type of plot is called Willamson-Hall plot. However, for plastically deformed crystals, the peak widths scatter around an imaginary line [125]. This is because the microstrains produced by dislocations are anisotropic and thus depends on the particular <uvw> direction. The visibility of dislocations by broadening in a particular direction is expressed by the contrast factor C_{hkl}, which depends on the elastic constants of a crystal and the relative orientation of a scattering vector to the dislocation line and Burgers vector [126]. By using the modified Willamson-Hall plot where the widths are plotted as a function of $\frac{\sin(\theta)}{\lambda}C_{hkl}^{1/2}$, scattering about the imaginary line is reduced, which improves the fit [127]. This method was used in ***Paper II***. Since the microstrain is proportional to the dislocation density, it can be extracted using the methods in [127, 128].

4.3 Digital image correlation

Digital image correlation (DIC) technique combines the recording of specimen images during deformation, and computational methods for tracking local changes in the images. The technique is most commonly used for measuring surface deformation, and is nowadays a standard technique for full-field measurements of displacements and strains in numerous disciplines [129]. The algorithm identifies regions of unique surface features, which can be native to the specimen or added speckle patterns, and tracks their relative displacements. The algorithm is implemented in several commercial software packages. Reviews of suitable image conditions and computational methods can for instance be found in [130-132]. The details of the implementation of the computational method are for instance available in open-source code packages such as Ncorr [129] and ADIC2D [133].

The images can be recorded with either scanning electron microscope or optical microscope. It is possible to detect the out of plane motion to measure three-dimensional deformation with optical microscopy, but only the two-dimensional in-plane surface deformation is of interest in this thesis work. The measurement of in-plane surface deformation requires the use of a single camera. To obtain images suitable for analysis, the specimen surface should be parallel with image sensor and evenly illuminated throughout the experiment [130]. Other key factors for successful imaging are temporal and spatial resolutions. Temporal resolution, or frame rate, is limited by the sensors acquisition rate. It depends on object illumination, aperture and exposure time. The exposure time should be long enough to capture sufficient light but short enough to avoid blurring of images due to the specimen motion [132]. The spatial resolution of a camera depends on the pixel size of its sensor and distortion of its lens. However, the spatial resolution of DIC also depends on the quality of native or applied surface patterns, as it is the features on the surface that allow the tracking of regions. Other factors that affect the quality includes the settings of DIC and specific choice of algorithms [131].

The principle behind subset-based DIC analysis is the following [130]. A region of interest is defined in the images and is further partitioned into small regions called subsets. By evaluating the degree of similarity between subsets through a correlation criterion, the approximate centre points of the corresponding subsets in reference image and the deformed image are found. It is very beneficial if the surface pattern is dense, random, and of high contrast, so that a small subset size can be selected. By taking into account that the subset may deform, the centre position is further refined. The subset in the reference image is transformed through a shape function to a deformed subset. Shape functions of different orders can allow varieties in the complexity of deformation. A first-order shape function allows combinations of translation, rotation, shear and normal strains [130]. The subsets in the reference image and the deformed image are also compared through a correlation criterion, and the transformation of the subset is iteratively optimized. Although the subsets consist of discreate pixels, subpixel resolution is achieved through interpolation. The difference in centre points between the subsets in the sequence of images is used as the displacement field, and a strain filed is obtained by differentiation.

Several settings affect the outcome of DIC analysis. The most significant one is the size of the subset. A small subset size is sensitive to noise, which causes low correlation [129], and moreover risks that a wrong subset may be found [129, 130]. However, the deformation of a small subset is easier to accurately approximate with a low order shape function, whereas large subsets lead to large errors in the deformation [130]. In addition, a large subset tends to smoothen the field such that localized deformation and sharp deformation gradients are not correctly captured [129]. Thus, the subset size should be as small as possible without sacrificing accuracy.

5 Results and discussion

In this chapter, the summary of main results in this thesis work is presented and discussed. The outcome of the X-ray diffraction analysis (***Paper I, II* and *III***) is discussed in section 5.1, and the DIC analysis (***Paper IV, V***) in section 5.2. The results from the two sections are correlated in section 5.3 to highlight some aspects not formulated clearly in the published papers.

5.1 Stress partitioning

The stress partitioning over the early stages of deformation was investigated *in situ* with synchrotron X-ray diffraction techniques (***Paper II* and *III*)**. The average behaviour of the fine and the coarse grain fractions was monitored in ***Paper II*** using powder diffraction. Arcs of $\pm$ 15° in η from the tensile axis (see Figure 4.3) were analysed for the first four Debye-Scherrer rings at several steps of loading. As noted in section 4.2.4.2, the Debye-Scherrer rings contain reflections from both fine and coarse grains. The separation of the continuous ring (fine grains) and the high intensity reflections (coarse grains) was accomplished through the algorithm described in ***Paper I*** and section 4.2.4.2.

Figure 5.1a shows the radial profiles of the unseparated and separated 111 ring prior to loading, and at the final loading step. The uniaxial stress and strain states at each loading step can be read from the black stress-strain curve in Figure 5.2. The total intensity (area under the curve) of a respective grain fraction corresponds to its diffracting volume. The number average ratio of continuous ring (fine grains) to the total intensity of the diffracting volume of the individual Debye-Scherrer rings at the unloaded state were 22%. Since the EBSD analysis (see section 3) showed that the area fraction of grains smaller than 5 μm is 24%, it is reasonable to presume that the algorithm discriminates grains larger and smaller than approximately 5 μm prior to loading, and thus follow the previous definition of coarse and fine grains in the thesis work (see section 3).

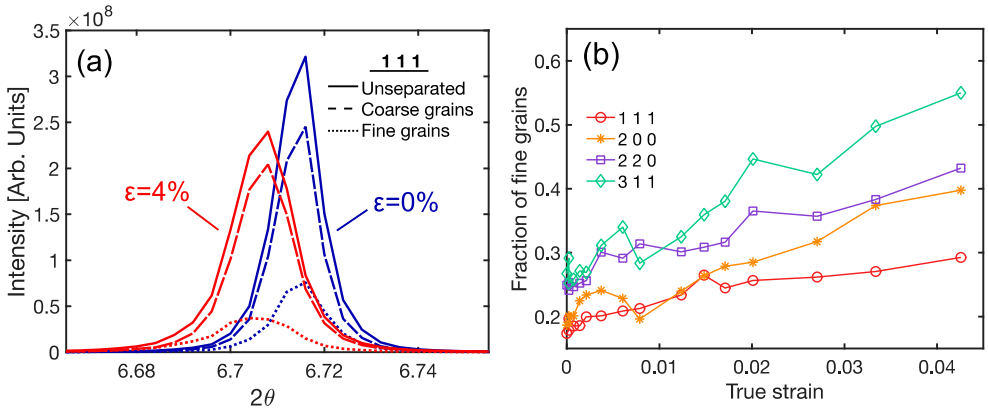

Figure 5.1 Separated and unseparated 111 radial profiles (a) at two macroscopic strain levels. Fraction of fine grains according to separation algorithm (b).

With increasing true strain, the ratio of continuous ring (fraction of fine grains) for respective Debye-Scherrer ring increases (Figure 5.1b). This might be a consequence of the subdivision of coarse grains due to plastic deformation, which leads to the spreading of high intensity reflections This causes the smooth continuous ring to comprise of a combination of intensity from fine grains and parts of high intensity reflections from subgrains in the deformed coarse grains.

Figure 5.1a shows that the peaks shift to lower $2\theta^{mean}$ and become broader with increasing applied stress and true strain. Using the peak shifts and widths, two parameters were evaluated for the two grain fractions, local average stress and apparent microstrain. The apparent microstrain correlates with dislocation density and was calculated with modified Williamson-Hall analysis. Figure 5.2 shows the evolution of average local stress and microstrain with macroscopic true strain of the respective grain fraction. It is clear that (i) fine-grained and coarse-grained fractions have quite different local stresses, and (ii) stress partitioning starts during elastic to plastic transition. The dependence of local stresses on macroscopic strain in each fraction resembles the macroscopic stress-strain curves of their homogeneous counterparts, apart from a few exceptions (see ***Paper II*** for details). Most strikingly, the onset of plastic yielding in the coarse-grained fraction of HS nickel occurs at a higher stress than in the homogenous counterpart (which will be analysed in detail later). The subsequent stress-strain response of the coarse-grained fraction and the homogenous counterpart is similar until global true strain 0.015-0.02 when the loading curve of the coarse-grained fraction becomes steeper.

If the local loading curves of the fine-grained and the coarse-grained regions are added after weighting by their respective volume fractions, the macroscopic stress-strain curve of the HS nickel is obtained. At a first glance, it appears in Figure 5.2 as if the stress-strain curve of the HS specimen, with adjustment from the apparent increased yield strength of the coarse-grained fraction, might be considered as the

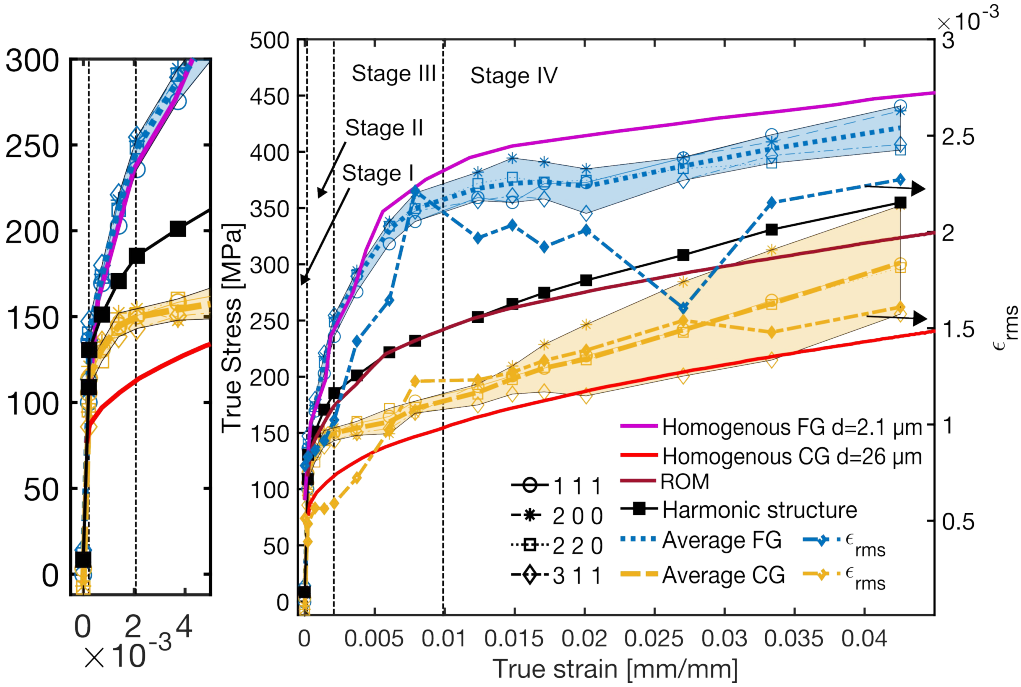

Figure 5.2 Evolution of average local stress and microstrain with macroscopic true strain of the coarse- and fine-grained fractions in HS nickel. The black curve shows the macroscopic true stress-strain curve due to the applied load while the local stresses are estimated for different grain orientations from the separated radial profiles from four Debye-Scherrer rings. Shaded areas reflect the ranges of variation of local stresses between the different grain orientations, while dashed lined represent their mean values. The microstrain for the respective grain fraction are determined from six Debye-Scherer rings using the modified Williamson-Hall analysis. True stress–strain curves of homogenous coarse-grained [81] and fine-grained [97] nickel are added from literature.

superposition of homogenous stress-strain curves. Figure 5.2 also shows the expected stress-strain response from the rule of mixtures

$$\sigma_{ROM} = f_{FG}\,\sigma_{Homo\,FG} + f_{CG}\,\sigma_{Homo\,shift\,CG}, \qquad (5.1)$$

where f_{FG} is the volume fraction of fine grains (set to $f_{FG} = 0.24$), $\sigma_{Homo\,FG}$ is the loading curve of homogenous fine grains, and $\sigma_{Homo\,shift\,CG}$ is the loading curve of homogenous coarse grains, with its yield strength shifted to match that of the coarse-grained fraction in the HS specimen. The measured macroscopic loading curve of the HS specimen and σ_{ROM} compare reasonably well until 0.02 true strain. Then, σ_{ROM} underestimates the work-hardening rate. This, as well as the different stages of deformation in Figure 5.2 will be addressed later.

The observation that the coarse grains in the HS appear to have a higher yield strength than their homogenous counterpart was further investigated in ***Paper III***. Reflections from individual grains of different size in nickel samples with harmonic structure, and individual coarse grains in a homogeneous coarse-grained structure,

were monitored with high resolution reciprocal space mapping during tensile deformation. The technique was selected because the reflection from individual grains can be traced in isolation from the background of very fine grains without using any separation algorithm. Additionally, small levels of plastic deformation can be detected at low strains.

Only grains that had their [100] direction close to parallel with the tensile axis were investigated. The grain size was estimated by scanning several grains through the beam to estimate their volume and to obtain an intensity to volume ratio. Using the ratio, the estimation of non-scanned grain sizes was also possible. Two large grains with an equivalent grain diameter of approximately 20 μm and two small grains of approximately 4 and 5 μm were investigated in the HS specimen. The large grains are representative of the coarse-grained fraction while the small grains represent the portion of large grains within the fine-grained fraction. Two grains with almost equivalent grain size of 40 μm were also investigated in the homogenous coarse-grained specimen for comparison.

The high resolution reciprocal space mapping data is analysed with two complementary projections (see section 4.2.3.2). Azimuthal maps which represent local orientation differences within the grains, and radial profiles that represents the distribution of lattice plane spacings. Examples of azimuthal maps from one coarse grain in the HS at different applied stresses is shown in Figure 5.3. Two complementary series of azimuthal maps are shown. In one series, the same fixed region in reciprocal space is presented. The upper limit of the colour scale is set to 90 % of the pixel with highest intensity in each map to give an overview of the evolution of the reflection's position and extent. To enhance fine details, magnified contour maps of the reflection are shown in the series of insets. The contour map acquired at an applied load of 10 MPa shows that the intensity distribution is clearly heterogenous with several peaks of high, but varying intensity. Each individual peak represents a local maximum in the reciprocal space corresponding to a near dislocation-free subgrain. The upper limits of colour scales in the contour maps are set to reveal the structure of the peaks of lower intensity levels.

With increasing applied stress and consequently stain, the reflection spreads in the azimuthal directions. This is due to the developing cell structure and increasing misorientation between cells with increasing strain (see section 2.2.4). Thus, changes in the orientation distribution are an indication of plastic deformation. Comparing the overview azimuthal maps at 175 MPa and 252 MPa applied stress, it is obvious that the reflection spreads and that plastic deformation occur. However, much smaller changes are visible in the magnified maps. For instance, the peaks indicated by black and red arrows at 92 MPa split at 175 MPa. This is the indication of dislocation movement and thus plastic deformation. Plastic deformation can also

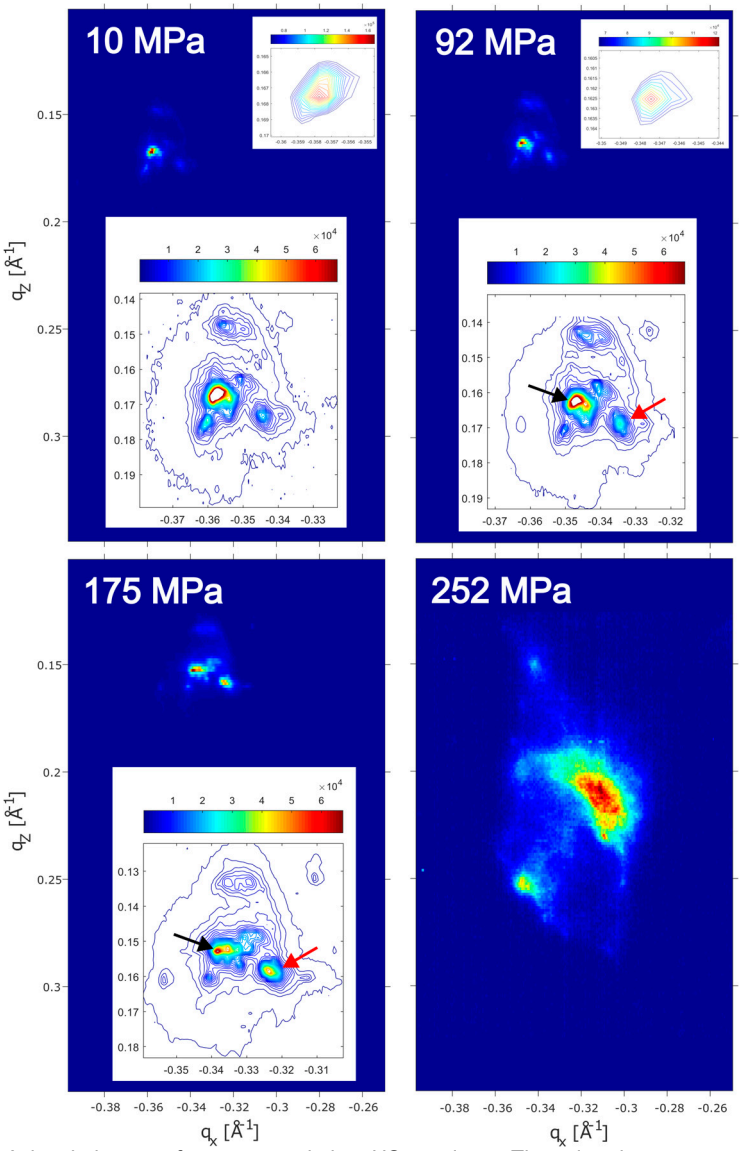

Figure 5.3 Azimuthal maps of a coarse grain in a HS specimen. The colored maps represent the same region in reciprocal space to reveal changes in position and extent. They are scaled to 90 % of the maximum pixel intensity in the map. The contour maps in the insets reveal more details of the pole distribution and the presence of individual subgrains. The large insets at the lower part for the loads 10 MPa to 175 MPa are scaled to a fraction of the integrated intensity in the reflection. A fixed color scale is used for the applied loads of 10 to 175 MPa to facilitate identification of individual subgrains and monitoring their evolution. The smaller insets at the upper-right corners of the maps for applied loads 10 MPa and 92 MPa reveal the intensities above the threshold value. During stress levels from 92 to 175 MPa small but clear changes are visible as those highlighted by black and red arrows. The highest intensity peak indicated by the black arrow splits into two peaks between 92 and 142 MPa which then move relative to each other when loading to 175 MPa. The peak indicated by red arrow displays similar behavior. The overall azimuthal intensity distribution changes considerably between 175 and 252 MPa and expands in the azimuthal directions as evident from the overview maps.

be detected by the increase of integral widths of the radial profiles from the grains. The evolution of integral width is shown in Figure 5.4a and b.

An interesting observation from ***Paper III*** was that the change in orientation and the increase of integral width do not exactly coincide. Detailed analysis of the azimuthal maps and integral widths (as outlined in ***Paper III*** and its supplementary materials) shows that the change of reflection can be categorized into: (i) no change in azimuthal map and integral width, (ii)) change in azimuthal maps but not integral width and (iii) change in azimuthal map and integral width. Hence, the deformation of a single grains was categorized into elastic deformation, small levels of plastic deformation and significant plastic deformation.

Based on such changes, the deformation in the two specimen is categorized into regimes A, B and C. The evolution of q_{mean} which correlates with average elastic strain is shown in Figure 5.4c. A sharp transition in the $q_{mean}$is shown at an applied stress of 241 MPa for the large grains. Therefore, the regime of significant plastic deformation is further subdivided into D. For the HS specimen, all grains deform elastically in regime A. In regime B, all the large grains and the largest one of the small grains undergo small levels of plastic deformation, while the smallest grain still deforms solely elastic. In regime C, all the grains undergo significant plastic deformation.

Comparing the large grains in the HS and the grains in the homogenous structure, it is interesting to note that the onset of significant plastic deformation in the large grains occurs at 175 MPa in the HS, while at 69 MPa in the coarse-grained material. This suggests that the fine-grained network restricts the large grains from deforming plastically.

The combination of the powder diffraction and high resolution reciprocal space mapping experiments allows detailed analysis of deformation mechanisms in the HS material. By comparing the stages of deformation in Figure 5.2 and the evolution of q_{mean} in the regimes in Figure 5.4c, it is possible the link the grain-level and grain size fraction deformation behaviours. In Figure 5.2, the stress-strain curve of HS material is divided into four different stages based on the most distinctive features of the local loading curve in the fine-grained fraction. The sequence starts from a linear straining (stage I), that continues with a slightly shallower but still near-linear slope (stage II), which transitions to a parabolic curve (stage III), which later stagnates and attain an almost linear shallow slope (stage IV). On the applied stress level, the stages and the regimes correspond well. Figure 5.5 displays the evolution of elastic strains in the two grain fractions obtained from the 200 Debye-Scherrer ring ([100]-direction parallel to the tensile axis, alike the individual 400 reflections).

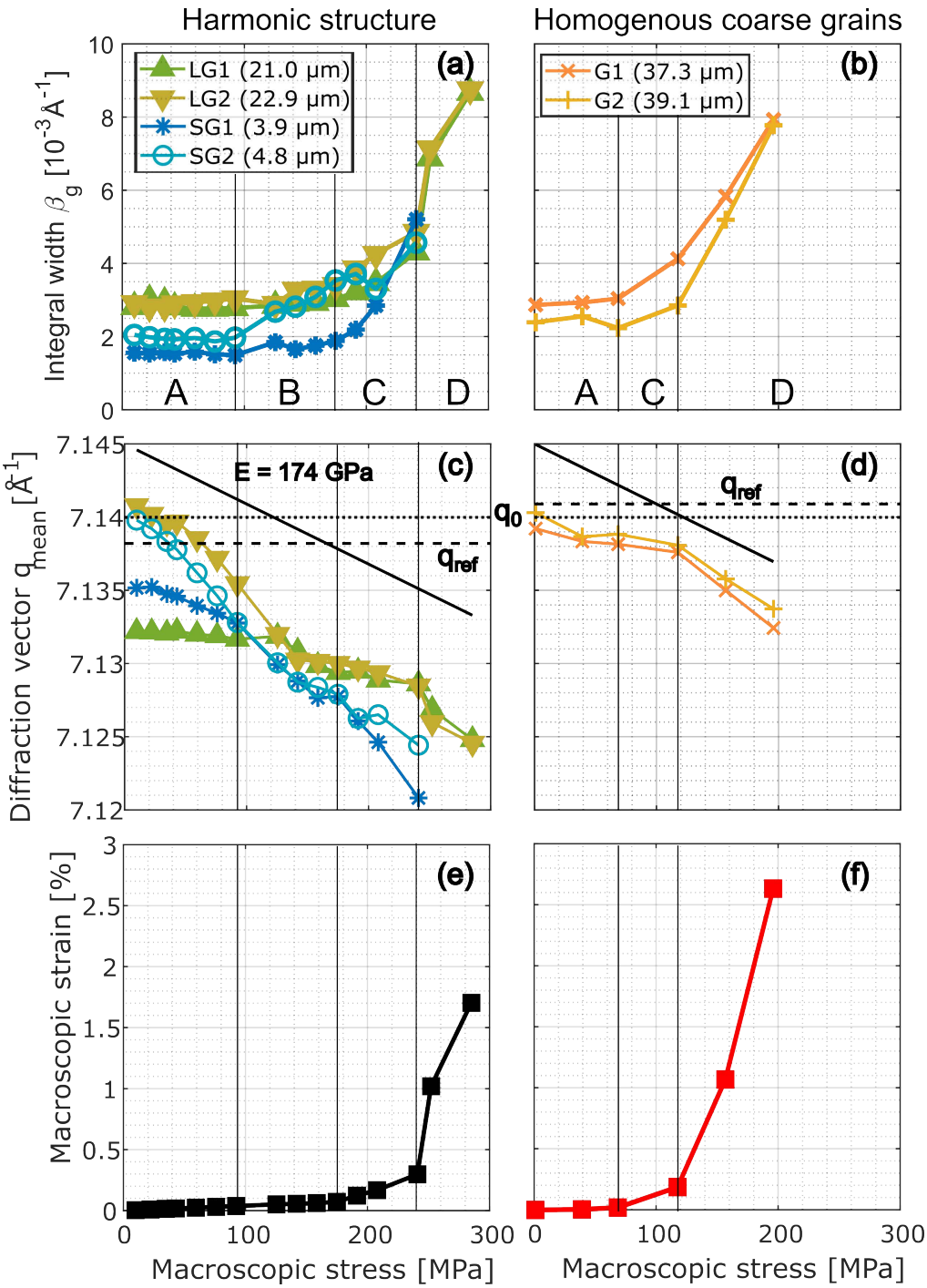

Figure 5.4 Evolution of radial profiles in the investigated grains (integral width, a-b, and peak position c-d) and extrapolated macroscopic strains for the HS (e) and the reference homogeneous coarse-grained (f) specimens with applied stress. The strains are extrapolated for load steps less than 92 MPa based on the linear behavior between the loads 125 MPa to 175 MPa.

Figure 5.4a reveals the elastic strain scatter among the grains prior to deformation. This is due to internal stresses of unknown origin. With increasing applied stress, the elastic strain homogenizes among the grains towards the end of regime A. All grains have a similar response to the applied stress in the beginning of regime B. However, toward the end of this regime, the grains start to deviate marginally as the individual grains start to show signs of small levels of plastic deformation.

It is important to note that the small grains are not the finest grains in the HS, and therefore it is reasonable to assume that these fine grains deform elastically similar to the smallest investigated grain (SG1). The large grains are constrained from deforming plastically as they normally would at the applied stress levels (compare Figure 5.4a and c with Figure 5.4b and d). Instead, the large grains undergo a combination of small amounts of plastic deformation, and primarily elastic deformation together with the fine-grained network. Figure 5.5 supports this, as the elastic strain of the coarse-grained fraction proceeds with almost the same slope at stage II as at stage I.

Moreover, the fine grains develop larger elastic strain than the coarse grains, revealing stress partitioning. This is because back stresses develop relative to the applied stress in the plastically deforming large grains, and forward stresses in the elastically deforming fine grains. The same behaviour is observed for the large and small grains in regime B (Figure 5.4c). The stress partitioning ensures compatible deformation of neighbouring grains with different resistances to plastic deformation.

The change in slope of the fine-grained fraction at stage II (Figure 5.2) indicates that parts of the fine-grained fraction start to undergo plastic deformation. The nearly linear curve is probably the consequence of the finest grains in the fraction still deforming elastically. The parabolic shape of the stress-strain curve of the fine-grained fraction during stage III suggest that most of the grains deform through plastic deformation. The regime C in Figure 5.4c also suggests that the smallest investigated grain clearly deforms plastically. Once a substantial portion of the fine-grained network deforms plastically, the large grains attain the ability to undergo significant plastic deformation, as they would do without the restrained condition.

Although all the grains deform plastically at stage III and regime C, the stress continue to partition among the fine and coarse grains (Figure 5.2, Figure 5.4c and Figure 5.5). This is because grains of different sizes have different work-hardening rates due to differences in the rate of dislocation accumulation (see section 2.2.6.1). The fine grains should accumulate dislocations faster than the coarse grains. The faster increasing flow stress and apparent microstrain in the fine-grained fraction in Figure 5.2 supports this conclusion. Eventually, the accumulation of dislocations in the fine-grained fraction stagnates, as evident from the slow increase in apparent microstrain and the low work-hardening rate at stage IV. The coarse-grained fraction still has room to accumulate dislocations, as visible from its lower apparent

microstrain, and thus still has the capacity to work-harden. The trend in local stress increase shifts, with stress startsing to concentrate in the coarse grains instead of the fine grains. This is noticeable from the slightly steeper local stress curve of the coarse-grained fraction at stage IV, and is clearly visible in Figure 5.5. The same trend is visible in regime D (Figure 5.4c), if the same shallow slope of the fine-grained fraction as in Figure 5.5 is extrapolated for the individual small grains.

The measurement of the reciprocal space has similarities with the thick yield surface introduced in section 2.4. The Debye-Scherrer rings reflect the distribution of elastic strains and thus stress states in different elements (in this case grains) within the material that form the thick yield surface. Through reciprocal space mapping, the (uniaxial) stress state of a few individual elements in the structure is measured. The stress states travel inside the yield surface during the elastic regime until penetrating its thick surface. The different elements yield at different applied macroscopic stresses confirming the usefulness of the concept of thick yield surface. Figure 5.4c and e show that over the elastic-plastic transition macroscopic plastic flow starts when a non-negligible part of the elements is on their subsequent yield surfaces. The deviation of stress states after yielding is a measure of the spreading of the cloud of internal stress [93]. The fact that a substantial part of elements needs to enter the thick yield surface before macroscopic deformation shows that HS materials can be used close to their yield strength even though some elements are considerably softer than the macroscopic. It can be said that the HS design expands the yield surface of elements compared to unconstrained (homogenous grain size) conditions.

The results from ***Paper II*** are in line with several literature sources regarding heterogenous materials in showing different stages of deformation [12-15, 77-79]. However, it is difficult to compare the evolution of average grain fraction stresses with literature as there, to my knowledge, are no other *in situ* x-ray diffraction experiments of heterogenous single-phase materials with similar morphology.

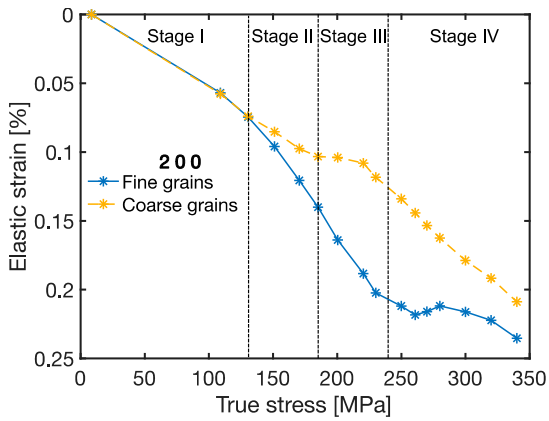

Figure 5.5 Evolution of elastic strains as a function of macroscopic true stress for the separated profiles for the 200 Debye-Scherrer ring in a HS specimen.

Nonetheless, there is an abundance of studies with *in situ* x-ray diffraction on multi-phase materials showing the evolution of phase stresses [134-139]. The stresses typically redistribute among the phases during deformation.

At low temperature, a dual-phase copper-iron alloy showed a similar tendency as the HS nickel. The stress concentrates in the hard iron phase well before macroscopic yielding, followed by a decrease in the phase stress difference due to a higher work-hardening rate of the copper phase [138]. Similar to the enhancement of the yield stress of coarse-grained fraction in the HS material, austenite was strengthened in a dual-phase steel [139]. It was shown that the soft austenite attained higher elastic strains at the point of macroscopic yielding when the surrounding hard martensite had been precipitation strengthened. The hard martensite constrains the soft austenite from plastic deformation. Additionally, it was shown for a heterogenous laminate structure of titanium that the transfer of strain from coarse grains to fine-grained layer is inhibited [140]. This led to a yield strength of the laminate structure close to the homogenous fine grains, although the structure only consisted of 11.5 % volume weight fine grains.

5.2 Strain partitioning

Tensile tests with an initial strain rate of $3.6 \times 10^{-3}\ s^{-1}$ were recorded with an optical microscope equipped with a digital camera. The camera acquired 25 frames per second with a resolution of 1920 × 1080 pixels, which corresponds to a pixel size of 2.4 μm. To reveal the microstructure, the samples were polished and etched with a sulphuric-nitric acid-based solution. Figure 5.6 shows the raw microstructure image as viewed in an optical microscope at the beginning of tensile testing. Light-grey areas represent fine-grained regions, while the dark areas are coarse-grained regions. Note this distinction is based on the optical contrast of respective areas, and may not strictly follow the grain size threshold defined earlier in the thesis. The microstructure (grain orientation) contrast was sufficient to perform DIC analysis with the commercial software 'GOM correlate'. Every 25th image was extracted from the videos, and a subset size of 38 pixels and a point distance of 20 pixels was used for the DIC to measure the strain distribution from the beginning to midway through the tensile test. In ***Paper IV***, the analysis of strain distribution was limited to the early stages of deformation, and ***Paper V*** includes the stages beyond that. The results from DIC analysis are compared with a finite element (FE) model in ref. [141] to aid the interpretation of results and to check the validity of the model.

Figure 5.7 shows equivalent strain distribution in the loading direction for harmonic structure nickel at various levels of global strains in uniaxial tension. The pattern of bright areas and dark areas in Figure 5.6 was preserved in the early parts of the tensile test but diminished with increasing global strain due to surface deformation.

It was possible to extract an overlay of the microstructure for the early parts of deformation. Contrast in the overlay is inversed compared to the optical image, i.e. dark areas represent the fine-grained regions in Figure 5.6. The equivalent strain level is indicated by the colour scheme in the legend in Figure 5.7a. White areas represent regions where correlation criterion was not met. Figure 5.7c displays the strain field within macroscopically elastic strains. The strain field is almost homogenous which confirms a quite homogeneous co-deformation of fine and coarse grain. Local strain gradients develop in several spots in the microstructure as the global strain increase. Figure 5.7e shows that the highest strain levels are observed in the centres of coarse grain areas, as indicated by white arrows. The amplitudes of local strain and the number of spots with gradients increase with global strain (Figure 5.7g). ***Paper V*** contains analysis of the strain field up to 0.174 global strain. The trend of different levels of local strain in the two grain fractions is maintained beyond 0.04 global strain, but the average local strain increases in both grain fractions. In general, the distribution of strain is consistent, at least on a qualitative level, with results from the FE simulation as well as other models and experiments [81, 142-145]. Nevertheless, the experimental DIC results are somewhat different from the model [141], which predicts the maintenance of low strain levels in the fine-grained areas and sharp strain gradients increasing until global fracture. The difference can be explained by a combination of resolution and inaccuracies in the DIC analysis and FE model. The DIC analysis is likely to measure shallower strain gradients than the reality, as the relatively large subset smoothens strain gradients. The model most likely exaggerates the strain gradients, since it is based on a larger fraction of fine grains with smaller average grain size than the experimentally tested specimen.

The experimentally defined strain partitioning and the divergence of strain-levels in the coarse and fine-grained regions were quantified by averaging the local strain in in fine- and coarse-grained regions. The dependence of average local engineering strain in each grain fraction on global true strain is shown in Figure 5.8. The true

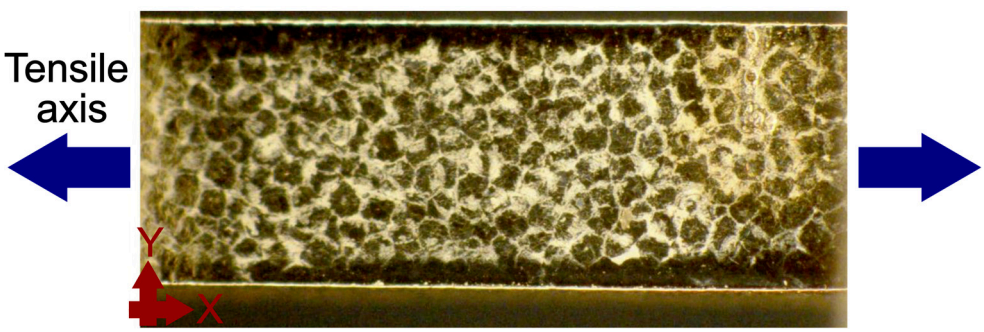

Figure 5.6 Surface features of HS sample at the beginning of tensile testing.

stress-strain curve of the tensile test is also displayed for direct comparison. Figure 5.8 shows that the local strains accumulate homogenously in both grain fractions until approximately 0.015-0.02 global true strain, and then deviate. The local strain in the coarse-grained fraction increases at a high rate until approximately 0.06 global strains and at a considerably lower rate subsequently. The local strain in the fine-grained fraction increases with a low rate until 0.08 global true strain and then accelerate. The strain accumulation is similar in both grain fractions beyond 0.1 global strain.

The strain partitioning may lead to synergetic effects. The faster accumulation of local strain in the coarse grains compared to the global true strain should lead to an acceleration of their work-hardening, and thus to an increase of work-hardening in the HS material. The slow accumulation of local strain in the fine grains reduces the consumption of their ductility resources, which delays their fracture to the later stages of global deformation.

Previous studies have shown that the ordered periodic structure of HS materials creating the continuous network of fine grains is important for their tensile properties [17, 146]. It has been shown for several different pure metals and alloys that the network has some effect on the yield strength and work-hardening behaviour but is decisive for the elongation to failure [10, 81, 146, 147]. Thus, the network seems to delay the onset of necking and the subsequent fracture. ***Paper V*** attempts

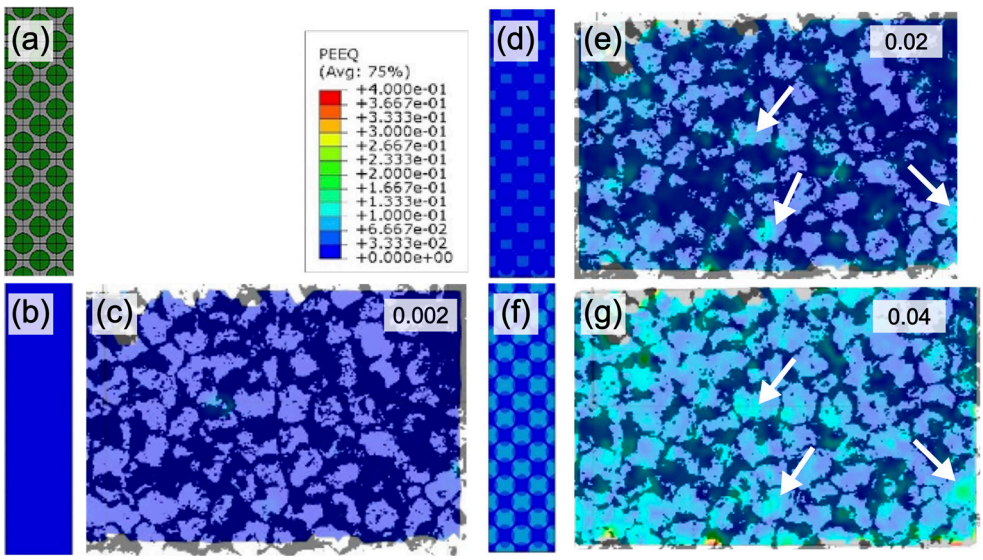

Figure 5.7 Evolution of local equivalent strain distribution for different significant global strain levels, with the local strain levels indicated by the legend in (a), for the FE model in the left column and DIC in the right column. Green and gray in (a) indicate the location of the coarse-grained and fine-grained fractions, respectively, in the FE model. Dark areas in the overlay of DIC (c,e,g) shows the location of fine grains.

to further clarify the origin of the delayed onset of necking by comparing the strain localization behaviour in HS nickel (with a continuous network) and bimodal random structure nickel (without a continuous network). In the paper, high local strain rates are perceived as a signature of strain localization, following previous studies on Lüders deformation [148] and the Portevin-Le Chatelier effect [149]. In the sample with bimodal random structure, the site of initial strain localization and the subsequent necking and fracture coincide. In the HS sample, on the other hand, the site of first instance of local high strain appears well before failure and sweeps through the gauge section to finally settle at the site of fracture shortly before failure. This may explain the later onset of necking in the HS compared to the bimodal random sample.

The FE simulation [141] provides further details on the difference in strain localization characteristics. In the bimodal random structure, plastic strain localizes at the periphery of coarse-grained areas close to the thin regions of fine grains, and then propagates almost perpendicular to the tensile axis through the shortest path of coarse-grained areas that are separated by thin areas of fine grains. This causes plastic strain to localize in a small area within the gauge section. In the HS, plastic strain localizes in the centre of coarse-grained areas and then propagates in a tortuous zig-zag pattern through the thin areas of fine grains.

The high level of plastic strain is distributed over a relatively larger area within the gauge section than in the sample with bimodal random structure. In summary, the continuous network of fine grains in the HS material seems to effectively delocalize plastic strain. This pushes the occurrence of the critical levels of plastic strain to higher global strain levels.

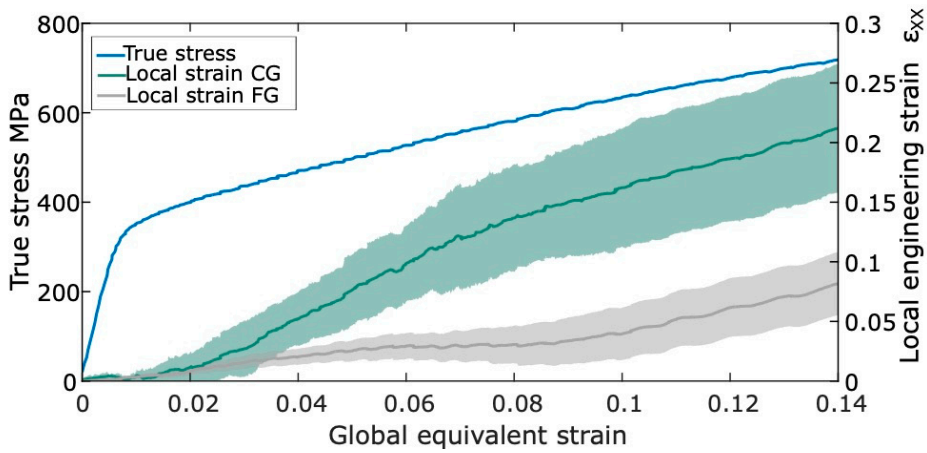

Figure 5.8 True stress (left axis) and average local engineering strain in the coarse-grained and fine-grained areas (right axis) in dependence of macroscopic true strain. Shaded areas show 95% confidence interval.

5.3 Unification of stress and strain partitioning

The purpose of this section is to give a more coherent understanding of deformation mechanisms in the HS material by aligning the results from the stress and strain partitioning studies. Furthermore, some aspects that have not been explicitly addressed in any of the appended papers will be discussed.

Figure 5.8 shows that the local strains in the coarse and fine-grained fractions are similar until 0.015 - 0.02 global true strain. This indicates the equality of average elastic modulus and homogenous co-deformation in the fractions. The local strain of each grain fraction deforms with the global imposed strain, i.e., an iso-strain condition. The iso-strain condition is maintained beyond yielding within the grain fractions due to the development of positive forward stresses ($\sigma_{forward}$) in the fine grains and negative back stresses (σ_{back}) in the coarse grains. This causes the grain fractions to have local stresses that are different from the global stress, as evident from Figure 5.2 and Figure 5.9.

The stress partitioning ensures that the local total strains of the two fractions are equivalent although the fractions have differences in yield strengths and evolution of resistance to further plastic deformation with increasing strain. The local stress of the fine-grained fraction (σ_{FG}) is the combination of applied stress (σ_{macro}) and $\sigma_{forward}$ such that and the local stress is

$$\sigma_{FG} = \sigma_{macro} + \sigma_{forward}, \tag{5.2}$$

and the stress of the of the coarse-grained fraction (σ_{CG}) likewise is

$$\sigma_{CG} = \sigma_{macro} + \sigma_{back}. \tag{5.3}$$

When scaled with volume fraction of each grain fraction the total internal stress must vanish such that

$$f_{FG}\,\sigma_{forward} + f_{CG}\,\sigma_{back} = 0, \tag{5.4}$$

where f_{FG} and f_{CG} are the volume fractions of the fine and coarse grains respectively.

Figure 5.9 shows the same loading curves as in Figure 5.2, but without the Debye-Scherrer ring-specific curves, and with two new curves added. The first is the evolution of $|\sigma_{back}|$ measured as the difference between σ_{macro} and σ_{CG}. The second is the loading curve of homogenous coarse grains with its yield strength shifted to match that of the coarse-grained fraction in the HS specimen ($\sigma_{Homo\ shift\ CG}$). The curve denoted ROM is, as in equation (5.1), based on the rule of mixtures between the shifted curve and homogenous fine grains. Interestingly, the development of back stress in the coarse-grained fraction and its work-hardening

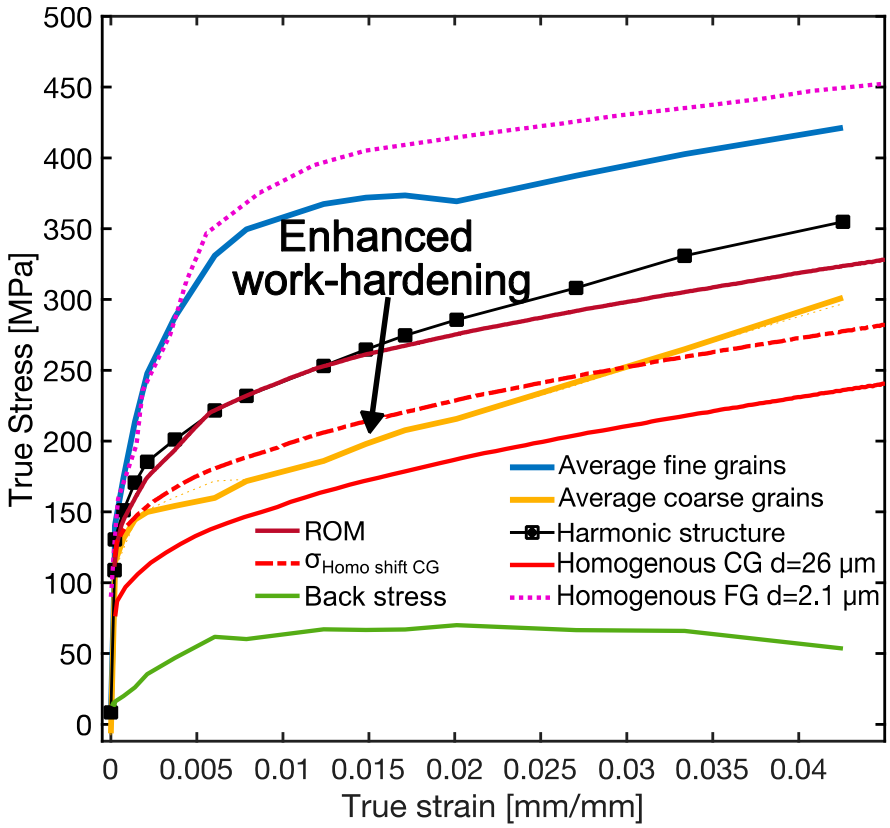

Figure 5.9 Evolution of average local stress in the of the coarse- and fine-grained fractions in HS nickel and its macroscopic true stress with macroscopic true strain. True stress – strain curves of homogenous coarse-grained [81] and fine-grained [97] nickel are added from literature. The curves are obtained with the same method as in Figure 5.2. Back stress is the differences between average stress in the coarse grains and the HS. The homogenous coarse-grained curve is shifted to the same yield strength as the coarse-grained fraction in the HS to highlight their differences. Similarly, to clarify differences between rule of mixtures and the HS, a stress-strain curve according to rule of mixtures based on the homogenous fine-grained curve and the shifted coarse-grains curve is added.

rate does not seem correlate. This can be seen from that the work-hardening rate of the coarse-grained fraction and its homogenous counterpart is similar (Figure 5.2 and Figure 5.9). This demonstrates that the high work-hardening rate of the HS material results from the inherently high work-hardening rate of the fine-grained fraction within the strain range, which adds to the characteristic slow work-hardening of the coarse-grained fraction. Importantly, this indicates that the back stress is not necessary, or at least does not play a decisive role, for explaining the high work-hardening rate of the HS material. This is different from general description of heterostructure materials in references [12-15, 77-79] in section 2.3 and specific studies on harmonic structure materials [142], which attributes the high work-hardening rate to the back stress.

Notably, Figure 5.9 reaches a peak in back stress, to then decline, while other studies show a steady increase. This is because only intergranular back stress is incorporated, while studies based on LUR measure the average back stress, which also includes intragranular back stresses. Development of such stresses are visible in Figure 5.10. The transition from symmetric to asymmetric radial profiles with increasing applied stress is shown for a large grain in the HS specimen (Figure 5.10a) and a grain in the reference specimen of homogenous coarse grains (Figure 5.10b). The longer tails towards low q-values of radial profiles with their diffraction vector parallel to the tensile direction, are related to developing forward stresses in the dislocation walls and back stresses in the subgrains [115, 150]. The evolution of absolute asymmetry in large grains in the HS specimen and grains in the reference specimen with increasing stress and strain are shown in Figure 5.10c and d. The vertical lines indicate the onsets of regime D in the respective specimen. Interestingly, regime D is associated with an abrupt increase in absolute asymmetry and, consequently, intragranular stresses in both specimens.

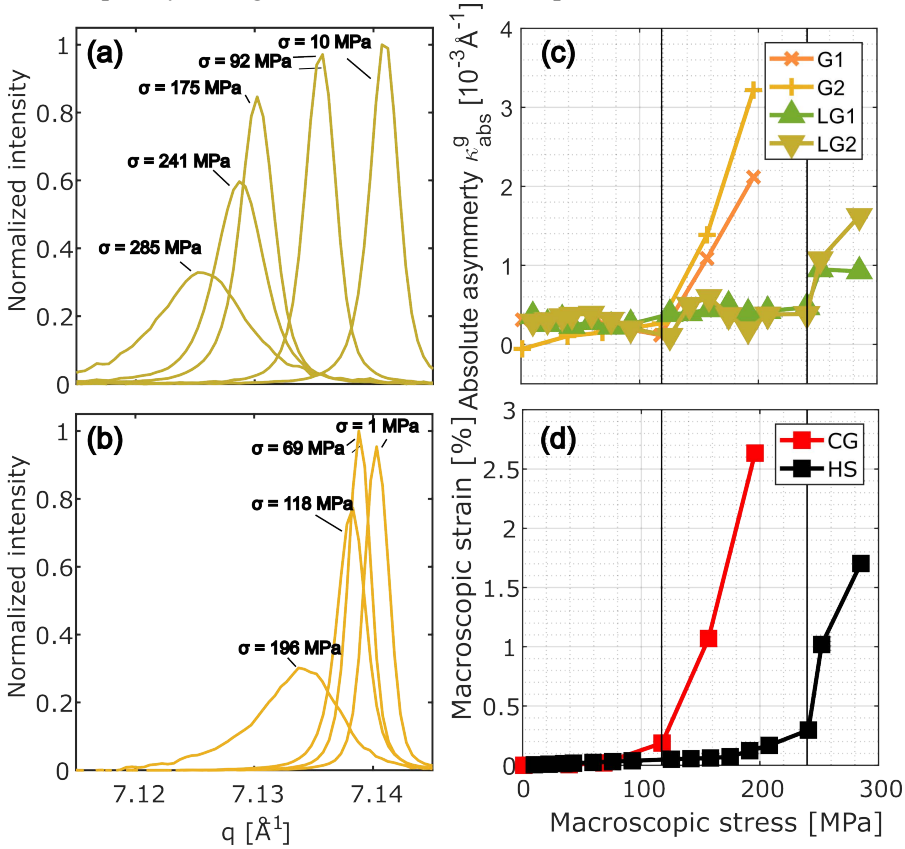

Figure 5.10 Development of asymmetric radial profiles with applied stress for a large grain in HS specimen (a) and a grain in specimen of homogenous coarse grains (b). Evolution of absolute asymmetry in the investigated grains (c) and extrapolated macroscopic strains for the HS and the reference homogeneous coarse-grained (d) specimens with applied stress.

Turning back to Figure 5.9, comparison of the shifted homogenous coarse-grained curve ($\sigma_{Homo\ shift\ CG}$) with the loading curve of the coarse-grained fraction shows that the work-hardening rate of the coarse-grained fraction accelerates relative to the homogenous counterpart at approximately 0.015 true strain. This might be a consequence of the separation algorithm struggling to distinguish the reflections from coarse and fine grains when the plastic deformation becomes pronounced. This may explain why the local stress in the coarse-grained fraction is higher than in the homogenous counterpart, while the fine-grained fraction shows lower local stress. Nevertheless, the interpretation that the work-hardening rate of the coarse-grained fraction increases is still reasonable. This is supported by the fact that the measured stress-strain curve of the HS also starts to have a higher work-hardening rate than expected from rule of mixtures. This is clearly visible in Figure 5.9 starting from 0.02 global true strain, which means that the work-hardening rate of some component in the HS increases. Interestingly, the increase of work-hardening rate in the coarse-grained fraction corresponds with the strain partitioning at 0.015-0.02 global true strain. Thus, the work-hardening rate of the coarse-grained fraction appears to increase because the local strain in the coarse-grained fraction increases more than the global strain. This causes the work-hardening rate of the HS material to increase more than can be expected from the rule of mixtures.

Based exclusively on the experimental results from this work, it is not possible to tell if the increase of work-hardening rate can solely be attributed to the acceleration of local strain, or if other effects also contribute. Several experimental and modelling studies have shown high densities of GND to accumulate at the interface of coarse and fine grains [142, 143, 145]. It is possible that the local increase of total dislocation density helps to enhance the work-hardening rate.

Nevertheless, the results from DIC in this work hint at synergetic effects of the HS material. Figure 5.8 shows that the local strains continue to concentrate in the coarse-grained fraction until 0.1 global true strain. Thereafter, the strain increases similarly in both the fractions while keeping the accumulated difference in local strain. The FE modelling suggests that the differences in local strain should be maintained until fracture. However, this could not be confirmed by the DIC since the measurement of local strains cannot be correlated beyond 0.2 global true strain. Figure 2.8a showed that the HS and the homogenous counterpart have similar levels of uniform elongation. This advocates the existence of a synergetic effect in the HS, which helps the coarse-grained and the fine-grained fraction to sustains higher average local strains than in their homogenous counterparts.

6 Summary and outlook

6.1 Summary

The work presented in this thesis has significantly advanced the understanding of deformation mechanisms in harmonic structures based on experimental studies using advanced X-ray diffraction and optical digital image correlation techniques. The harmonic structure constitutes of fractions of fine and coarse grains where the fine grains are arranged in a continuous network that surrounds islands of coarse grains. The experiments have been aimed at monitoring the interplay between the fractions in terms of stress and strain.

An algorithm capable of separating the diffraction pattern from fine and coarse grains with the same chemistry and crystal structure was developed. This algorithm can be considered as an extra step in the analysis of typical powder diffraction data It enabled grain fraction-resolved analysis of stress and microstrain in harmonic-structure materials for the first-time. High resolution reciprocal space mapping was also used for the analysis of individual grains in each fraction of harmonic as well as homogenous coarse-grained structure. Optical digital image correlation was used for the measurement of strain field and strain-rate field evolution.

Based on these studies, the following can be concluded:

- Coarse grains in harmonic structure have a higher yield strength than in a homogeneous counterpart because they are constrained from undergoing significant plastic deformation until significant yielding in fine grains.
- From early stages of elastic-plastic transitions, stress begins to partition between the grain fractions, and back stress develops. At the developed plastic deformation, strain also partitions between the grain fractions.
- As long as the local strains in the grain fractions are similar to the macroscopic strain, the stress-strain behaviour of the grain fractions is similar to their homogenous counterparts. This shows that the high work-hardening rate in the harmonic structure is the superposition of fine and coarse grains with inherited high and low work-hardening rates, respectively. The developing back stress seems not to correlate with work-hardening rate in each fraction.

- This work also proves the advantages of using *in situ* methods and their maturity in the analysis of deformation mechanisms in heterogenous-structure materials.

6.2 Outlook

Despite major advances in understanding deformation mechanisms in harmonic structure materials, this work must be considered as a major milestone rather than conclusive finish in such studies. Much more remains to be done to fully understand the deformation mechanism of harmonic structure materials. In particular, the experimental campaign fell short of clarifying the synergetic effects in the harmonic structure at the developed stages of plastic deformation and fracture. Even in the present cutting-edge instrumentation and data analysis, diffraction patterns from fine and coarse grains become too similar for reliable separation. Furthermore, the resolution of local strain in optical DIC experiments can be improved. By developing the FE model and the resolution of DIC further, it will be possible to better correlate the model and the experiments. With a model that matches experiments, it is possible to draw conclusions regarding details that will be difficult to capture experimentally, such as stress partitioning at the developed stages of plastic deformation and strain localization.

The DIC showed that strain partitioning coincides with an acceleration of work-hardening compared to rule of mixtures and indicates that the coarse-grained fraction can sustain higher average strains in the harmonic structure than standalone. However, no information was provided about how the partitioning is accomplished on the microstructural level. Combining SEM-based DIC and EBSD during tensile deformation will enable to take into consideration local grain orientations and global texture and to develop crystal-plasticity base FE models.

The SEM-based DIC will allow high resolution measurements of strain sufficient to measurement strain gradients in the coarse-graine fraction and strain in the fine-grained fraction. The combination of DIC and EBSD enables measurement of the evolution of density of geometrically necessary dislocations, and rotation of individual grains, with local strain. This is important for understanding how compatible deformation at the interface of fine- and coarse-grained fractions is maintained, while the accumulated local strains in the grains fractions diverge.

With the development of appropriate computational models, the optimal design of the harmonic structure from particular application perspectives should be easier to achieve.

7 References

[1] R. O. Ritchie, The conflicts between strength and toughness, Nature Materials 10 (2011) 817-822.

[2] Y. Wei, Y. Li, L. Zhu, Y. Liu, X. Lei, G. Wang, Y. Wu, Z. Mi, J. Liu, H. Wang, H. Gao, Evading the strength–ductility trade-off dilemma in steel through gradient hierarchical nanotwins, Nature Communications 5 (2014) 3580.

[3] C. C. Tasan, M. Diehl, D. Yan, M. Bechtold, F. Roters, L. Schemmann, C. Zheng, N. Peranio, D. Ponge, M. Koyama, K. Tsuzaki, D. Raabe, An Overview of Dual-Phase Steels: Advances in Microstructure-Oriented Processing and Micromechanically Guided Design, Annual Review of Materials Research 45 (2015) 391-431.

[4] E. O. Hall, The deformation and ageing of mild steel: III Discussion of results, Proceedings of the Physical Society. Section B 64 (1951) 747-753.

[5] N. J. Petch, The Cleavage Strength of Polycrystals, Journal of Iron and Steel Research, International 174 (1953) 25-28.

[6] Y. Estrin, A. Vinogradov, Extreme grain refinement by severe plastic deformation: A wealth of challenging science, Acta Materialia 61 (2013) 782-817.

[7] Y. M. Wang, E. Ma, Strain hardening, strain rate sensitivity, and ductility of nanostructured metals, Materials Science and Engineering: A 375-377 (2004) 46-52.

[8] X. Wu, M. Yang, F. Yuan, G. Wu, Y. Wei, X. Huang, Y. Zhu, Heterogeneous lamella structure unites ultrafine-grain strength with coarse-grain ductility, Proceedings of the National Academy of Sciences 112 (2015) 14501.

[9] Y. Xia, K. Miao, H. Wu, L. Geng, C. Xu, C.-S. Ku, G. Fan, Superior strength-ductility synergy of layered aluminum under uniaxial tensile loading: The roles of local stress state and local strain state, International Journal of Plasticity 152 (2022) 103240.

[10] C. Sawangrat, S. Kato, D. Orlov, K. Ameyama, Harmonic-structured copper: performance and proof of fabrication concept based on severe plastic deformation of powders, Journal of Materials Science 49 (2014) 6579-6585.

[11] T. H. Fang, W. L. Li, N. R. Tao, K. Lu, Revealing Extraordinary Intrinsic Tensile Plasticity in Gradient Nano-Grained Copper, Science 331 (2011) 1587.

[12] E. Ma, T. Zhu, Towards strength–ductility synergy through the design of heterogeneous nanostructures in metals, Materials Today 20 (2017) 323-331.

[13] Y. Ma, M. Yang, F. Yuan, X. Wu, A Review on Heterogeneous Nanostructures: A Strategy for Superior Mechanical Properties in Metals, Metals, 2019.

[14] Y. Zhu, K. Ameyama, P. M. Anderson, I. J. Beyerlein, H. Gao, H. S. Kim, E. Lavernia, S. Mathaudhu, H. Mughrabi, R. O. Ritchie, N. Tsuji, X. Zhang, X. Wu, Heterostructured materials: superior properties from hetero-zone interaction, Materials Research Letters 9 (2021) 1-31.

[15] Y. Zhu, X. Wu, Heterostructured materials, Progress in Materials Science 131 (2023) 101019.

[16] X. Wu, P. Jiang, L. Chen, F. Yuan, Y. T. Zhu, Extraordinary strain hardening by gradient structure, Proceedings of the National Academy of Sciences 111 (2014) 7197.

[17] K. Ameyama, F. Cazes, H. Couque, G. Dirras, S. Kikuchi, J. Li, F. Mompiou, K. Mondal, D. Orlov, B. Sharma, D. Tingaud, S. K. Vajpai, Harmonic structure, a promising microstructure design, Materials Research Letters 10 (2022) 440-471.

[18] D. L. Cederberg, M. Christiansen, S. Ekroth, J. Engman, B. Fabech, K. Guðjónsdóttir, J. T. Håland, I. Jónsdóttir, P. Kostaomo, C. Legind, Food contact materials-metals and alloys: Nordic guidance for authorities, industry and trade, Nordic Council of Ministers 2015.

[19] R. Davis, A. Singh, M. J. Jackson, R. T. Coelho, D. Prakash, C. P. Charalambous, W. Ahmed, L. R. R. da Silva, A. A. Lawrence, A comprehensive review on metallic implant biomaterials and their subtractive manufacturing, The International Journal of Advanced Manufacturing Technology 120 (2022) 1473-1530.

[20] H. M. Ledbetter, R. P. Reed, Elastic Properties of Metals and Alloys, I. Iron, Nickel, and Iron-Nickel Alloys, Journal of Physical and Chemical Reference Data 2 (1973) 531-618.

[21] G. Gottstein, Physical Foundations of Materials Science, Springer-Verlag Berlin Heidelberg 2004.

[22] D. Hull, D. J. Bacon, in: D. Hull, D.J. Bacon (Eds.), Introduction to Dislocations (Fifth Edition), Butterworth-Heinemann, Oxford, 2011, pp. 171-204.

[23] in: M.V. Lubarda, V.A. Lubarda (Eds.), Intermediate Solid Mechanics, Cambridge University Press, Cambridge, 2020, pp. 3-30.

[24] in: M.V. Lubarda, V.A. Lubarda (Eds.), Intermediate Solid Mechanics, Cambridge University Press, Cambridge, 2020, pp. 31-50.

[25] C. L. Dym, I. H. Shames, in: C.L. Dym, I.H. Shames (Eds.), Solid Mechanics: A Variational Approach, Augmented Edition, Springer New York, New York, NY, 2013, pp. 1-69.

[26] in: M.V. Lubarda, V.A. Lubarda (Eds.), Intermediate Solid Mechanics, Cambridge University Press, Cambridge, 2020, pp. 51-80.

[27] J. Bauschinger, Mittheilung XV: On the changes of the elastic limit and the strength of iron by straining in tension and in compression, Mittheilungen aus dem Mechanisch-Technischen Laboboratorium der Koniglichen Technischen Hochschule in Munchen 13 (1886) 1-115.

[28] R. E. Stoltz, R. M. Pelloux, The Bauschinger effect in precipitation strengthened aluminum alloys, Metallurgical Transactions A 7 (1976) 1295-1306.

[29] T. Kishi, I. Gokyu, A new relationship between pre-strain and yield stress drop due to bauschinger effect, Metallurgical Transactions 4 (1973) 390-392.

[30] X. Hu, C. Wei, H. Margolin, S. Nourbakhsh, The Bauschinger effect and the stresses in a strained single crystal, Scripta Metallurgica et Materialia 27 (1992) 865-870.

[31] A. A. Mamun, R. J. Moat, J. Kelleher, P. J. Bouchard, Origin of the Bauschinger effect in a polycrystalline material, Materials Science and Engineering: A 707 (2017) 576-584.

[32] D. Hull, D. J. Bacon, in: D. Hull, D.J. Bacon (Eds.), Introduction to Dislocations (Fifth Edition), Butterworth-Heinemann, Oxford, 2011, pp. 43-62.

[33] R. E. Smallman, A. H. W. Ngan, Modern Physical Metallurgy (Eighth Edition), Butterworth-Heinemann, Oxford, 2014, pp. 357-414.

[34] D. Hull, D. J. Bacon, in: D. Hull, D.J. Bacon (Eds.), Introduction to Dislocations (Fifth Edition), Butterworth-Heinemann, Oxford, 2011, pp. 157-169.

[35] N. Hansen, D. Kuhlmann-Wilsdorf, Low energy dislocation structures due to unidirectional deformation at low temperatures, Materials Science and Engineering 81 (1986) 141-161.

[36] N. Hansen, R. F. Mehl, A. Medalist, New discoveries in deformed metals, Metallurgical and Materials Transactions A 32 (2001) 2917-2935.

[37] D. Hull, D. J. Bacon, in: D. Hull, D.J. Bacon (Eds.), Introduction to Dislocations (Fifth Edition), Butterworth-Heinemann, Oxford, 2011, pp. 1-20.

[38] D. Kuhlmann-Wilsdorf, N. Hansen, Geometrically necessary, incidental and subgrain boundaries, Scripta Metallurgica et Materialia 25 (1991) 1557-1562.

[39] B. Bay, N. Hansen, D. A. Hughes, D. Kuhlmann-Wilsdorf, Overview no. 96 evolution of f.c.c. deformation structures in polyslip, Acta Metallurgica et Materialia 40 (1992) 205-219.

[40] G. I. Taylor, Plastic strain in metals, J. Inst. Metals 62 (1938) 307-324.

[41] U. F. Kocks, The relation between polycrystal deformation and single-crystal deformation, Metallurgical Transactions 1 (1970) 1121-1143.

[42] N. Hansen, X. Huang, D. A. Hughes, Microstructural evolution and hardening parameters, Materials Science and Engineering: A 317 (2001) 3-11.

[43] R. W. Armstrong, The influence of polycrystal grain size on several mechanical properties of materials, Metallurgical and Materials Transactions B 1 (1970) 1169-1176.

[44] Z. C. Cordero, B. E. Knight, C. A. Schuh, Six decades of the Hall–Petch effect – a survey of grain-size strengthening studies on pure metals, International Materials Reviews 61 (2016) 495-512.

[45] Y. Li, A. J. Bushby, D. J. Dunstan, The Hall–Petch effect as a manifestation of the general size effect, Proceedings of the Royal Society A: Mathematical, Physical and Engineering Sciences 472 (2016) 20150890.

[46] S. N. Naik, S. M. Walley, The Hall–Petch and inverse Hall–Petch relations and the hardness of nanocrystalline metals, Journal of Materials Science 55 (2020) 2661-2681.

[47] R. W. Armstrong, 60 Years of Hall-Petch: Past to Present Nano-Scale Connections, MATERIALS TRANSACTIONS 55 (2014) 2-12.

[48] U. F. Kocks, H. Mecking, Physics and phenomenology of strain hardening: the FCC case, Progress in Materials Science 48 (2003) 171-273.

[49] F. B. Prinz, A. S. Argon, The evolution of plastic resistance in large strain plastic flow of single phase subgrain forming metals, Acta Metallurgica 32 (1984) 1021-1028.

[50] P. Haasen, A cell theory for stage IV work hardening of metals and semiconductors, Journal de Physique 50 (1989) 2445-2453.

[51] E. Nes, Modelling of work hardening and stress saturation in FCC metals, Progress in Materials Science 41 (1997) 129-193.

[52] D. A. Hughes, N. Hansen, The microstructural origin of work hardening stages, Acta Materialia 148 (2018) 374-383.

[53] Y. Estrin, H. Mecking, A unified phenomenological description of work hardening and creep based on one-parameter models, Acta Metallurgica 32 (1984) 57-70.

[54] I. S. Yasnikov, Y. Kaneko, M. Uchida, A. Vinogradov, The grain size effect on strain hardening and necking instability revisited from the dislocation density evolution approach, Materials Science and Engineering: A 831 (2022) 142330.

[55] M. A. Meyers, A. Mishra, D. J. Benson, Mechanical properties of nanocrystalline materials, Progress in Materials Science 51 (2006) 427-556.

[56] I. A. Ovid'ko, R. Z. Valiev, Y. T. Zhu, Review on superior strength and enhanced ductility of metallic nanomaterials, Progress in Materials Science 94 (2018) 462-540.

[57] J. Bach, M. Stoiber, L. Schindler, H. W. Höppel, M. Göken, Deformation mechanisms and strain rate sensitivity of bimodal and ultrafine-grained copper, Acta Materialia 186 (2020) 363-373.

[58] L. S. Toth, C. F. Gu, B. Beausir, J. J. Fundenberger, M. Hoffman, Geometrically necessary dislocations favor the Taylor uniform deformation mode in ultra-fine-grained polycrystals, Acta Materialia 117 (2016) 35-42.

[59] M. F. Ashby, The deformation of plastically non-homogeneous materials, The Philosophical Magazine: A Journal of Theoretical Experimental and Applied Physics 21 (1970) 399-424.

[60] H. Gao, Y. Huang, Geometrically necessary dislocation and size-dependent plasticity, Scripta Materialia 48 (2003) 113-118.

[61] J. Jiang, T. B. Britton, A. J. Wilkinson, Evolution of dislocation density distributions in copper during tensile deformation, Acta Materialia 61 (2013) 7227-7239.

[62] D. A. Hughes, N. Hansen, D. J. Bammann, Geometrically necessary boundaries, incidental dislocation boundaries and geometrically necessary dislocations, Scripta Materialia 48 (2003) 147-153.

[63] H. Mughrabi, Dislocation wall and cell structures and long-range internal stresses in deformed metal crystals, Acta Metallurgica 31 (1983) 1367-1379.

[64] H. Mughrabi, T. Ungár, in: F.R.N. Nabarro, M.S. Duesbery (Eds.), Dislocations in Solids, Elsevier2002, pp. 343-411.

[65] S. D. Antolovich, R. W. Armstrong, Plastic strain localization in metals: origins and consequences, Progress in Materials Science 59 (2014) 1-160.

[66] A. Pineau, A. A. Benzerga, T. Pardoen, Failure of metals I: Brittle and ductile fracture, Acta Materialia 107 (2016) 424-483.

[67] A. Considère, Memoire sur l'emploi du fer et de l'acier dans les constructions, Annales des Ponts et Chaussées I sem (1885) 574-775.

[68] I. S. Yasnikov, A. Vinogradov, Y. Estrin, Revisiting the Considère criterion from the viewpoint of dislocation theory fundamentals, Scripta Materialia 76 (2014) 37-40.

[69] S. Cheng, E. Ma, Y. M. Wang, L. J. Kecskes, K. M. Youssef, C. C. Koch, U. P. Trociewitz, K. Han, Tensile properties of in situ consolidated nanocrystalline Cu, Acta Materialia 53 (2005) 1521-1533.

[70] K. Yang, Y. Ivanisenko, A. Caron, A. Chuvilin, L. Kurmanaeva, T. Scherer, R. Z. Valiev, H. J. Fecht, Mechanical behaviour and in situ observation of shear bands in ultrafine grained Pd and Pd–Ag alloys, Acta Materialia 58 (2010) 967-978.

[71] J. Li, J. Xu, B. Guo, D. Shan, T. G. Langdon, Shear fracture mechanism in micro-tension of an ultrafine-grained pure copper using synchrotron radiation X-ray tomography, Scripta Materialia 132 (2017) 25-29.

[72] J. Li, C. Ding, W. Chen, D. Shan, B. Guo, J. Xu, Strain localization and ductile fracture mechanism of micro/mesoscale deformation in ultrafine-grained pure copper, Materials & Design 229 (2023) 111873.

[73] I. Sabirov, Y. Estrin, M. R. Barnett, I. Timokhina, P. D. Hodgson, Tensile deformation of an ultrafine-grained aluminium alloy: Micro shear banding and grain boundary sliding, Acta Materialia 56 (2008) 2223-2230.

[74] I. Sabirov, Y. Estrin, M. R. Barnett, I. Timokhina, P. D. Hodgson, Enhanced tensile ductility of an ultra-fine-grained aluminum alloy, Scripta Materialia 58 (2008) 163-166.

[75] D. Dorner, Y. Adachi, K. Tsuzaki, Periodic crystal lattice rotation in microband groups in a bcc metal, Scripta Materialia 57 (2007) 775-778.

[76] N. Jia, P. Eisenlohr, F. Roters, D. Raabe, X. Zhao, Orientation dependence of shear banding in face-centered-cubic single crystals, Acta Materialia 60 (2012) 3415-3434.

[77] X. Wu, Y. Zhu, Heterogeneous materials: a new class of materials with unprecedented mechanical properties, Materials Research Letters (2017) 1-6.

[78] Y. Zhu, X. Wu, Perspective on hetero-deformation induced (HDI) hardening and back stress, Materials Research Letters 7 (2019) 393-398.

[79] L. Romero-Resendiz, M. Naeem, Y. T. Zhu, Heterostructured Materials by Severe Plastic Deformation: Overview and Perspectives, MATERIALS TRANSACTIONS 64 (2023) 2346-2360.

[80] T. H. Chou, W. P. Li, H. W. Chang, X. H. Du, W. S. Chuang, T. Yang, Y. T. Zhu, J. C. Huang, Quantitative analysis of hetero-deformation induced strengthening in heterogeneous grain structure, International Journal of Plasticity 159 (2022) 103482.

[81] D. Orlov, J. Zhou, S. Hall, M. Ota-Kawabata, K. Ameyama, Advantages of architectured harmonic structure in structural performance, IOP Conference Series: Materials Science and Engineering 580 (2019) 012019.

[82] H. Wu, G. Fan, An overview of tailoring strain delocalization for strength-ductility synergy, Progress in Materials Science 113 (2020) 100675.

[83] Y. Wang, C. Huang, Y. Li, F. Guo, Q. He, M. Wang, X. Wu, R. O. Scattergood, Y. Zhu, Dense dispersed shear bands in gradient-structured Ni, International Journal of Plasticity 124 (2020) 186-198.

[84] F. Yuan, D. Yan, J. Sun, L. Zhou, Y. Zhu, X. Wu, Ductility by shear band delocalization in the nano-layer of gradient structure, Materials Research Letters 7 (2019) 12-17.

[85] Y. F. Wang, C. X. Huang, Q. He, F. J. Guo, M. S. Wang, L. Y. Song, Y. T. Zhu, Heterostructure induced dispersive shear bands in heterostructured Cu, Scripta Materialia 170 (2019) 76-80.

[86] A. Godfrey, W. Q. Gao, G. M. Le, C. L. Zhang, K. N. Zhu, Local deformation mechanisms in metal systems with a tailored grain size distribution, IOP Conference Series: Materials Science and Engineering 1249 (2022) 012006.

[87] in: W.F. Hosford (Ed.), Solid Mechanics, Cambridge University Press, Cambridge, 2010, pp. 67-83.

[88] U. F. Kocks, C. N. Tomé, H. R. Wenk, Texture and Anisotropy: Preferred Orientations in Polycrystals and Their Effect on Materials Properties, Cambridge University Press, 2000, pp. 326-389.

[89] J. F. W. Bishop, R. Hill, XLVI. A theory of the plastic distortion of a polycrystalline aggregate under combined stresses, The London, Edinburgh, and Dublin Philosophical Magazine and Journal of Science 42 (1951) 414-427.

[90] H. Mecking, in: K.H.J. Buschow, R.W. Cahn, M.C. Flemings, B. Ilschner, E.J. Kramer, S. Mahajan, P. Veyssière (Eds.), Encyclopedia of Materials: Science and Technology, Elsevier, Oxford, 2001, pp. 9785-9794.

[91] P. Lequeu, P. Gilormini, F. Montheillet, B. Bacroix, J. J. Jonas, Yield surfaces for textured polycrystals—I. Crystallographic approach, Acta Metallurgica 35 (1987) 439-451.

[92] Y. E. Beygelzimer, A. V. Spuskanyuk, The thick yield surface: Idea and approach for investigating its structure, Philosophical Magazine A 79 (1999) 2437-2459.

[93] Y. Beygelzimer, A. Spuskanyuk, V. Varyukhin, On the Loading Surface of Microinhomogeneous Materials, 2001.

[94] C. Cai, K. Zhou, in: C.D. Patel, C.-H. Chen (Eds.), Digital Manufacturing, Elsevier2022, pp. 247-298.

[95] D. C. Joy, N. W. M. Ritchie, J. R. Michael, D. E. Newbury, J. Goldstein, J. H. J. Scott, Scanning Electron Microscopy and X-Ray Microanalysis, Fourth edition ed., Springer 2018.

[96] C. Suryanarayana, Mechanical alloying and milling, Progress in Materials Science 46 (2001) 1-184.

[97] M. Nagata, N. Horikawa, M. Kawabata, K. Ameyama, Effects of Microstructure on Mechanical Properties of Harmonic Structure Designed Pure Ni, Materials Transactions 60 (2019) 1914-1920.

[98] U. Anselmi-Tamburini, in: M. Pomeroy (Ed.), Encyclopedia of Materials: Technical Ceramics and Glasses, Elsevier, Oxford, 2021, pp. 294-310.

[99] M. Tokita, in: S. Somiya (Ed.), Handbook of Advanced Ceramics (Second Edition), Academic Press, Oxford, 2013, pp. 1149-1177.

[100] A. J. Wilkinson, P. B. Hirsch, Electron diffraction based techniques in scanning electron microscopy of bulk materials, Micron 28 (1997) 279-308.

[101] R. Borrajo-Pelaez, P. Hedström, Recent Developments of Crystallographic Analysis Methods in the Scanning Electron Microscope for Applications in Metallurgy, Critical Reviews in Solid State and Materials Sciences 43 (2018) 455-474.

[102] L. A. Giannuzzi, J. R. Michael, Comparison of Channeling Contrast between Ion and Electron Images, Microscopy and Microanalysis 19 (2013) 344-349.

[103] M. Yang, Y. Pan, F. Yuan, Y. Zhu, X. Wu, Back stress strengthening and strain hardening in gradient structure, Materials Research Letters 4 (2016) 145-151.

[104] S. Gao, K. Yoshino, D. Terada, Y. Kaneko, N. Tsuji, Significant Bauschinger effect and back stress strengthening in an ultrafine grained pure aluminum fabricated by severe plastic deformation process, Scripta Materialia 211 (2022) 114503.

[105] V. V. Stolyarov, Structure Refinement and Bauschinger Effect in fcc and hcp Metals, Metals, 2023.

[106] P. Willmott, An Introduction to Synchrotron Radiation2019, pp. 51-106.

[107] N. Schell, A. King, F. Beckmann, T. Fischer, M. Müller, A. Schreyer, The High Energy Materials Science Beamline (HEMS) at PETRA III, Materials Science Forum 772 (2014) 57-61.

[108] Z. Hegedüs, T. Müller, J. Hektor, E. Larsson, T. Bäcker, S. Haas, A. L. C. Conceiçao, S. Gutschmidt, U. Lienert, Imaging modalities at the Swedish Materials Science beamline at PETRA III, IOP Conference Series: Materials Science and Engineering 580 (2019) 012032.

[109] A. González, in: E.H. Egelman (Ed.), Comprehensive Biophysics, Elsevier, Amsterdam, 2012, pp. 64-91.

[110] R. Guinebretière, X-ray Diffraction by Polycrystalline Materials2007, pp. 1-38.

[111] T. Ungár, Microstructural parameters from X-ray diffraction peak broadening, Scripta Materialia 51 (2004) 777-781.

[112] C. Wejdemann, H. F. Poulsen, U. Lienert, W. Pantleon, In Situ Observation of the Dislocation Structure Evolution During a Strain Path Change in Copper, JOM 65 (2013) 35-43.

[113] B. Jakobsen, H. F. Poulsen, U. Lienert, J. Almer, S. D. Shastri, H. O. Sørensen, C. Gundlach, W. Pantleon, Formation and Subdivision of Deformation Structures During Plastic Deformation, Science 312 (2006) 889.

[114] B. Jakobsen, H. F. Poulsen, U. Lienert, W. Pantleon, Direct determination of elastic strains and dislocation densities in individual subgrains in deformation structures, Acta Materialia 55 (2007) 3421-3430.

[115] B. Jakobsen, U. Lienert, J. Almer, H. F. Poulsen, W. Pantleon, Direct observation of strain in bulk subgrains and dislocation walls by high angular resolution three-dimensional X-ray diffraction, Materials Science and Engineering: A 483-484 (2008) 641-643.

[116] W. Pantleon, C. Wejdemann, B. Jakobsen, U. Lienert, H. F. Poulsen, Evolution of deformation structures under varying loading conditions followed in situ by high angular resolution 3DXRD, Materials Science and Engineering: A 524 (2009) 55-63.

[117] T. H. De Keijser, J. I. Langford, E. J. Mittemeijer, A. B. P. Vogels, Use of the Voigt function in a single-line method for the analysis of X-ray diffraction line broadening, Journal of Applied Crystallography 15 (1982) 308-314.

[118] C. Wejdemann, U. Lienert, W. Pantleon, Reversal of asymmetry of X-ray peak profiles from individual grains during a strain path change, Scripta Materialia 62 (2010) 794-797.

[119] C. Wejdemann, U. Lienert, W. Pantleon, In situ measurements of X-ray peak profile asymmetry from individual grains, Journal of Physics: Conference Series 240 (2010) 012160.

[120] E. M. Lauridsen, D. J. Jensen, H. F. Poulsen, U. Lienert, Kinetics of individual grains during recrystallization, Scripta Materialia 43 (2000) 561-566.

[121] B. Jakobsen, In-situ studies of bulk deformation structures: Static properties under load and dynamics during deformation, Roskilde University, Roskilde, 2006.

[122] A. R. Stokes, A. J. C. Wilson, The diffraction of X rays by distorted crystal aggregates - I, Proceedings of the Physical Society 56 (1944) 174.

[123] P. Scherrer, Bestimmung der Größe und der inneren Struktur von Kolloidteilchen mittels Röntgenstrahlen, Nachrichten von der Gesellschaft der Wissenschaften zu Göttingen, Mathematisch-Physikalische Klasse 1918 (1918) 98-100.

[124] G. K. Williamson, W. H. Hall, X-ray line broadening from filed aluminium and wolfram, Acta Metallurgica 1 (1953) 22-31.

[125] A. Borbély, The modified Williamson-Hall plot and dislocation density evaluation from diffraction peaks, Scripta Materialia 217 (2022) 114768.

[126] T. Ungár, Dislocation densities, arrangements and character from X-ray diffraction experiments, Materials Science and Engineering: A 309-310 (2001) 14-22.

[127] T. Ungár, A. Borbély, The effect of dislocation contrast on x-ray line broadening: A new approach to line profile analysis, Applied Physics Letters 69 (1996) 3173-3175.

[128] Á. Révész, T. Ungár, A. Borbély, J. Lendvai, Dislocations and grain size in ball-milled iron powder, Nanostructured Materials 7 (1996) 779-788.

[129] J. Blaber, B. Adair, A. Antoniou, Ncorr: Open-Source 2D Digital Image Correlation Matlab Software, Experimental Mechanics 55 (2015) 1105-1122.

[130] B. Pan, K. Qian, H. Xie, A. Asundi, Two-dimensional digital image correlation for in-plane displacement and strain measurement: a review, Measurement Science and Technology 20 (2009) 062001.

[131] B. Pan, Digital image correlation for surface deformation measurement: historical developments, recent advances and future goals, Measurement Science and Technology 29 (2018) 082001.

[132] M. Sutton, J.-J. Orteu, H. Schreier, Image Correlation for Shape, Motion and Deformation Measurements. Basic Concepts, Theory and Applications, 2009.

[133] D. Atkinson, T. Becker, A 117 Line 2D Digital Image Correlation Code Written in MATLAB, Remote Sensing, 2020.

[134] R. Shi, Z. Nie, Q. Fan, G. Li, Elastic plastic deformation of TC6 titanium alloy analyzed by in-situ synchrotron based X-ray diffraction and microstructure based finite element modeling, Journal of Alloys and Compounds 688 (2016) 787-795.

[135] N. Tsuchida, T. Kawahata, E. Ishimaru, A. Takahashi, H. Suzuki, T. Shobu, Static Tensile Deformation Behavior of a Lean Duplex Stainless Steel Studied by In Situ Neutron Diffraction and Synchrotron Radiation White X-rays, ISIJ International 53 (2013) 1260-1267.

[136] B. Fu, W. Y. Yang, Y. D. Wang, L. F. Li, Z. Q. Sun, Y. Ren, Micromechanical behavior of TRIP-assisted multiphase steels studied with in situ high-energy X-ray diffraction, Acta Materialia 76 (2014) 342-354.

[137] M. Teimouri, A. Godfrey, B. Yu, N. Tsuji, Deformation behavior study in a model dual phase system of copper–martensitic steel using in-situ synchrotron X-ray diffraction, IOP Conference Series: Materials Science and Engineering 895 (2020) 012002.

[138] T. Yamashita, N. Koga, T. Kawasaki, S. Morooka, S. Tomono, O. Umezawa, S. Harjo, Work hardening behavior of dual phase copper–iron alloy at low temperature, Materials Science and Engineering: A 819 (2021) 141509.

[139] S. S. Xu, J. P. Li, Y. Cui, Y. Zhang, L. X. Sun, J. Li, J. H. Luan, Z. B. Jiao, X. L. Wang, C. T. Liu, Z. W. Zhang, Mechanical properties and deformation mechanisms of a novel austenite-martensite dual phase steel, International Journal of Plasticity 128 (2020) 102677.

[140] D. Li, G. Fan, X. Huang, D. Juul Jensen, K. Miao, C. Xu, L. Geng, Y. Zhang, T. Yu, Enhanced strength in pure Ti via design of alternating coarse- and fine-grain layers, Acta Materialia 206 (2021) 116627.

[141] A. Shokry, A. Ahadi, P. Ståhle, D. Orlov, Improvement of structural efficiency in metals by the control of topological arrangements in ultrafine and coarse grains, Scientific Reports 11 (2021) 17445.

[142] H. K. Park, K. Ameyama, J. Yoo, H. Hwang, H. S. Kim, Additional hardening in harmonic structured materials by strain partitioning and back stress, Materials Research Letters 6 (2018) 261-267.

[143] G. Li, J. Jiang, H. Ma, R. Zheng, S. Gao, S. Zhao, C. Ma, K. Ameyama, B. Ding, X. Li, Superior strength–ductility synergy in three-dimensional heterogeneous-nanostructured metals, Acta Materialia 256 (2023) 119143.

[144] D. Orlov, R. Kulagin, Y. Beygelzimer, Strain partitioning and back-stress evaluation in harmonic-structure materials, Materials Letters 275 (2020) 128126.

[145] T. Shimokawa, T. Hasegawa, K. Kiyota, T. Niiyama, K. Ameyama, Heterogeneous evolution of lattice defects leading to high strength and high ductility in harmonic structure materials through atomic and dislocation simulations, Acta Materialia 226 (2022) 117679.

[146] Z. Zhang, D. Orlov, S. K. Vajpai, B. Tong, K. Ameyama, Importance of Bimodal Structure Topology in the Control of Mechanical Properties of a Stainless Steel, Advanced Engineering Materials 17 (2015) 791-795.

[147] S. K. Vajpai, C. Sawangrat, O. Yamaguchi, O. P. Ciuca, K. Ameyama, Effect of bimodal harmonic structure design on the deformation behaviour and mechanical properties of Co-Cr-Mo alloy, Materials Science and Engineering: C 58 (2016) 1008-1015.

[148] H. Qiu, T. Inoue, R. Ueji, Experimental measurement of the variables of Lüders deformation in hot-rolled steel via digital image correlation, Materials Science and Engineering: A 790 (2020) 139756.

[149] T. Tretyakova, V. E. Wildemann, Study of spatial-time inhomogeneity of serrated plastic flow Al-Mg alloy: Using DIC-technique, Frattura ed Integrita Strutturale 8 (2014) 83-97.

[150] T. Ungar, H. Mughrabi, D. Rönnpagel, M. Wilkens, X-ray line-broadening study of the dislocation cell structure in deformed [001]-orientated copper single crystals, Acta Metallurgica 32 (1984) 333-342.

Printed by Media-Tryck, Lund 2024 NORDIC SWAN ECOLABEL 3041 0903

Division of Mechanics, Materials and Component Design
Department of Mechanical Engineering Sciences
Faculty of Engineering

ISBN 978-91-8104-255-9